

MASTER

2D Core flow instability in a wide vaneless diffuser experimental set-up design

van Boxtel, F.J.J.

Award date:
2006

[Link to publication](#)

Disclaimer

This document contains a student thesis (bachelor's or master's), as authored by a student at Eindhoven University of Technology. Student theses are made available in the TU/e repository upon obtaining the required degree. The grade received is not published on the document as presented in the repository. The required complexity or quality of research of student theses may vary by program, and the required minimum study period may vary in duration.

General rights

Copyright and moral rights for the publications made accessible in the public portal are retained by the authors and/or other copyright owners and it is a condition of accessing publications that users recognise and abide by the legal requirements associated with these rights.

- Users may download and print one copy of any publication from the public portal for the purpose of private study or research.
- You may not further distribute the material or use it for any profit-making activity or commercial gain

2D CORE FLOW INSTABILITY
IN A WIDE VANELESS DIFFUSER:
EXPERIMENTAL SET-UP DESIGN

F.J.J. van Bortel
Report number WET 2006.03

Supervisors:

Prof. dr. ir. A.A. van Steenhoven
Dr. ir. H.C. de Lange
Ir. S. Ljevar

Eindhoven University of Technology
Department of Mechanical Engineering
Division Thermo Fluids Engineering
Section Energy Technology

Summary

Unsteady flows limit the operating range of compressors and suppression of these instabilities is required to increase efficiency. A thorough understanding of the relevant fluid dynamics is needed for successful implementation of suppression techniques. The research presented in this thesis deals with an instability known as rotating stall and limits itself to the rotating stall instability in wide vaneless diffusers. One approach in the ongoing research includes the assumption that in a wide vaneless diffuser the wall effects can be neglected, yielding a two-dimensional core flow which is prone to instabilities. In numerical simulations, a two-dimensional rotating instability pattern has been obtained when reducing the mass flow in a diffuser model. This bears very strong resemblance to rotating stall and the need for experimental verification was identified.

An experimental set-up in which measurements can be performed to corroborate numerical findings was to be designed, built and tested. An air compressor was scaled to a water model with a bladed rotating cylinder inducing the fluid motion.

In the first realization of the set-up the domain height was preferred to be as large as possible. This led to unwanted three-dimensional motion in the form of a temporary Taylor-Couette-like disturbance in the vertical plane, which could not be eliminated without a slight redesign of the set-up. The reduction of the domain height was perceived as an option to suppress motion in the third direction.

An extensive domain height reduction analysis has been carried out and it proved impossible to totally eliminate the motion in the third direction. However, when using heights of 30 mm and lower it can be suppressed to a certain critical time, increasing with decreasing height. New measurements in a horizontal plane revealed a large vorticity patch rotating at a fraction of the cylinder rotation speed within the time frame where two-dimensional flow is expected. The propagation speed ratio, the vortex size and the estimated number of vortices are almost identical to the values obtained by the numerical model. Another observation that was made was the development of a distinct opposite-signed vorticity patch in close proximity to the original vortex. This too was present in the numerical simulations. A brief comparison with experiments in the diffuser of a radial flow pump revealed that there too, opposite-signed vorticity patches were encountered.

The experimental set-up needed for corroboration measurements has been developed, along with a measurement procedure. Measurements with one configuration have been performed and agree well with numerical results when looking at cell propagation speed, size, number and the presence of opposite-signed vorticity patches.

Nomenclature

Symbols

B	diffuser width	[m]
c	constant	[-]
c_p	heat capacity at constant pressure	[J/kg K]
c_v	heat capacity at constant volume	[J/kg K]
C	velocity	[m/s]
d	distance	[m]
d	gap width	[m]
D	diameter	[m]
D	vorticity dissipation length scale	[m]
g	gravitational acceleration	[m/s ²]
h	enthalpy	[J]
h	Runge-Kutta step size	[-]
k	Runge-Kutta parameter	[-]
L	length	[m]
\mathcal{L}	length scale	[m]
m	mass	[kg]
\dot{m}	mass flow	[kg/s]
Ma	Mach number	[-]
n	rotational speed	[s ⁻¹]
p	pressure	[N/m ²]
Q_m	mass flow rate	[kg/s]
Q_V	volume flow rate	[m ³ /s]
r	distance	[m]
r	radius	[m]
R	universal gas constant	[J/kg K]
t	time	[s]
T	temperature	[K]
\mathcal{T}	time scale	[s]
Ta	Taylor number	[-]
s	entropy	[J/K]
U	velocity of a mechanical component	[m/s]
\mathcal{U}	velocity scale	[m/s]
v	velocity	[m/s]
V	volume	[m ³]
W	work	[J]
x	coordinate	[-]
y	coordinate	[-]
Z	gravitational potential	[m ² /s ²]

Greek symbols

α	angle	[°]
γ	vortex strength	[s ⁻¹]
δ	boundary layer thickness	[m]
η	efficiency	[-]
κ	specific heat coefficient	[J]
μ	dynamic viscosity	[kg/m s]
ν	kinematic viscosity	[m ² /s]
ρ	density	[kg/m ³]
σ	slip factor	[-]
Υ	size ratio	[-]
ϕ	velocity potential	[-]
Φ	mass flow coefficient	[-]
ψ	stream function	[-]
ψ	power input factor	[-]
Ψ	pressure rise coefficient	[-]
ω	rotational speed	[rad/s]

Vectors

B	vector potential
g	gravitational vector
s	displacement vector
x	position vector
ω	vorticity vector

Subscripts

0	vorticity centroid
1	impeller inlet
2	diffuser inlet
3	diffuser outlet
∞	free stream
<i>a</i>	air
<i>a, b</i>	situation a, b
<i>c</i>	compressor
<i>cr</i>	critical
<i>cyl</i>	cylinder
<i>d</i>	displacement
<i>dif</i>	diffuser
<i>i</i>	based on inlet conditions
<i>i</i>	inner
<i>i, j</i>	summation indices
<i>ia</i>	interrogation area
<i>im</i>	image
<i>imp</i>	impeller
<i>min</i>	minimal
<i>mm</i>	millimeter unit
<i>o</i>	outer
<i>pix</i>	pixel unit
<i>r</i>	radial
<i>t</i>	impeller tip
<i>t</i>	tangential
<i>v</i>	vertical
<i>vort</i>	vortex
<i>w</i>	water

Contents

Summary	i
Nomenclature	ii
1 Introduction	1
1.1 Research scope	1
1.1.1 The centrifugal compressor	2
1.1.2 Compressor map	3
1.1.3 Phenomena limiting operating range	4
1.1.4 Stabilizing techniques	6
1.2 Problem definition and project objective	7
1.3 Approach and report lay-out	8
2 Analysis Tools	9
2.1 The measurement technique and data processing sequence	9
2.1.1 Particle image velocimetry	9
2.1.2 Data processing sequence	10
2.2 Vortex tools	11
2.2.1 Point vortex method	11
2.2.2 Higher order panel method	12
3 Experimental Set-up Design and Initial Measurements	13
3.1 Scaling to the water model	13
3.1.1 The scaling effort	13
3.1.2 The Taylor-Couette instability	14
3.2 The design process	14
3.2.1 Assembled set-up	14
3.2.2 Boundary conditions	15
3.2.3 The rotating body	16
3.2.4 The surface plate	18
3.2.5 The top plate	19
3.3 Measurements and results	19
3.3.1 Thin sheet horizontal plane measurements	20
3.3.2 Thick sheet horizontal plane measurements	27
3.3.3 Vertical plane measurements	29
3.4 Conclusions	31

4	Experimental Set-up Redesign and New Measurements	32
4.1	The design alterations	32
4.2	Measurements and results	34
4.2.1	Vertical plane measurements	34
4.2.2	The sticking particle problem	39
4.2.3	Horizontal measurements	42
5	Comparison with Numerical Results and Experiments	46
5.1	Comparisons with numerical results	46
5.1.1	Vortex size	46
5.1.2	Approximation of the number of vortices	47
5.1.3	Propagation speed ratio	47
5.1.4	Opposite vorticity presence	47
5.2	Comparisons with other experiments	48
5.2.1	Propagation speed ratio	48
5.2.2	Opposite vorticity presence	49
6	Conclusions and Recommendations	50
6.1	Conclusions	50
6.2	Recommendations	51
	Bibliography	52
A	Image Recording Equipment	56
A.1	The laser and its appurtenances	56
A.2	The camera and computer system	57
B	Detailed Data Conversion	59
C	The point vortex analogy	60
C.1	Proving the analogy	60
C.2	Invariant quantities	62
C.3	Runge-Kutta method	63
C.4	Two-vortex system	63
D	Centrifugal compressor scaling	65
D.1	Medium scaling	65
D.2	Geometric scaling	67
D.3	Dimensions of air compressor and working conditions at stall point	68
E	Minor design issues and rejected ideas	70
F	Individual components	73
G	Measurement protocol	75
	Samenvatting	77
	Acknowledgements	78

Chapter 1

Introduction

1.1 Research scope

A compressor is a mechanical device that increases the pressure of a gas. They are used in, for example, aircraft engines, turbocharged combustion engines and industrial gas turbines. Compressors are generally categorized based on the operation principle [Nis82]:

- **Compression by decreasing the volume**

This principle is best described as the trapping of gas in a chamber and subsequently reducing this chamber's volume. According to the law of isentropic compression, this leads to a pressure rise:

$$\frac{p_b}{p_a} = \left(\frac{V_a}{V_b} \right)^\kappa. \quad (1.1)$$

Herein, p and V represent the fluid pressure and volume, respectively. The specific heat coefficient is defined as $\kappa = \frac{c_p}{c_v}$ and is equal to 1.4 for air. The parameters c_p and c_v are the specific heats at constant pressure and at constant volume, respectively. Reciprocating and rotary compressors use this principle.

- **Compression by accelerating the fluid**

The second principle involves a conversion of induced kinetic energy into potential energy. The fluid is mechanically accelerated and then decelerated in a diverging channel. There are two important compressor types that use this operating principle, viz. centrifugal compressors and axial compressors. The process is described by the steady version of Bernoulli's theorem for compressible media, see *Kundu et al.* [Kun04]:

$$h + \frac{1}{2}v^2 + Z = c, \quad (1.2)$$

in which h is the enthalpy, v is the velocity magnitude and Z is defined as $\mathbf{g} = -\nabla Z$ with g being the gravitational acceleration defined as $g = |\mathbf{g}|$. Equation 1.2 states that the left hand part of the equation is a conserved quantity along a streamline. Recalling that the entropy s is constant, it states that the relation between velocity and pressure is essentially the same as in incompressible theory.

Since the project is aimed at instabilities occurring in the diffuser of a centrifugal compressor, the following will deal with only that particular compressor type. The reader interested in

a discussion of the other types is referred to textbooks by, for example, *Nisenfeld* [Nis82], *Cumpsty* [Cum89] and *Saravanamuttoo et al.* [Sar01].

1.1.1 The centrifugal compressor

The centrifugal compressor consists primarily of a casing, in which a rotating impeller is mounted and a diffuser, see figure 1.1, adopted from *Bradshaw & Laskin* [Bra48]. Herein, the airflow is coming from the right and is ejected radially outwards in the left part of the figure.

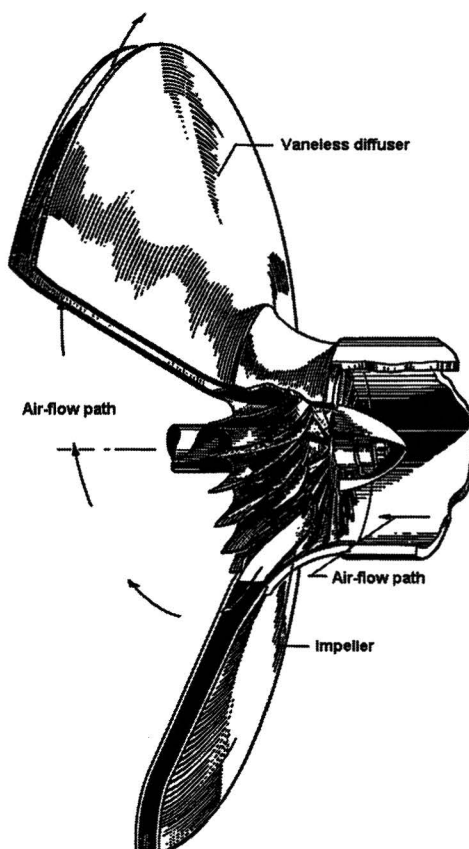


Figure 1.1: Centrifugal compressor with a vaneless diffuser, cross-sectional view.

The impeller transfers momentum to the fluid. The air is sucked into the impeller eye (or inducer) and ejected in a direction perpendicular to the rotational axis by the impeller blades. This change in direction has given rise to the alternative name radial compressor. The advantages of this compressor type over its axial counterpart include a shorter length, a greater resistance to foreign object damage, less susceptibility to performance loss due to deposit build-up on the blades and the possibility to operate over a wider range of mass flows for a given rotational speed.

The diffuser is a diverging channel in which the air is decelerated, resulting in a static pressure rise, as described in section 1.1. This diffuser can be either vaned or vaneless and its width can be constant or radially decreasing. In a vaned diffuser the gas is forced outward in a shorter path than it would be in a vaneless diffuser. If the path is too short the deceleration is too rapid which results in loss of efficiency. Vaned diffusers are more efficient at design

flows, but this is accompanied by unstable operation when the flow deviates from the design conditions. This project is concerned with instabilities in the parallel-walled vaneless diffuser of a centrifugal compressor. For more information on vaned diffusers and diffusers with a radially decreasing width, the reader is again referred to the textbooks mentioned above, viz. *Nisenfeld* [Nis82], *Cumpsty* [Cum89] and *Saravanamuttoo et al.* [Sar01].

1.1.2 Compressor map

The performance of a compressor can be specified by plotting delivery pressure and temperature versus mass flow for fixed values of rotational speed. The characteristics are dependent on other variables, which can, according to the Buckingham PI-theorem, be grouped into 4 dimensionless quantities. Hence, four scaled quantities are used to uniquely identify operating points, of which the first three are needed to determine the point in the compressor map [Cum89]:

- **Pressure rise**

This dimensionless total-to-static pressure rise is a measure of the amount of work put into the compressor compared to the work available and is given by

$$\Psi = \frac{\Delta p}{\rho U_t^2}, \quad (1.3)$$

with U_t the impeller tip speed.

- **Mass flow**

This mass flow is, for centrifugal compressors, calculated as

$$\Phi = \frac{\dot{m}}{\rho_i U_t D^2}, \quad (1.4)$$

with \dot{m} the mass flow rate and the subscript i for the density ρ indicating that it is based on inlet conditions. The impeller diameter is denoted by D .

- **Compressor speed**

This is the blade tip speed expressed in the Mach number:

$$Ma = \frac{U_t}{\sqrt{\kappa R T_i}}, \quad (1.5)$$

in which κ represents the specific heat coefficient as defined earlier. In the equation R is the gas constant (286.9 [J/kgK]) and T_0 is the fluid temperature at the inlet. The compressor speed is the quantity that is linked to the individual speed lines in the compressor map.

- **Temperature rise**

This, or another related variable, is needed to uniquely define an operating point. The isentropic efficiency is a common choice.

Compressor maps are widely used to graphically represent a compressor's operating range by plotting the pressure rise versus the mass flow, see figure 1.2. Steady state operating points with constant rotational speed are indicated by lines called speed lines. The rotational speed increases in the direction of the arrow. The load line represents the downstream system's pressure requirements. The point where these two lines intersect is the operating point.

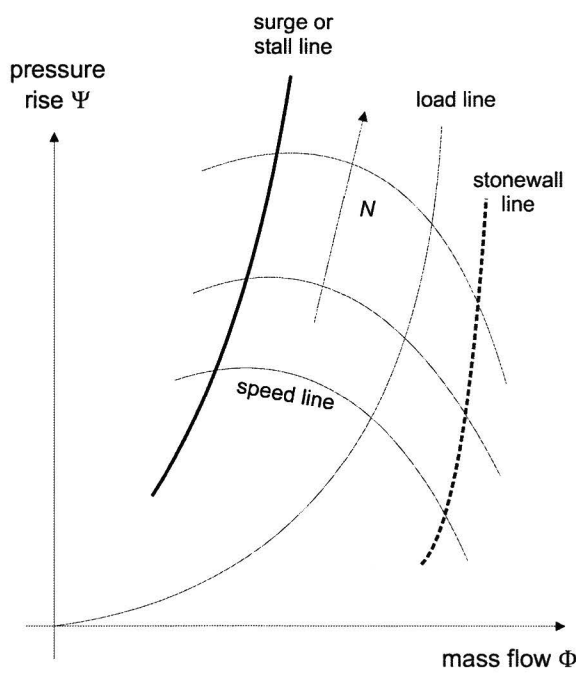


Figure 1.2: Compressor map.

1.1.3 Phenomena limiting operating range

The concept of compressor stability, or moreover stability in general, is related to the ability of a system to recover from a disturbance applied in a stable operating point. When this disturbance is transient, the performance is considered stable if the system returns to the original stable point of operational equilibrium. If not, the performance is labeled unstable, except when the perturbation was deliberate to achieve a new operating point. If steady state operation can be achieved at this new mass flow, the performance is stable once more. Compression systems are prone to various instabilities, such as combustion induced instabilities, aero-elastic instabilities and aerodynamic instabilities. *Pampreen* [Pam93] defines the latter as the ability of the entire system (guide vanes, rotors or impellers and stators or diffusers) to maintain or increase the delivery pressure to a downstream reservoir when the compressor operation has been perturbed to a lower flow. The stable operating range of compressors is limited, as shown in figure 1.2. The stonewall line depicts the limitation at high mass flows (choke), whereas at low mass flows the operating range is limited by the surge or stall line.

Choke

The maximum compressor volume flow is normally limited by the cross-section at the compressor inlet. In the subsonic regime, a decrease in frontal area induces an acceleration of the flow, whereas in the supersonic regime it would induce a deceleration of the flow [Cur03]. When the flow at the inlet reaches sonic velocity, no further increase in flow rate is possible. The choking point on a speed line in a compressor map can be identified by the onset of a steeply descending section.

Surge

The one-dimensional phenomenon called surge is a violent compression system instability that is associated with performance loss and often structural failure. Operation during surge should be avoided at all costs. The onset of surge is associated with a sudden drop in delivered pressure as the mass flow is decreased and with violent aerodynamic pulsations transmitted through the entire system. The fluctuations in mass flow can be of that magnitude that the flow can alternate between positive and negative. The annulus-averaged mass flow is unsteady, but circumferentially uniform. During surge and the suppression thereof, one often encounters another instability, called stall. For a more in-depth discussion of surge in centrifugal compressors, the reader is referred to *Willems* [Wil00] and *Meuleman* [Meu02].

Stall

The term stall refers to a cease in static pressure rise increase in a cascade or a diffuser. Experiments on stall in centrifugal compression systems are much less manifold than in their axial counterparts. However, for centrifugal compressors more is known on interaction between the acceleration and the deceleration areas.

Stall local to the inducer is experimentally observed to be non-rotating, while stall in other parts of the compression system is observed to be rotating. *Pampreen* [Pam93] states that impeller stall is initiated by one-dimensional boundary layer separation at the blade suction side, whereas diffuser stall is initiated near or in the diffuser or carried over from the impeller. Vaned diffuser stall is said to be initiated in the semi-vaneless space at the diffuser inlet and vaneless diffuser stall by separation inside the diffuser, as first proposed by *Jansen* [Jan64]. Other authors have made the assumption that the rotating stall instability is a two-dimensional feature, for example the 2D core flow instability approach adopted by *Abdelhamid* [Abd80] and *Tsujimoto et al.* [Tsu96]. This assumption inextricably rejects the effects of wall boundary layers, which were used to investigate rotating stall by several other authors, such as *Jansen* [Jan64], *Senoo & Kinoshita* [Sen77], *Frigne & van den Braembussche* [Fri84] and *Dou & Mizuki* [Dou98].

In rotating stall, the annulus-averaged mass flow is steady, but circumferentially non-uniform. It consists of stalled zones covering one or more blade passages or part of the diffuser. These zones rotate at a fraction of the rotor speed in the direction of rotor or impeller rotation in the absolute frame of reference. However, when assessing the movement of the cells in a co-rotating frame, the stall cells rotate in the other direction, but at a speed lower than the rotational speed of the rotor or impeller. This propagation can be seen as the stalling of the previously unstalled rearward blade, due to an increased incidence angle. This angle is increased due to the deflection of the flow by the already stalled region, see figure 1.3. The stalled forward blade recovers from its stalled state. Note that this figure represents an axial compressor rotor, since the illustration of cell propagation is more convenient. The essence however, is quite similar for centrifugal compressors. The only significant difference is that in axial compressors, there is a net through-flow in the axial direction, whereas in centrifugal compressors this net flow is in the radial direction.

The relative cell motion is greater for large stall cells (see *Greitzer* [Gre81]) and hence, in the absolute frame or reference, this results in a lower rotating speed for larger cells. This rotational speed is subject to discussion. It is reported to be between 20 and 80 % of the rotor speed for axial compressors, according to *Greitzer* [Gre81] or between 10 and 90 % for

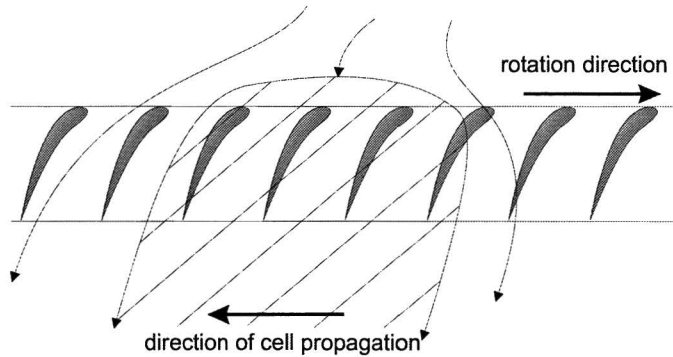


Figure 1.3: Stall cell propagation in an axial compressor.

both compressor types, according to *Kämmer & Rautenberg* [Käm86]. Why not all blades stall simultaneously is not known, but there are speculations that dimensional tolerances play a role. *Pampreen* [Pam93] states that the number of stall cells can vary between 1 and 9 for axial compressor rotors, whereas no such statements are presented for centrifugal compressors.

1.1.4 Stabilizing techniques

The most favorable operating points of a compression system are usually near the surge or stall line. The limitations in stable operation region due to surge and stall can be overcome mechanically and via control. Without aiming at an extensive description of all methods available, *Willems* [Wil00] proposes the following categorization:

- **Techniques focussing on better interior design**

These techniques include the use of a low-solidity vaned diffuser, as reported by *Buse et al.* [Bus96] and a decreased tip clearance as proposed by *Day* [Day93] and *McDougall et al.* [McD90]. *Greitzer* [Gre81] reports casing treatment and backward leaning rotor blades to be effective, whereas *Freeman et al.* use an increased number of blades [Fre98].

- **Techniques using variable geometry**

Movable inlet guide vanes change the shape of the compressor characteristic, see *Camp & Day* [Cam98] and *Rodgers* [Rod91]. When using a vaned diffuser, the option of movable diffuser vanes arises, as reported in *Hunziker & Gyarmathy* [Hun94] and *Lawless & Fleeter* [Law95].

- **Suppression by control**

The easiest control methods incorporate the surge detection and avoidance principle, often using a bleed valve, see, for example *Botros & Henderson* [Bot94]. More efficient active control, as first proposed by *Epstein et al.* [Eps89] uses controllers to feed back perturbations to the flow field to effectively stabilize unstable operating points. It has led to linear and nonlinear control methods, see also *Abed et al.* [Abe93] and *Haddad et al.* [Had99]. *McCaughan* [McC90] was the first to realize the use of bifurcation stabilization and for the current state of the art articles in this area, the interested reader is referred to, for example, *Liaw & Abed* [Lia96], *Chen et al.* [Che98], *Kang et al.* [Kan99], *Wang & Murray* [Wan02a], *Wang et al.* [Wan02b], *Nayfeh & Abed* [Nay02] and

Coller [Col03]. *Krstic et al.* [Krs95] use a backstepping method, while *Banaszuk and Krener* [Ban99], *Belta et al.* [Bel01] and *Willems* [Wil00] build upon the Moore-Greitzer model and the Greitzer lumped model.

Due to the scope of the report, the methods above will not be elaborated here. This section's goal was to give a brief overview of stabilizing methods to illustrate that there's much experience in control regarding this area of fluid dynamics. Clearly, most of the stabilizing techniques, be it via active control or not, are aimed at mitigating or eliminating the effects due to the one-dimensional instability surge.

Usually, rotating stall occurs when surge is postponed using active surge control techniques. Rotating stall is a phenomenon that limits the operating range of compressors as well and which is also known to generate noise and vibrations. These vibrations can cause structural failure in the compressor itself or in a pipeline further away due to resonance. In order to be able to implement similar control strategies as for surge, research is needed to gain more insight into the fluid dynamics of rotating stall.

1.2 Problem definition and project objective

The research on the fluid dynamics behind rotating stall in vaneless diffusers of centrifugal compressors is being performed by *Ljevar et al.*, see [Lje05a] and [Lje05b]. Using CFD methods, a two-dimensional incompressible viscous flow model has been constructed to study the vaneless diffuser core flow instability. The vaneless diffuser is considered wide, meaning it has a width to inlet radius ratio larger than 0.1: $\frac{B}{r_2} > 0.1$. For wide diffusers the assumption can be made that the core flow and the instability therein are two-dimensional and the influence of the wall boundary layers can be neglected. Also, the diffuser walls are assumed to be parallel. The impeller outflow is modeled by prescribing a rotating jet-wake pattern at the diffuser inlet. The diffuser outflow is radially unhindered save for a constant static pressure prescribed at the diffuser outlet. Figure 1.4(a) shows a stable flow pattern in a vaneless diffuser and figure 1.4(b) reveals zones of stalled flow.

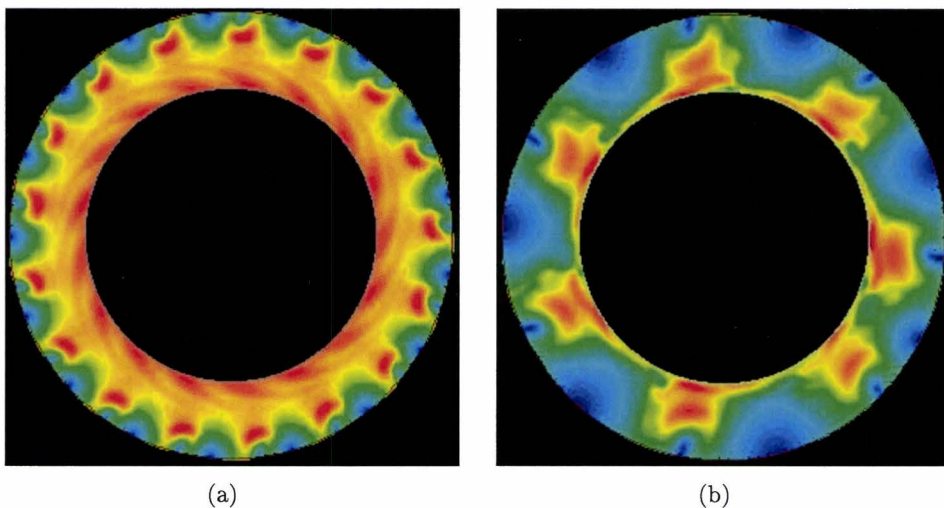


Figure 1.4: Numerically obtained stable (a) and unstable (b) flow in a vaneless diffuser.

In the figure the diffuser inlet and outlet are 0.03225 and 0.04908 m, respectively. Both images are from the same simulation, in which a decreasing mass flow is employed to lower the angle of the jet direction with the horizontal. The coloring is by velocity magnitude, where a blue region depicts a low velocity region and a red region a high velocity one. The rotation of the jet-wake pattern is clock-wise.

The desire now arises to obtain experimental verification of these numerical results. The project goal is thus defined as the design, realization and testing of an experimental set-up for experiments on the two-dimensional core flow instability and performing the experiments to corroborate the presented numerical results or part thereof.

1.3 Approach and report lay-out

The first step in the realization of the project objective is gathering the available tools for obtaining, analyzing and interpreting data, which are discussed in chapter 2. The air compressor is scaled to a water model before the actual set-up design can commence. This, along with a discussion of the experimental set-up design and measurement results, is discussed in chapter 3. The results from this chapter reveal the need for a set-up redesign. This is described in chapter 4, along with the performed measurements and the analysis thereof. Chapter 5 is dedicated to comparing the obtained measurement data to numerical and other experimental results. The conclusions and recommendations from the present study are presented in chapter 6.

Chapter 2

Analysis Tools

2.1 The measurement technique and data processing sequence

Information on rotating stall in a diffuser can be obtained by performing measurements in actual air compressors or scaled models thereof, with the aid of various techniques. Pressure trace analysis obtained with pressure transducers is a common technique and was employed by a variety of authors, including *Abdelhamid et al.* [Abd79], *Hunziker & Gyarmathy* [Hun94], *Kämmer & Rautenberg* [Käm82] and *Justen et al.* [Jus99]. Hot-wire anemometry is another technique, as used by *Jansen* [Jan64] and *Frigne & van den Braembussche* [Fri84]. To gain a more thorough insight in the occurring phenomena however, flow visualization is desirable. There are numerous methods that can be used to visualize a flow field. Without aiming at an extensive discussion a few methods are mentioned. Depending on the fluid, smoke, air bubble and dye visualization is possible. A very effective method for flow field generation is Particle Velocimetry (PV), which uses tracer particles, as employed by *Wuibaut et al.* [Wui02]. In the water model used in this project, this latter method has been used. The following sections provide some basic information on the method and will discuss the data processing sequence.

2.1.1 Particle image velocimetry

Flow phenomena can be investigated by using tracer particles to visualize the flow field. These particles are small enough to follow the fluid flow closely and neutrally buoyant. In water, a common choice is to use polyamid or glass seeding particles with, for example, an average diameter of 20 or 50 microns. These particles are illuminated by means of a laser sheet, created with a laser and the relevant lenses, mirrors and optomechanics. A CCD camera records frames with the moving particles which, after correlation, can be used to analyse the flow field. If a match has been established between particles in subsequent frames, these are assumed to correspond to the same physical particle. Next, the distance it has traveled can be calculated. To map this virtual distance to a physical one, calibration is required. This method is called particle velocimetry and can be subdivided into several different techniques.

Particle Image Velocimetry (PIV) is the technique that has been used in this project and for more information on other techniques, such as Particle Tracking Velocimetry and High-resolution Particle Velocimetry, the interested reader is referred to *van der Plas et al.* [Pla03]. PIV needs only two subsequent images to construct a flow field, which makes it a very effective technique for flow visualization. PIV images are divided into rectangular sectors and the corresponding sectors of two images are cross-correlated. Maximum correlation means that

the best match is found. The algorithm determines average particle displacements in corresponding frame segments. There are several demands to good PIV measurements, as adopted from *van der Plas et al.* [Pla03]:

1. Sufficient particles should be present in each image segment. In most cases it is recommended to have at least 4 to 8 particles per segment to ensure a clear correlation peak.
2. It should be avoided to have too many particles leaving the segment between the two correlating frames. The advised maximum particle displacement is one fourth of an image segment.
3. To avoid losing coherence, the velocity gradients in an image segment should not be too large.
4. Particles suddenly appearing in or disappearing from the second frame of a correlation pair have a negative influence on the correlation and should be avoided.
5. A minimal particle displacement of two pixels is recommended to ensure accuracy of the velocity vector.
6. Good quality images generally yield good correlations and avoidance of background noise and obtaining clear particle images can be imperative for the correlation process.

Since a pulsed laser has been used in this project, the experimental output is a quasi-equidistant frame sequence. A pulsed laser produces two pulses spaced only a small timestep apart and these pulse couples are spaced apart another, larger timestep, see figure 2.1. These timesteps are usually specified using a delay generator. It yields a sequence in which n frames lead to $\frac{n}{2}$ correlation pairs at most. For a listing and a brief description of the equipment used in the image recording process, the reader is referred to appendix A.

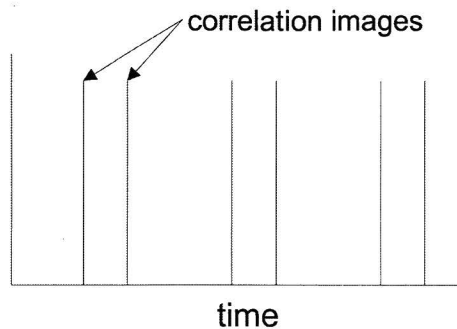


Figure 2.1: Captured images when using a pulsed laser.

2.1.2 Data processing sequence

In the previous section, the correlation process has been described. The frames are recorded by a CCD camera using the VideoSavant image capturing software. The measurement data is stored in real time display (rtd) files. Using a UNIX secure shell client, the separate images are extracted from these files and converted to 10 bit and later 8 bit portable gray map bitmap

(pgm) files. This yields the time-sampled frame sequence as discussed in the previous section. The program PIVview is used for the frame correlation. This program allows several image preprocessing activities before the correlation begins, including filtering, background subtraction and masking. Several correlation methods can be used, and unusable data can be skipped and/or replaced via outlier detection. The program stores the velocity field it extracts from the frames in NetCDF parameter (nc) files and it allows for several flow quantities to be visually represented.

However, a flexible MATLAB script invoking the MexCDF toolbox has been created to enable further editing of the data, with respect to vector and color bar scaling, neglecting information in part of the frame and subtracting mean flow quantity values. Also, the visual representation options are made more extensive and vortex identification techniques are employed. The data is stored in easily accessible text files (with a dummy extension .piv). The described data processing sequence is schematically represented in the block diagram in figure 2.2. For a more detailed description of the data conversion procedure, the reader is referred to appendix B.

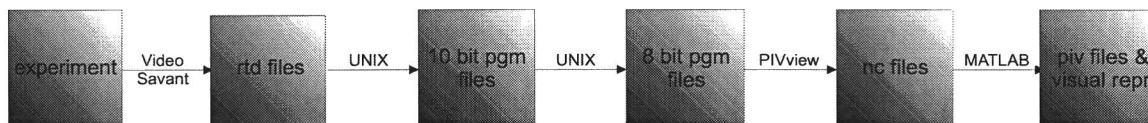


Figure 2.2: PIV data processing sequence.

2.2 Vortex tools

2.2.1 Point vortex method

Vortex interaction is a widely studied topic where numerous approaches have emerged. Point vortex analogies are manifold, as previously shown by *Aref* [Are83] and improvements on this method have been reported by *Chorin & Bernard* [Cho73] and *Krasny* [Kra87] in the form of a vortex blob method. This method solves the problem that the presence of several vortices in close proximity of one another inevitably leads to chaotic motion. Also, the cloud-in-cell technique, as described by *Christiansen* [Chr73a], has arisen in the field of vortex dynamics. It is effective in modeling the merging process of two vorticity patches [Chr73b].

In this section, the discussion is kept confined to point vortices, due to the favorable ratio between complexity and practical use. The point vortex analogy has been used to numerically study occurring vortex dynamics in the experimental set-up. The MATLAB script that has been used is, on request, available from the author.

It can be proven that, at some distance from its center, the velocity field due to a vorticity distribution $\omega(\mathbf{x})$ is essentially the same as that due to a point vortex of strength $\int \omega dA$ in the center of the vorticity patch. The reader interested in a more in-depth discussion of this matter is referred to appendix C.1, where the analogy is derived. Vortices induce velocities in fluid elements in their proximity. When incorporating more vortices, the interaction can be

summed up as follows:

$$\frac{dx_j}{dt} = -\frac{1}{2\pi} \sum_{i=1, i \neq j}^n \gamma_i (y_j - y_i) / r_{ij}^2, \quad (2.1)$$

$$\frac{dy_j}{dt} = +\frac{1}{2\pi} \sum_{i=1, i \neq j}^n \gamma_i (x_j - x_i) / r_{ij}^2 \quad \text{with} \quad (2.2)$$

$$r_{ij}^2 = (x_j - x_i)^2 + (y_j - y_i)^2. \quad (2.3)$$

In these equations x and y are the vortex coordinates while γ is the vortex strength. Vortices do not induce velocities in themselves, but they do have an effect on other vortices in their proximity. The magnitude of this effect is inversely proportional to the distance between the two interacting vortices, as can be concluded from the above equations.

2.2.2 Higher order panel method

For insight into the vortex shedding behavior, the above mentioned point vortex analogy is not suited and the interested reader is referred to, among others, articles describing the higher order panel method. This method describes two-dimensional vortex sheet motion in incompressible fluids, see *Hoeijmakers & Vaatstra* [Hoe83]. The method can be applied to describe flow separation behind sharp edges after mapping the physical domain to a one-sided computational domain using the Schwartz-Christoffel transformation, see *Peters & Hoeijmakers* [Pet95]. An interesting concept surely, but this was considered beyond the scope of the present study, albeit worth mentioning.

Chapter 3

Experimental Set-up Design and Initial Measurements

3.1 Scaling to the water model

3.1.1 The scaling effort

Prior to this project, measurements in an air compressor have been performed and numerical simulations have been carried out. The details of this compressor have been used in a scaling effort, leading to the dimensions of the current set-up. There are two geometric parameters that describe a vaneless diffuser with constant width, which can be used in scaling efforts, see *Cumpsty* [Cum89].

- **Diameter ratio**

The ratio of the outlet to the inlet diameter is the first geometric parameter, which has to be maintained constant in scaling efforts:

$$\frac{D_3}{D_2} = c, \quad (3.1)$$

in which D stands for diameter and the subscripts 2 and 3 refer to diffuser inlet (impeller outlet, approximately) and diffuser outlet, respectively.

- **Width to outer diameter ratio**

The diffuser width is in the same way related to the diffuser outlet diameter:

$$\frac{B}{D_3} = c, \quad (3.2)$$

with B referring to the diffuser width.

These scaling laws have been used and expanded for the air-to-water scaling, as described in appendix D. The outcome of the scaling laws was primarily used to determine the impeller radius. The diffuser width was assumed rather irrelevant by means of the assumption of a two-dimensional instability of the flow field [Lje05b]. An important simplification was made, since in the model as used in the current project, no actual impeller outflow is present. The scaling laws and procedure are presented in full in appendix D for possible project continuation.

There was a constraining design parameter in there being an available perspex tank, which

has an inner diameter of 640 mm and a height of 1285 mm. The constraining parameter here is the internal tank diameter. The diffuser has to be scaled to fit in the tank with room to spare, radially. This is because the tank has no outflow options and the solid wall would then influence the occurring flow phenomena to an unacceptably high degree. As mentioned before, one could justifiably argue that the set-up has no inflow either. However, the fluid motion the impeller rotation will provide is, for now, considered to be enough to study the two-dimensional instability in the diffuser.

Since now the diffuser width and fluid velocity criteria have been eliminated from the scaling effort, it boils down to a simple diffuser inlet-outlet ratio that has to be maintained:

$$\frac{D_3}{D_2} = 1.52. \quad (3.3)$$

Hence, when choosing the impeller diameter to be in the range of 200-300 mm, the required diffuser outlet diameter is ranging from 304-456 mm, which leaves more than enough space for the fictive outflow as mentioned above.

3.1.2 The Taylor-Couette instability

A well-known instability in experimental set-ups with rotating cylinders is the Taylor-Couette instability. It was considered important to address its physics in the design phase. The phenomenon is an instability of the flow field due to centrifugal force. Fluid is forced outwards and returns to the middle due to pressure gradients, see figure 3.1. As a result, a stacking of counter-rotating cells develops. It can be present in set-ups in which an inner and an outer cylinder co-rotate or in which only the inner cylinder rotates, as is the case in the present set-up. A dimensionless number that is relevant here is the Taylor number, which is defined as

$$Ta = \frac{\Omega_i^2 R d^3}{\nu^2}, \quad (3.4)$$

with Ω_i the rotational speed of the inner cylinder, R the average radius, d the distance between the two cylinders and ν the kinematic viscosity of the medium.

For the instability to occur, the Taylor number needs to exceed 1712 and $d \ll R_i$ has to hold, with R_i referring to the radius of the inner cylinder. A rough estimation involving a rotational speed of 1 m/s, an average radius of 0.2 m, a gap width of 0.2 m and a kinematic viscosity of 10^{-6} yields a Taylor number in the order of magnitude of 10^9 . Obviously, the first criterium is met, but the second and more subjective criterium is not. In fact, in the radius interval as mentioned in section 3.1.1, the radius difference is of the same order of magnitude as the inner cylinder radius, or $d \approx R_i$. This observation led to the assumption that the Taylor-Couette instability was not going to develop in the scaled set-up.

3.2 The design process

3.2.1 Assembled set-up

The assembled set-up is represented in figure 3.2(a). Here one can clearly see the cylindrical tank as it is positioned in the center of a rectangular one. Both these tanks are filled with

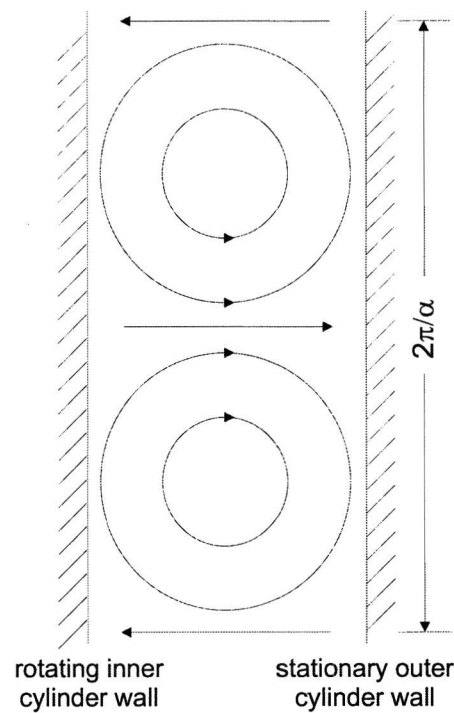


Figure 3.1: The Taylor-Couette instability.

water. Inside the cylindrical tank, a rotating body, including cylinder, connection plates, blades and axes, is visible and it is represented separately in figure 3.2(b). One can see the surface plate as it floats on the water surface to suppress wave motion and on the bottom of the tank, a cross-shaped bottom plate lies. A camera and an electromotor are represented on the top plate. This total set-up is standing on a frame, the geometry of which is rather trivial and not represented in the figure.

The following subsections will describe the separate components in the realized experimental set-up. Given the enormous amount of design issues and possible solutions, only the major design issues will be addressed here. A few abandoned ideas are presented in appendix E for future reference and appendix F contains detailed drawings of the connection plates and the blades.

3.2.2 Boundary conditions

As stated in the previous section, the exterior geometry of the set-up was predefined. The cylindrical tank has an interior diameter of 640 mm and a height of 1285 mm and is placed inside a rectangular tank with an 850 mm square ground area and a height of 1250 mm. The latter can be filled with water to mitigate image distortion due to light refraction when recording images from the side. This tank combination is placed on a frame that elevates the tank bottom to about 670 mm above the ground, to facilitate easy draining of the tanks. Nothing was to be altered or damaged in the available tank.

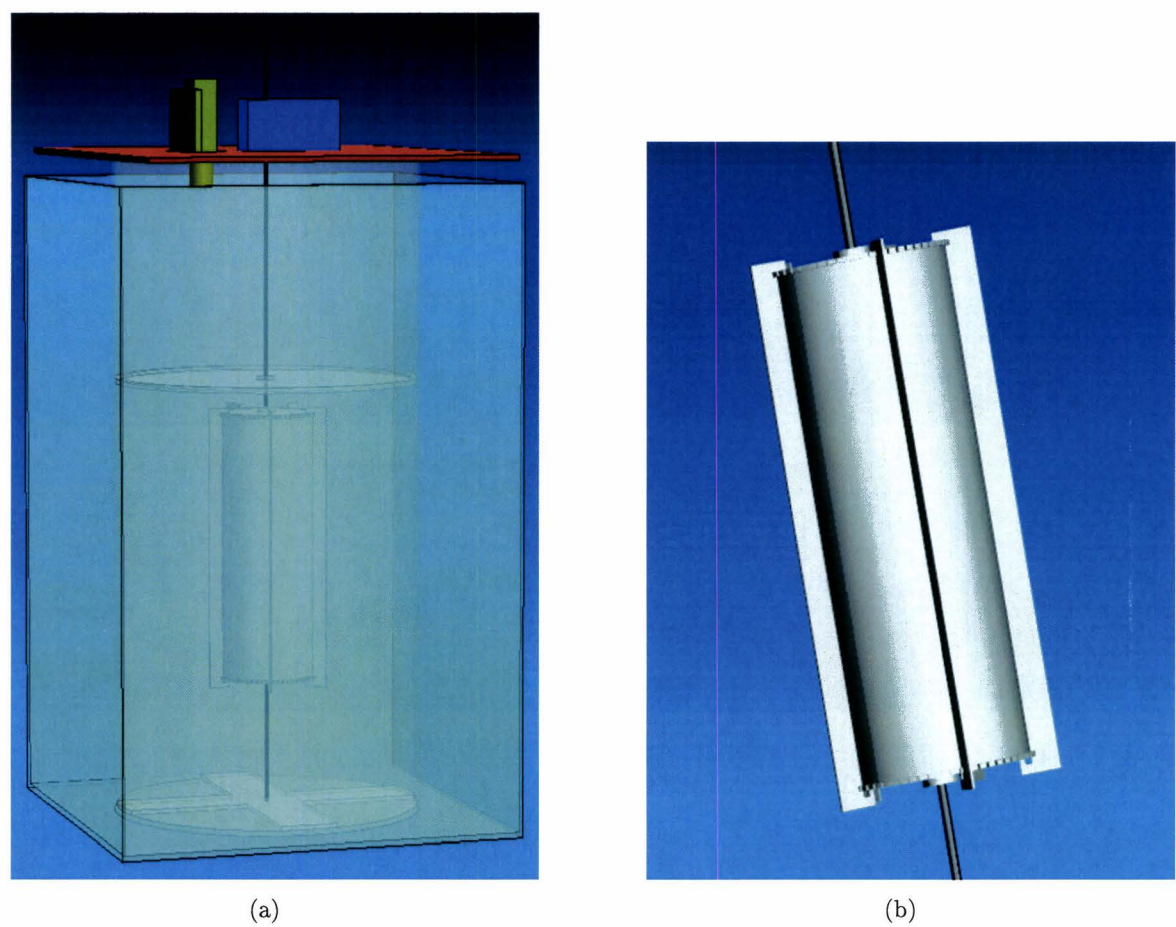


Figure 3.2: The complete set-up (a) and the rotating body (b), Unigraphics images.

3.2.3 The rotating body

Inside the cylindrical tank a rotating body had to be positioned, as represented in figure 3.2(b). To make optimal use of the tank's radial extent, the rotating body was chosen to be a PVC cylinder with an outer diameter of 200 mm (wall thickness 5 mm), which leaves enough room for blades to be mounted onto the cylinder. Due to the rotation of this part, the fluid will start to move and since a passing blade ejects a jet of fluid, this can be seen as an impeller outflow, albeit a rather weak approximation thereof.

The length of the cylinder has been a key issue in the design of the experimental set-up and is bound to contradicting demands. On one hand the cylinder is preferred to be as long as possible, to eliminate the influence of the end effects at the upper and lower ends of the blades on the flow field. On the other hand too long blades will prove impractical in realization and in preparing the set-up for measurements. Moreover, with the blades being attached to the cylinder only at the top and the bottom, another problem arises when using long blades. The main disadvantage of long blades then is the fact that the blades will experience bending, which induces unwanted three-dimensional motion. The length of the blades has been chosen to be 550 mm, which is considered a good trade-off between the demands mentioned above when using a blade thickness of 3 mm, see figure 3.3.

The blades themselves have been subjected to several alterations. The number of blades was

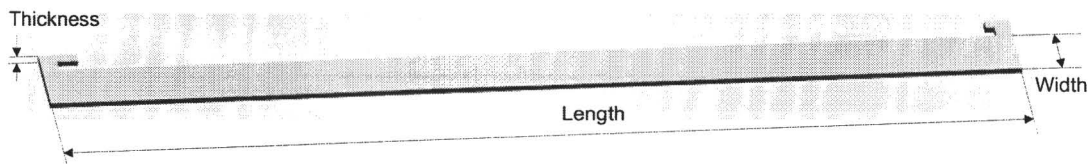


Figure 3.3: Impeller blade, Unigraphics image.

altered until the best number for the measurements was identified. The width of the blades has initially been chosen to be 10 mm, but this was changed to 30 mm upon discovering that the first blade width did not trigger tangential flow to the desired extent. The material was changed from PVC to perspex when in vertical measurements the PVC blades scattered too much of the laser light into the camera when being at a certain position. This yielded great light intensity differences in the frame sequence, which is not desirable. The blade geometry, as schematically presented in figure 3.3, shall be elaborated on shortly.

The cylinder was to be connected to a rotating axis by means of an upper and lower plate, glued onto the cylinder. With the length of the blades defined, a fixation mechanism was to be designed since ideally, the number and position of the blades should be adjustable. This tricky demand was met by designing the blades and fixation plates as depicted in figures 3.3 and 3.4, respectively. Figure 3.4(a) represents the lower connection plate and 3.4(b) represents its upper counterpart. The slots in the circumference of the plates provide tangential blade fixation. It was desired to enable numerous different blade distributions, including numerous possibilities with uniform distributions. There are 60 slots in the circumference for that is a practically feasible number with a lot of possible uniform distributions.

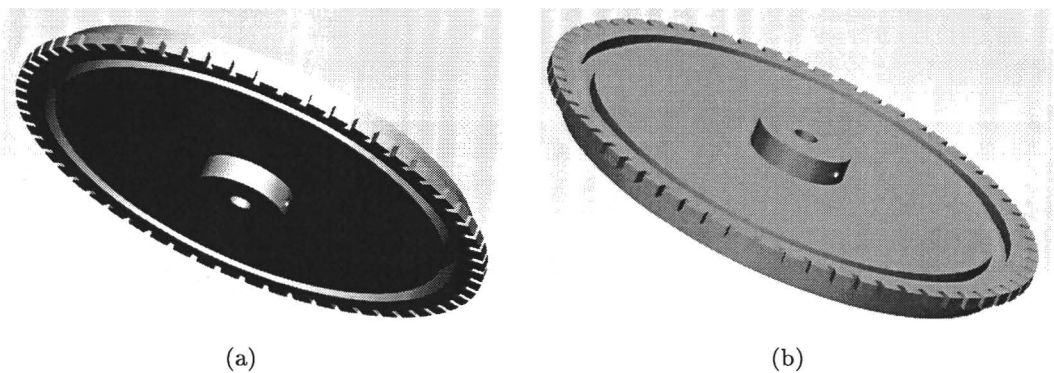


Figure 3.4: Lower (a) and upper connection plate (b), Unigraphics images.

Figure 3.5 illustrates how the blades are put into place. The mounting of the blade involves first sticking the pin at the lower end of the blade into the 12 mm deep circular groove in the lower fixation plate and subsequently pushing the pin at the upper end of the blade into the 5 mm deep groove in the upper fixation plate. The blades are now radially, tangentially and axially fixed yet their position and number can still be altered in-situ. In order to remove a blade, it has to be lifted into the position that the pin at the bottom is completely inside the groove again, which allows it to come free at the top end. Note that, for clarity, the figure is not to scale.

An upper and lower axis with a diameter of 10 mm are connected to the fixation plates by

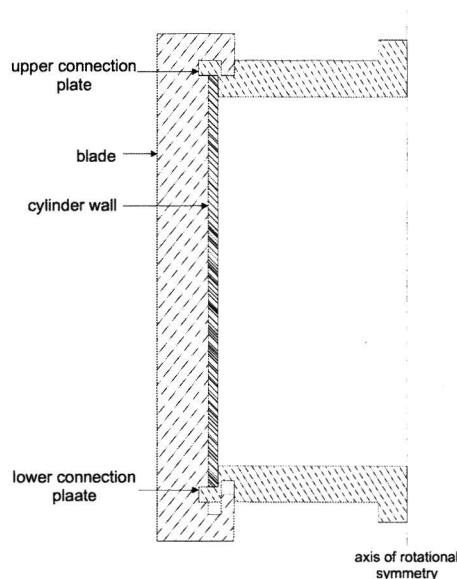


Figure 3.5: The blade fixation solution.

sticking them into the center holes and fixing them with a small bolt. The lengths of these axes were chosen to be 750 and 250 mm, respectively. This is long enough to allow for the upper axis to be clamped into an electromotor. Due to these axes being in continuous contact with water, they have been made out of stainless steel. The designed rotating body had to be radially fixed in the center of the cylindrical tank. A bottom plate was designed in the shape of a cross with a non-through hole in the center to provide this radial fixation at the bottom and to avoid damage to the bottom of the tank, see figure 3.6. The axis has two more radial fixations, one of which has already been mentioned, viz. the electromotor. The other radial fixation will become clear in the next subsection.

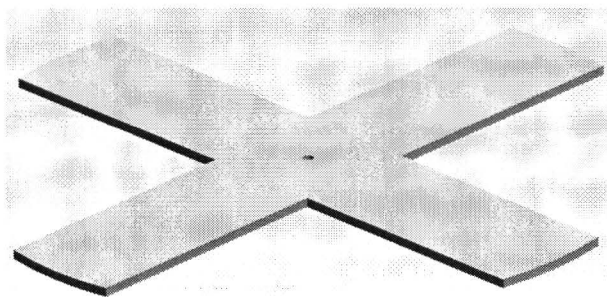


Figure 3.6: The cross-shaped bottom plate, Unigraphics image.

3.2.4 The surface plate

During the PIV measurements a laser sheet was directed into the tank and a high speed camera was recording from above or from the side. During operation, waves are bound to be generated by the rotation of the rotating body. These waves distort the images recorded from above. A perspex plate with a hole in the center is placed on top of the water surface to keep

it flat and hence, the optical distortion to a minimum. Besides the negative influences waves would have on the images, they would also imply motion in the third dimension.

Besides solving these issues, the surface plate provides the second radial axis fixation. Due to the density of perspex being slightly higher than that of water, the plate would be prone to sinking. This has been overcome by gluing an additional edge onto the plate, as illustrated in figure 3.7. This lowers the plate's effective density by 'trapping' air, causing it to float. Another advantage of these edges is that they keep all water off of the surface altogether.

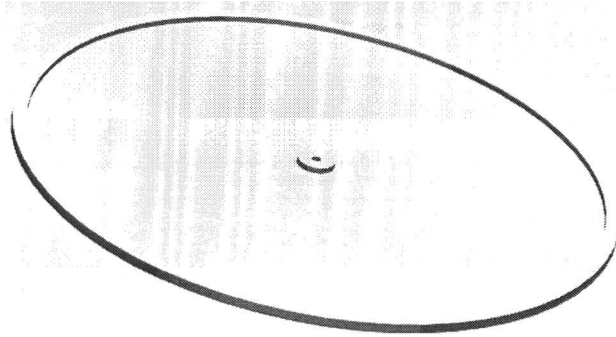


Figure 3.7: The surface plate, Unigraphics image.

3.2.5 The top plate

The rotation of the axis and hence the rotation of the cylinder with the blades mounted onto it is realized by means of an electromotor. This motor is mounted onto a plate that lies on top of the cylindrical tank, see figure 3.2(a). The rotation is clockwise (negative rotation) when viewed from above and only the lowest rotational speed can be used due to the occurrence of significant slip when operating at a higher rotational speed. The clamping of the axis in the motor is obviously the third radial fixation, as stated before. On the same plate, the camera can be mounted when recording images from above. The positions of both the motor and the camera are fixed to ensure measurement repeatability, but adjustable if needed. Three small blocks are attached to the bottom of the top plate, to make sure it can be put on top of the set-up's cylindrical tank in exactly the same position every time.

3.3 Measurements and results

Before measurements can be conducted, several things need to be addressed to ensure good image correlation. First, the concentration of particles is a very important issue, as mentioned in section 2.1.1. Too few particles yield to few correlations and too many particles may lead to images that can not be correlated at all. The best concentration can be calculated, but it is often best to use a base concentration and add particles to improve upon that with visual feedback.

Also, the time between the two correlation pulses is very important. The maximum displacement of a particle is one fourth of an interrogation area. Using the rotational speed of the cylinder as the upper velocity limit, the time between the pulses is now dependent on the rotational speed of the cylinder, the image and interrogation area size in pixels and the image

size in millimeters. For example, when using images of 1000 by 1000 pixels, corresponding to 100 by 100 mm, an interrogation area of 32×32 pixels and a maximum rotational speed of 1 revolution per second, the following simple calculations can be made. First the interrogation area size determines the maximum particle displacement in pixels, which can be converted to a displacement in millimeters. The ratio between interrogation area and image sizes is given by

$$\Upsilon = \frac{L_{ia,pix}}{L_{im,pix}} = \frac{L_{ia,mm}}{L_{im,mm}}, \quad (3.5)$$

with L_{ia} and L_{im} being the sizes of the interrogation area and the image frame, respectively. The subscripts *pix* and *mm* refer to the units used, being pixels and millimeters. Cross-multiplication in equation 3.5 yields 3.2 mm for the size of the interrogation area. Hence, the maximum particle displacement is 0.8 mm.

Assuming the maximum rotational velocity to be 1 revolution per second gives a tangential velocity upper limit of 0.82 m/s. The time between the two correlation pulses can now be calculated as

$$t = \frac{\Delta x}{v} = \frac{0.8 \cdot 10^{-3}}{0.82} = 0.00098. \quad (3.6)$$

Note that this is merely an example, and that fine-tuning of this time step can greatly enhance correlation results.

3.3.1 Thin sheet horizontal plane measurements

The first measurements to be conducted with the thus described set-up were measurements in which the laser sheet was horizontal and the camera was recording from above. The thickness of the laser sheet used was reduced to 2 mm, using a sheet cut-off. One does not use the full intensity of the laser beam when using a sheet cut-off, but in this case, the remaining intensity was sufficient. Figure 3.8 is a schematic representation of such a sheet cut-off. Here, one sees the operating principle of the sheet cut-off by merely letting a selection of the laser light pass. It is an effective means of controlling the laser sheet thickness and the sheet intensity.

Rotating stall can be present in the normal operating region of a compressor and the numerically obtained cells persist for a large number of impeller revolutions. This had initially led to the assumption that the best measurement results were to be obtained after some time had passed and a developed flow pattern was obtained. Hence, the image recording was started after about two minutes and many impeller revolutions. Experiments were carried out with just a rotating cylinder and configurations with just one blade as well as a uniform blade distribution of 5 or 10 blades. In all configurations including blades, the two different blade widths were used. Every measurement in this extensive measurement set yielded sequences of flow patterns deprived of clear indications towards a two-dimensional instability. This was initially attributed to the presence of structures from previous measurements and other prior flow disturbances, so the first improvement on the measurement procedure was to make sure these were eliminated.

To eliminate left-over motion from previous measurements or set-up preparation, the fluid was allowed to come to rest prior to starting the cylinder rotation and the subsequent waiting for a developed flow. The image recording was thus still started in a developed flow, but one that had been allowed to develop from rest. The measurements that were carried out using this

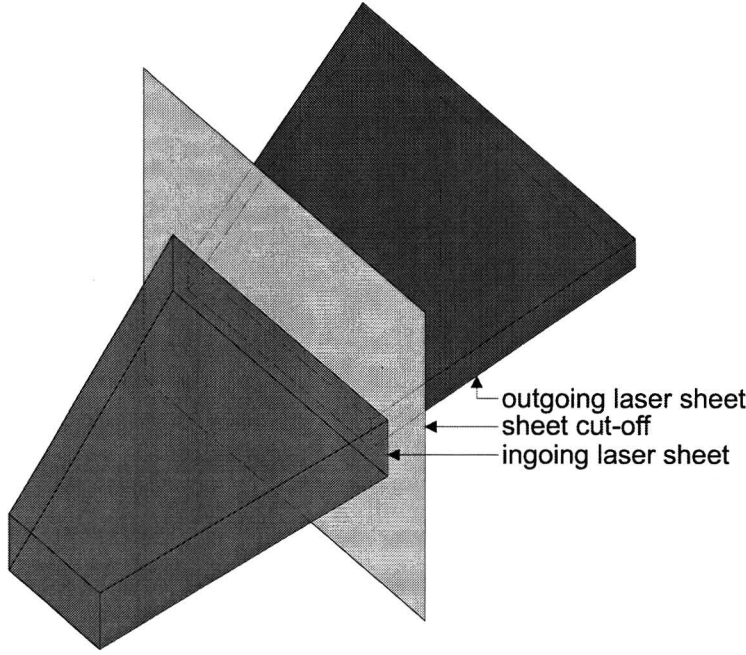


Figure 3.8: The laser sheet cut-off.

measurement procedure showed improvement, but were still without clear indications towards the instability.

The absence of these indications was then attributed to viscous annihilation of the emerged structures due to the presence of the solid wall. Drag due to this wall inhibits fluid motion to a certain degree. The dissipation timescale is derived from the following equations. It scales with the cell length and velocity scale, leading to the quite trivial equation below.

$$\tau \approx \frac{\mathcal{L}}{u} \quad (3.7)$$

Recalling that a velocity scale can be rewritten with the introduction of the kinematic viscosity ν as

$$u \approx \frac{\nu}{\mathcal{L}}, \quad (3.8)$$

equation 3.7 can be rewritten to

$$\tau \approx \frac{\mathcal{L}^2}{\nu}. \quad (3.9)$$

Substituting the actual values for the parameters (with an estimated cell size in the order of 10^{-2} m) into equation 3.9 yields a dissipation timescale of around 100 seconds. In the measurements carried out so far, the image capturing process started after about two minutes. This indicates that the possible instability cells would already be, at least partially, viscously annihilated by the time the images were recorded. This explains why indications towards the two-dimensional instability have been absent and the flow field was just filled with remainders

of vortical structures. New experiments were carried out in which the start-up procedure was included in the measurement time. This had the advantage of, besides of being obviously necessary, providing insight into the development of the vorticity patches.

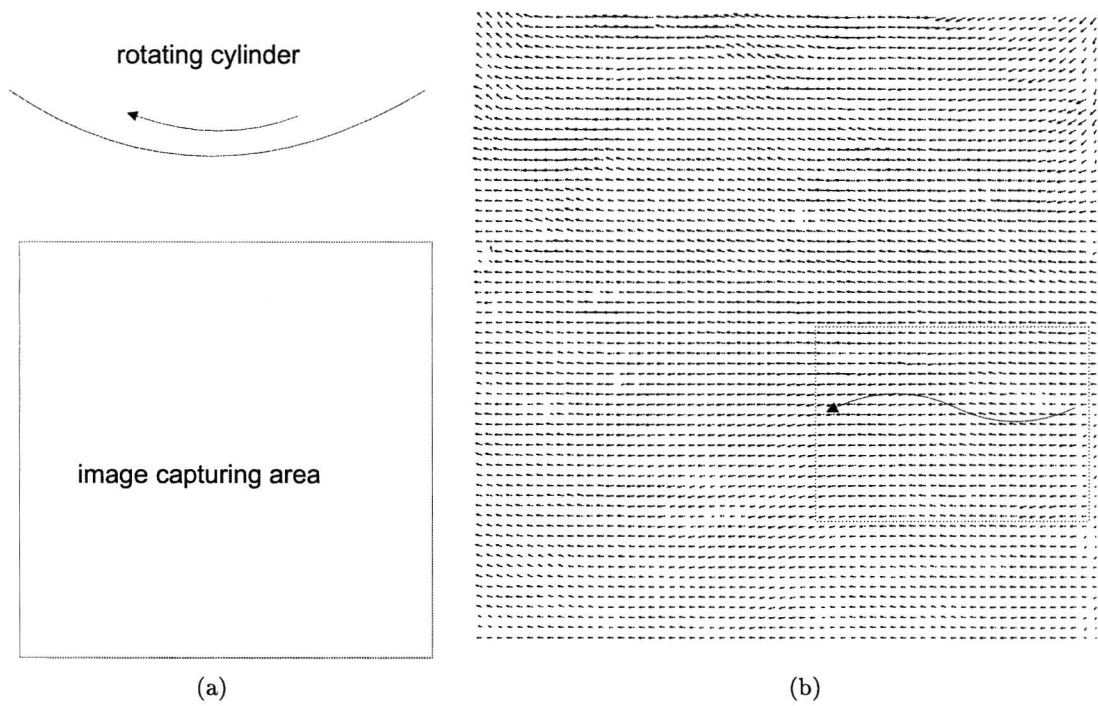


Figure 3.9: Image position elaboration (a) and flow pattern obtained without usage of blades (b).

Again, the extensive measurement set was carried out, with much more promising results. When using no blades, the fluid was accelerated too slowly to induce boundary layer separation and there were no edges to facilitate easier vortex shedding either. Figure 3.9(b) represents a flow pattern obtained in a measurement in which no blades were attached to the rotating cylinder. In this figure the vectors represent the velocity field. The measurement area is elaborated in figure 3.9(a). Although no clear instability cells can be identified in the figure, attention is drawn to the wave-like motion, as presented in magnification in figure 3.10.

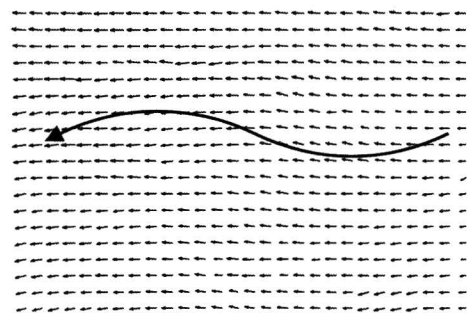


Figure 3.10: The wave-like motion in the flow field.

The wave-like disturbance in an otherwise axisymmetrical Couette flow bears very strong resemblance to the onset of the Kelvin-Helmholtz instability. This is an instability that is quite common in flows where a distinct separation plane between two bulks of fluid with different velocities is present. It can be numerically reproduced by giving a vortex sheet a small sinusoidal excitation. The growth of this instability, obtained from a numerical simulation, is represented in figure 3.11.

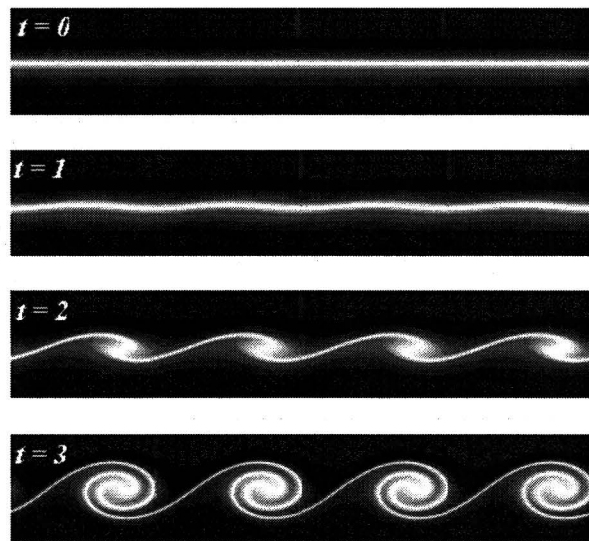


Figure 3.11: Growth of the Kelvin-Helmholtz instability, adopted from *Hu* [Hu97].

Assuming the wavelike motion in figure 3.10 to be induced by the rotating cylinder from the beginning of the measurement, it can be deduced that the shear layer is not strong enough to effectuate break-up into vorticity patches. It is these patches that potentially represent the instability cells that are to be obtained in the experimental set-up.

Although numerical simulations had revealed that blades were not imperative for creating the cell pattern, a certain roughness had to be applied on the cylinder surface. This was done by mounting the blades onto it. The configuration with one blade was found to be ideally suited to study the vortex shedding phenomenon, but did not yield promising results for reproduction of the numerically obtained instability pattern. The rotating body was too asymmetrical for a background Couette flow to develop.

Experiments with more blades did reveal indications towards a cell pattern. The blades are dragged through the fluid, leaving behind a shear layer in their wake. However, the creation of this shear layer is not confined to the wake of the blades, as the jet of fluid thrust forward by the passing of the blade also contributes to this phenomenon. This shear layer rolls up, forming vorticity patches, much as described above and illustrated in figure 3.11. Under the influence of the developing base flow these patches migrate radially outwards being more or less maintained on the plane separating the tangentially moving and the stagnant fluid. Figure 3.12(b) presents a result from a measurement in which 5 wide blades were mounted onto the rotating cylinder. The image domain is located so, that the rotating cylinder is located above it, and so that passing blades are not caught in the images, see figure 3.12(a). The vectors represent the local velocities and the background coloring represents the vorticity. Red patches depict regions of positive vorticity, whereas the blue patches are regions of negative vorticity.

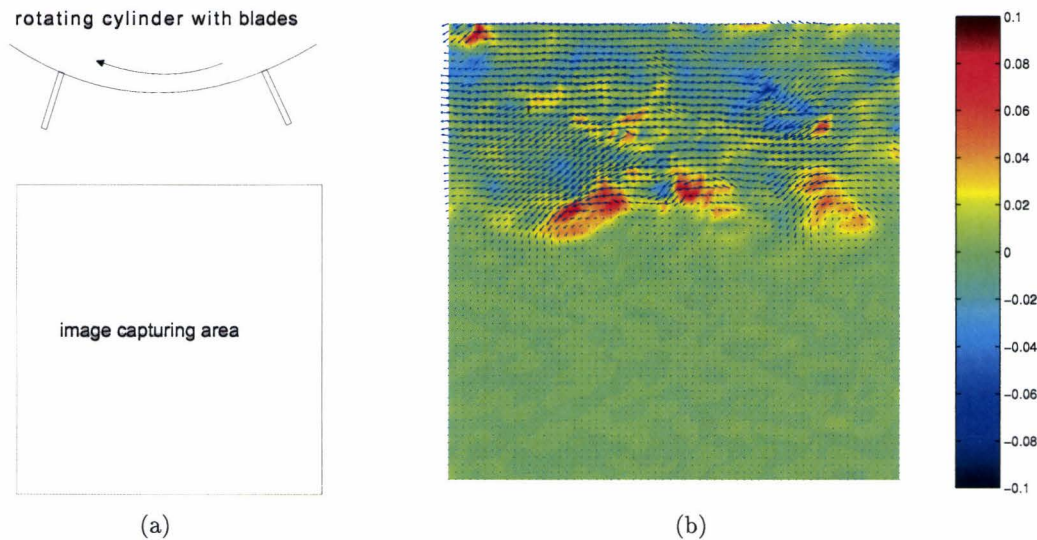


Figure 3.12: Image position elaboration (a) and experimental vortices sustained on the interface (b).

This observation has led to the idea that rotating stall is indeed comparable to a Kelvin-Helmholtz-like phenomenon. The Kelvin-Helmholtz instability can be numerically reproduced by a single vortex layer using the cloud-in-cell technique as proposed by *Christiansen* [Chr73a], which corroborates the observation made earlier, regarding the breaking up of the shear layer. The blades with a width of 30 mm yielded the best results, since the 10 mm blades proved to trigger tangential motion too slowly for an actually distinct separating plane between moving and stagnant fluid to be formed. Also, the optimal number of blades was found to be 5 in these measurements, evenly distributed along the cylinder's circumference. Due to the set-up being flexible with respect to the number of blades and their position, other configurations can be used at any time.

The vorticity patches in figure 3.12(b) could, in crude analogy with rotating stall, be called cells. These cells however, are not persistent as discussed before, whereas in numerical simulations, they did persist many impeller revolutions. This is to be attributed to the solid wall near the diffuser outlet in the experiments, as mentioned earlier in this section. The numerical simulations are based on a radial outflow boundary condition with a constant pressure at the diffuser exit, which is much less constraining than a solid wall. Once simulations were conducted with a geometry alike the experimental one, i.e. with a solid wall near the diffuser exit and no mass flow, interesting observations were made. The structures in these new simulations were not as persistent as the ones in the previous simulations and they moved more slowly. These latest numerical results were much closer to the experimental observations.

Figure 3.13 illustrates how the thus identified vorticity patches rotate about one another, to eventually merge and dissipate. These images are taken from the same measurement as figure 3.12(b) and thus also at the same position.

The weaker vortical structure rotates about the stronger one, i.e. the middle cell rotates about the right one. In the numerical simulations incorporating a solid wall boundary condition, the merging and dissipation of the vorticity patches was also obtained, as was the rotation behavior. Figure 3.14 shows the entire fluid domain and reveals the beginning of vortex interaction.

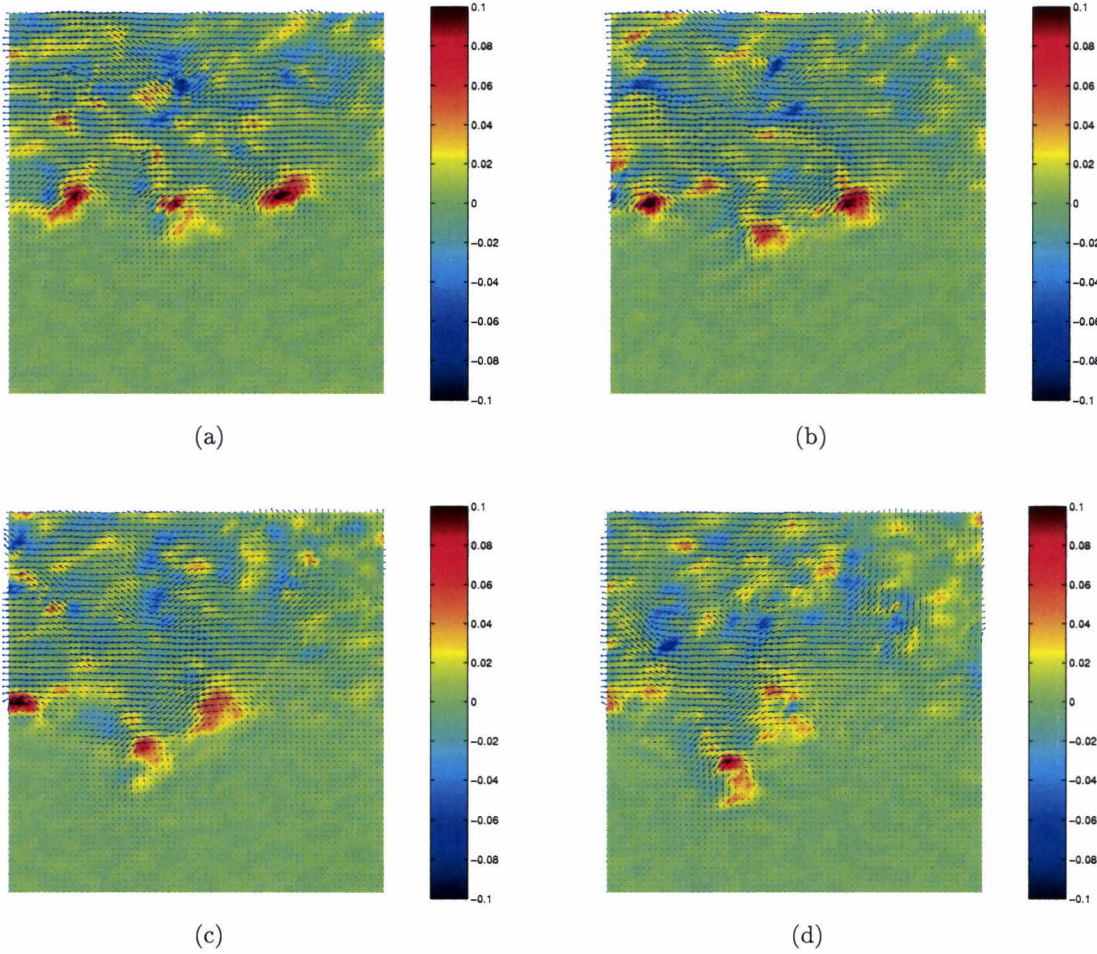


Figure 3.13: The vortex rotating behavior in the set-up.

Vortex interaction is a widely studied topic and in section 2.2.1 it was mentioned that at a distance from the vorticity patch centers, this interaction can be described using a point vortex analogy. A more in-depth discussion of the validity and derivation of this analogy is presented in appendix C.1.

Here, due to its relevance, the interaction between two point vortices shall be briefly discussed. Every point vortex induces a velocity in the fluid particles in its proximity and logically, not in itself. Hence, in a system of two vortices, each vortex is influenced by the other, as already became clear in equations 2.1, 2.2 and 2.3. It can be proven that

$$\frac{d}{dt}[(x_1 - x_2)^2 + (y_1 - y_2)^2] = 0 \quad (3.10)$$

holds, with x_1 and y_1 being the coordinates of one vortex and x_2 and y_2 the coordinates of the other. Equation 3.10 implies that the distance between the two point vortices is constant. Note that the straightforward analogy does not account for vorticity dissipation. For a derivation of equation 3.10 the reader is referred to appendix C.4. Depending on the vortex strengths, the vortices have different movements. Here, the discussion is kept confined to two vortices of

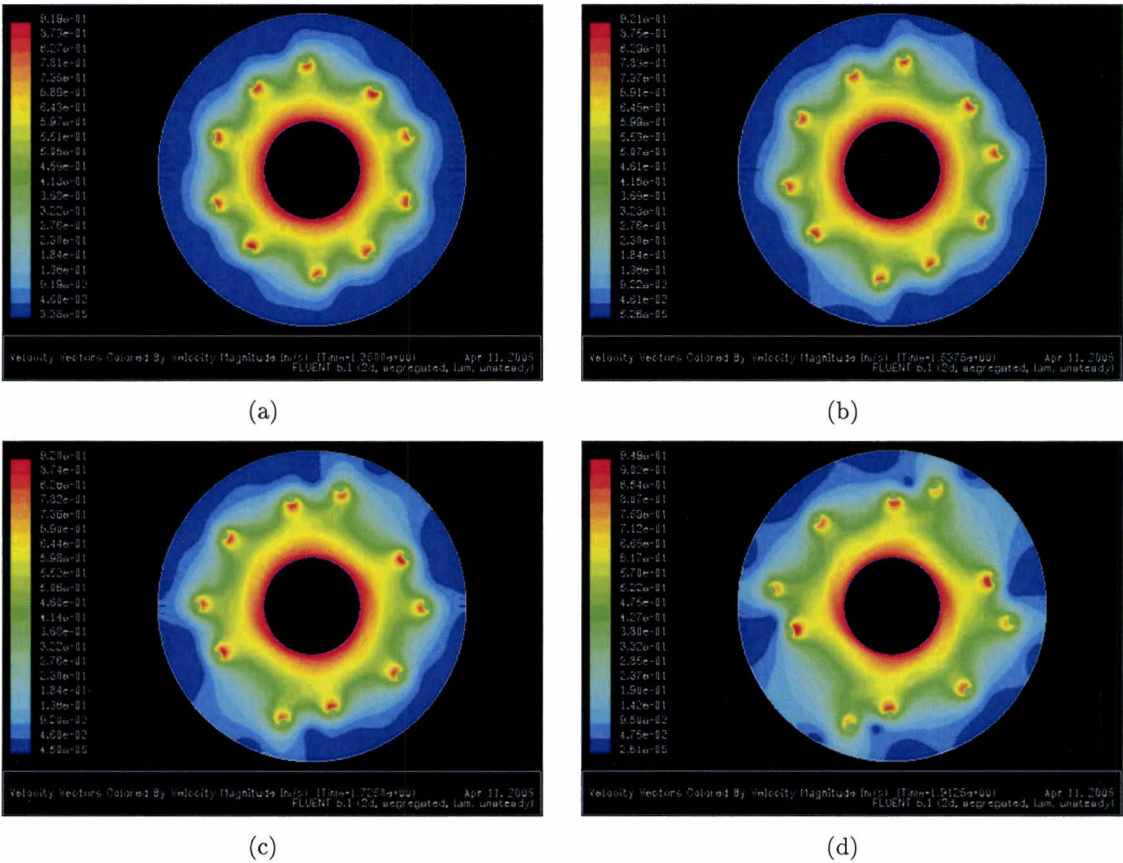


Figure 3.14: The vortex rotating behavior in numerical simulations, FLUENT images.

equal sign. Two identical vortices will move around a common center, which is known as the vorticity centroid and which lies exactly on the center of the line connecting the two vortices. When the vortices are of unequal strength, but equal sign, the movement is slightly different. Now the weaker vortex will make the largest rotation about the vorticity centroid, which in this case is in between the two vortices, but more towards the stronger one. For more information, the reader is referred to appendix C.2. Given the sign and location of the vortices, the weaker one will move outwards and hence, experience less advection of the rotating cylinder. This adds to the vortex interaction leading to the experimentally obtained vortex movements. Corroboration for the observed rotational behavior has now been established both numerically and analytically. The point vortex analogy as it was mentioned in section 2.2.1, and as it is available from the author in a MATLAB script, can be used to study vortex motions of more complex point vortex systems.

In the processed PIV results, one can clearly see that, besides the vorticity patches identified as instability cells, numerous other vortical structures are present in the flow field. A quite logical result, since one can not produce net vorticity. Opposite-signed vortical structures are expected to appear, since it is unlikely that the negative vorticity in the domain will be kept confined to the boundary layers. Hence, the positive vorticity in the cells has to be accompanied by negative vorticity elsewhere, outside the boundary layers. Given the small size of these patches, it was believed that these were small-scale three-dimensional disturbances. An attempt to have these disturbances average out involved using a thicker laser sheet.

3.3.2 Thick sheet horizontal plane measurements

The laser sheet was thickened by merely removing the sheet cut-off. The PIV algorithm determines mean particle displacements in an image segment, so a thicker laser sheet could prove useful to eliminate some of these small three-dimensional effects. The camera was moved a bit towards the cylinder to catch more of the shedding phenomena at the same time.

A first interesting observation was made immediately after the rotation was started. A new vortical interaction has been obtained, which is presented in figure 3.15(b). Numerous small

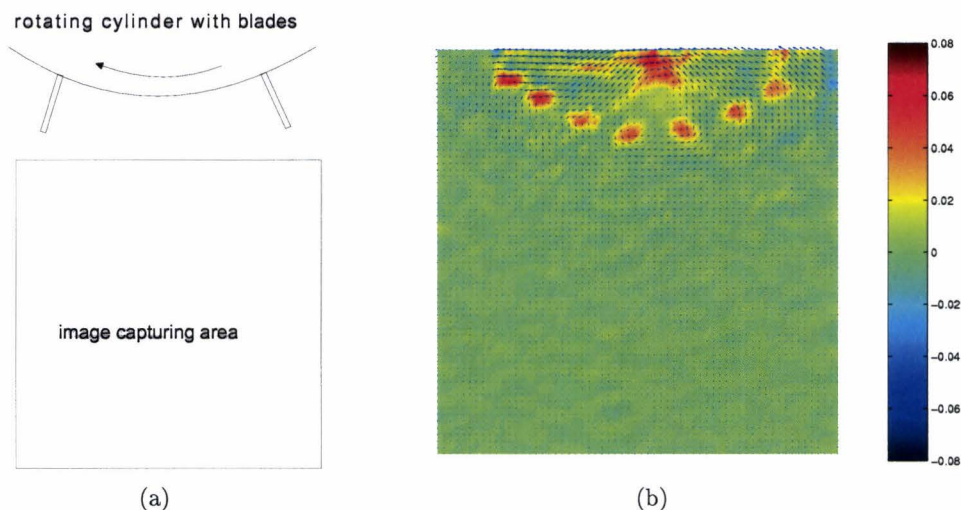


Figure 3.15: Image position elaboration (a) and planetary vortex structure in the set-up (b).

vortices are present and are grouped around a central larger vortical structure. Since they all have equal-signed vorticity, the smaller vortices can not be induced by the larger one. For that to be a valid explanation, the smaller vorticity patches would have to have opposite-signed vorticity with respect to the central vortex. Several other explanations for the emergence and entrapment of the smaller vortices are presented. A first plausible explanation is that these smaller vortices are present due to the breaking up of the shear layer of the forward blade. The shear layer breaks up into smaller vorticity patches which are subsequently entrapped by the tip vortex of the rearward blade. The breaking up of the shear layer can be ‘spontaneously’ due to its own instability or induced by the rearward blade that leaves behind the central vortical structure. The second, and most plausible explanation is that a shear layer is created by the passing of a blade and that the vortices formed after break-up group around the tip vortex of the same blade. This process is visually represented in figure 3.16 and elaborates on the formation of the situation presented in figure 3.15(b). In figure 3.16(a) the shear layer due to the ejected flow is more or less intact and the subsequent images show its gradual breakdown, to eventually form distinct vorticity patches.

An explanation for the fact that these planetary vortex structures have not yet been observed to this extent could lie in the measurement area being a bit closer to the rotating cylinder, but it could also be that the thickness of the laser sheet is the determining factor. When we consider the small vortices to be quasi two-dimensional, meaning that they are two-dimensional disturbances over a small vertical extent, the explanation could be that the thicker laser sheet simply reveals more of them. This idea is schematically represented in figure 3.17. This latter explanation is inconsistent with the very assumption that led to using the thicker laser sheet,

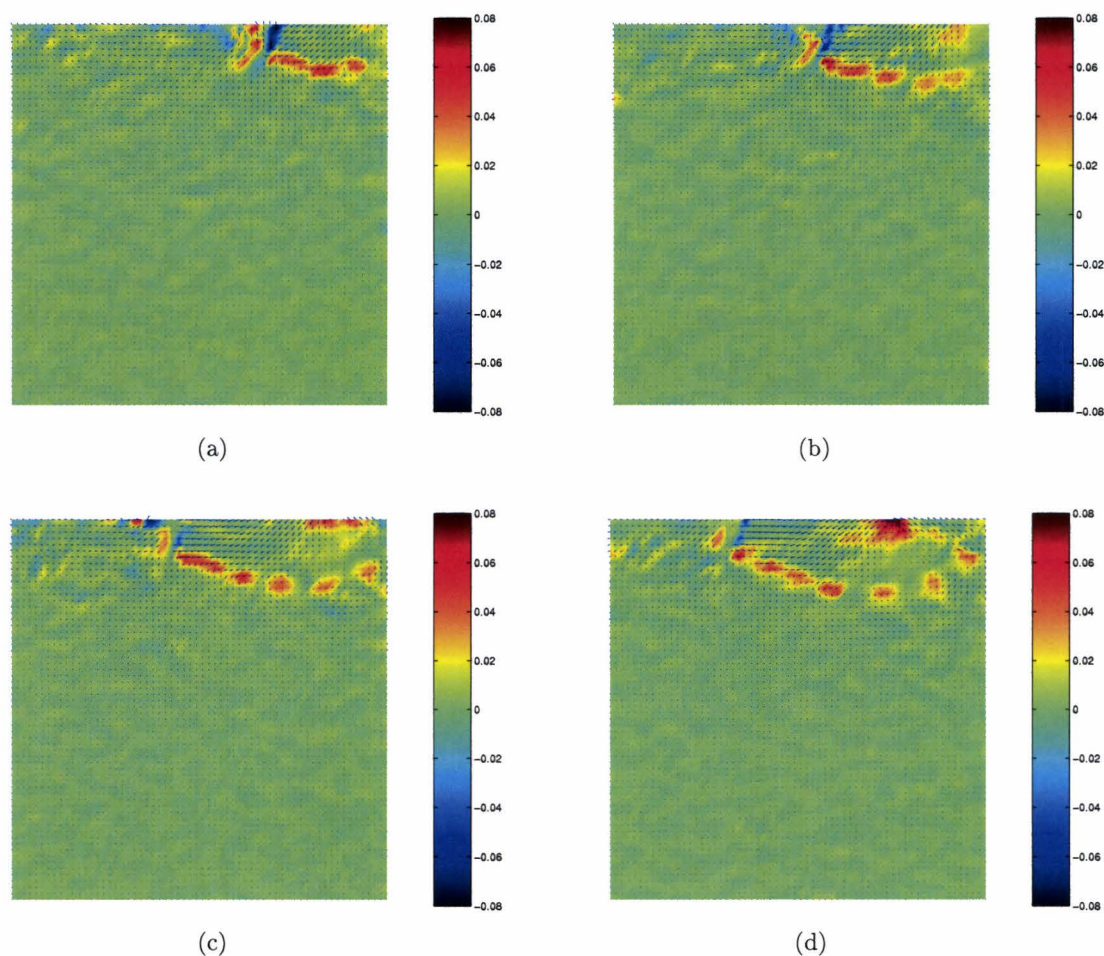


Figure 3.16: The formation of the planetary vortex system.

and therefore considered less plausible than the other. The left part of the figure shows the sheet not illuminating several quasi two-dimensional vortices. These are illuminated in the right part of the figure. Note that the focal depth of the camera also plays a role in capturing the vortices.

The two vortical structures that have been discussed, i.e. the vortices sustained on the flow interface and the planetary vortex system, appear in the same measurement. The first few blade passages bring about the planetary vortex system, whereas the other vortices appear after several impeller revolutions. After these few revolutions, a distinct interface has emerged, on which the vortices are sustained for a while before being viscously annihilated.

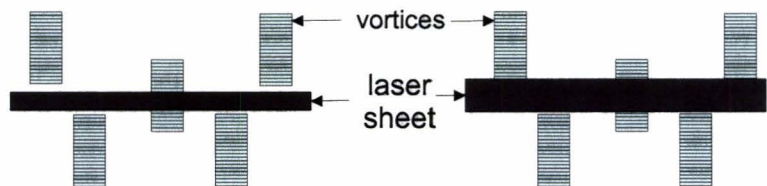


Figure 3.17: Vortices caught in thin and thick laser sheet.

The results after a longer period of time revealed no significant elimination of small-scale disturbances when compared to the results obtained earlier, with a thinner sheet. This led to the assumption that non-trivial three-dimensional motion was present in the set-up.

3.3.3 Vertical plane measurements

To examine the character of the three-dimensional effects in the fluid domain, the set-up was slightly altered. The camera was relocated to the side of the rectangular tank and images were recorded in a vertical plane, using a vertical laser sheet. The rectangular tank that can also be filled with water now proves its worth in mitigating the refraction issues for the camera. Structures with a vertical vorticity axis are very hard to discern in such measurements. Good tuning of the timestep between the correlating laser pulses, the thickness of the laser sheet and the position of the focal plane of the camera is imperative, but extremely difficult. The radial and vertical flows have completely different velocity scales than the tangential flow. The time between the two correlation laser pulses needs to be small enough to capture the particle twice. Within this time, particles also need to make significant radial and/or vertical displacements for the measurements to yield any result. the minimal radial and vertical velocities can be calculated as follows. Acknowledging the minimal particle displacement to be 2 pixels for good correlation and taking the laser sheet to have a thickness of 2 mm, one obtains for the tangential velocity

$$v_t = \frac{d}{\Delta t} \Rightarrow \Delta t = \frac{d}{v_t}, \quad (3.11)$$

with d equal to the thickness of the laser sheet. The distance of 2 pixels can be converted to a distance in mm by multiplying it with the ratio of the image size in mm and the image size in pixels $\frac{L_{im,mm}}{L_{im,pix}}$. Assuming, for the sake of elaboration, this ratio to be $\frac{1}{10}$, one obtains a minimal displacement of 0.2 mm. Equation 3.11 can be substituted into the equation for the minimal in-plane velocities to yield

$$v_{r,min} = v_{v,min} = \frac{\Delta x}{\Delta t} = \frac{L_{im,mm}/L_{im,pix}}{d/v_t} = \frac{0.2 \cdot 10^{-3} v_t}{2 \cdot 10^{-3}} = \frac{v_t}{10}. \quad (3.12)$$

Figure 3.18 gives a schematic representation of the top view of the set-up in these measurements. Part of it is presented enlarged as well, to elaborate on the velocity components, i.e. v_t and v_r for tangential and radial velocity, respectively.

The results from the measurements conducted with this new camera position and laser sheet orientation showed that indeed substantial three-dimensional motion was present in the set-up. In the initial stages of the measurements, an interesting flow was observed, which looked very much like the toroidal rolls formed in the Taylor-Couette instability, as described in section 3.1.1. The flow pattern at one point in the experiments where the manifestation was clearly present is presented in figure 3.19(b).

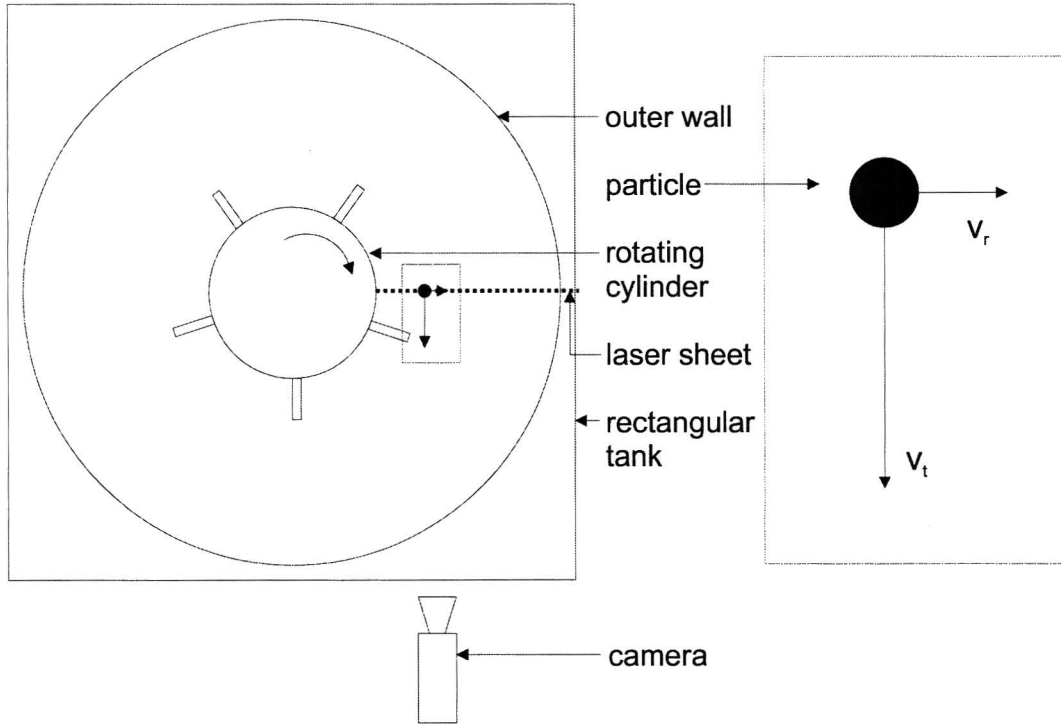


Figure 3.18: Set-up top view in vertical measurements.

Figure 3.19(b) is a result from a measurement with a vertical laser sheet and clearly reveals the presence of two vortical structures in the third dimension. The rotating cylinder is located to the left of the image area, as schematically depicted in figure 3.19(a). The fluid is ejected radially outwards in between the two structures, of which the upper one is the most prominent. The vortices are highlighted by two circles with a rotation indication. The flow pattern in figure 3.19(b) bears strong resemblance to the counter-rotating rolls depicted in figure 3.1. Most of the fluid that is ejected radially outwards tends to move up, probably due to hydrostatic pressure distribution. This kind of motion could also be triggered by the bending of the blades, but since this image was taken at about half the height of the rotating cylinder, this explanation is rendered incorrect. The bending of the blade is neutral halfway its length.

Analysis of this occurrence of the instability recalls the equation for the Taylor number:

$$Ta = \frac{\Omega_i^2 R d^3}{\nu^2}, \quad (3.13)$$

along with the requirements for the instability to develop, being $Ta > 1712$ and $d \ll R_i$. The latter condition was previously the one implying that the Taylor-Couette instability would not occur. However, in the start-up phase of the experiments, the bulk of non-rotating fluid serves as a fictive wall. The measurements need to be conducted in this time interval due to viscous annihilation, see section 3.3.1. This fictive wall, which is obviously much closer to the rotating cylinder, effectively reduces the outer radius in the Taylor-Couette requirements. Taking the new effective gap width to be 0.05 m, the new Taylor-Couette number would be around a factor 100 lower than the original one and thus in the order of magnitude of 10^7 , which still complies with the first condition. The second condition, $d \ll R_i$, comes much closer

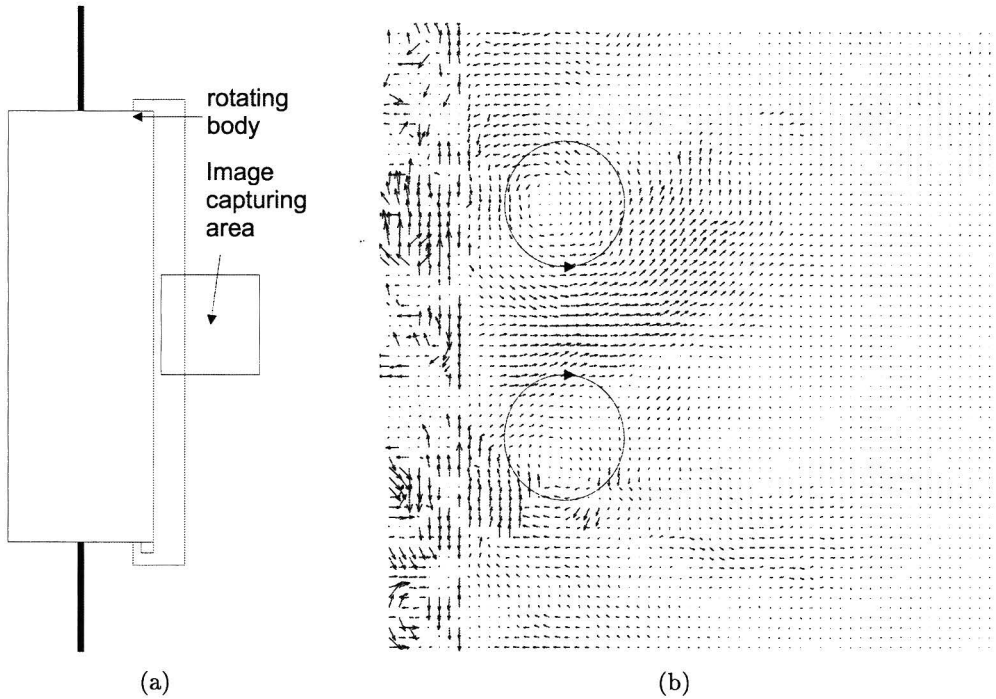


Figure 3.19: Image position elaboration (a) and Taylor-Couette-like rolls (b).

to fulfilment now and the set-up is thus prone to Taylor-Couette-like instabilities, as clearly represented in figure 3.19(b). For convenience, the term Taylor-Couette instability shall be used in the remainder of the report, even though the encountered effects differ from the exact manifestation thereof. In this figure, the seemingly random velocity vectors in the left of the image are due to placement of the camera. This part of the image captures the moving blade and should therefore be ignored in result interpretation.

The Taylor-Couette-like phenomenon as observed in the experimental water model is a temporary and non-uniform feature. The longer the rotation is present, the more fluid is advected, which drives the fictive wall outwards. This causes the radius ratio to eventually leave the range that supports the instability, which makes it disappear. However, the induced three-dimensional effects remain present. The circumferentially non-uniform character of the instability is due to the rotating body being not sufficiently rotational symmetric. The blades mounted onto the rotating cylinder make the case different from the set-up in which a regular Taylor-Couette instability is allowed to develop. Another discrepancy is the fact that the Taylor-Couette instability requires no-slip conditions at the walls, which are not completely satisfied in the experimental set-up, due to the fictive wall.

3.4 Conclusions

As clearly illustrated in this chapter, encouraging results have been obtained. However, due to the presence of three-dimensional effects, the most prominent of which being the Taylor-Couette instability, the two-dimensional instability of the base flow field that is to be studied using the set-up, can not yet be sufficiently identified and isolated. A slight redesign of the current set-up is desired to suppress the Taylor-Couette instability.

Chapter 4

Experimental Set-up Redesign and New Measurements

4.1 The design alterations

In section 3.4 it has been concluded that the experimental set-up needed alteration to suppress three-dimensional motion, or to at least postpone it. As became clear in the previous chapter, it was impossible to suppress the Taylor-Couette instability via the Taylor number or the requirement regarding the gap width within the current set-up. The rotational velocity is not a variable that is freely adjustable, due to a certain required minimal velocity and limitations of the electromotor. The only practically feasible option to accomplish this is to decrease the vertical extent of the domain. This demand may seem contradictory with the already conflicting one stating that the blades should be as long as possible, but this issue was solved. The rotating cylinder remained unaltered, but there was need for a new surface plate; one with a larger hole in the middle to fit over the rotating body. This way, the vertical extent of the fluid domain could be reduced, without introducing the end effect at the lower or upper end of the blades. To avoid having to measure too close to the bottom of the blades, a secondary bottom plate was designed, which is placed 400 mm above the actual tank bottom, as shown in figure 4.1.

Both the surface plate and the new bottom plate need a hole of a little more than 260 mm (rotating cylinder diameter + two blade widths) diameter for a bit of clearance between the rotating blades and the horizontal plates. The two new parts are represented in figure 4.2. The secondary bottom plate is covered with a black foil to reduce laser light scattering and have the illuminated particles stand out more in the images.

Implementing the new parts in the set-up yields, in combination with a shorter lower axis, a new experimental domain roughly halfway the rotating cylinder. Here, the end effects are minimal, if present at all and the blade bending is somewhat neutral. By lowering the water level it is now possible to vary the vertical extent of the domain.

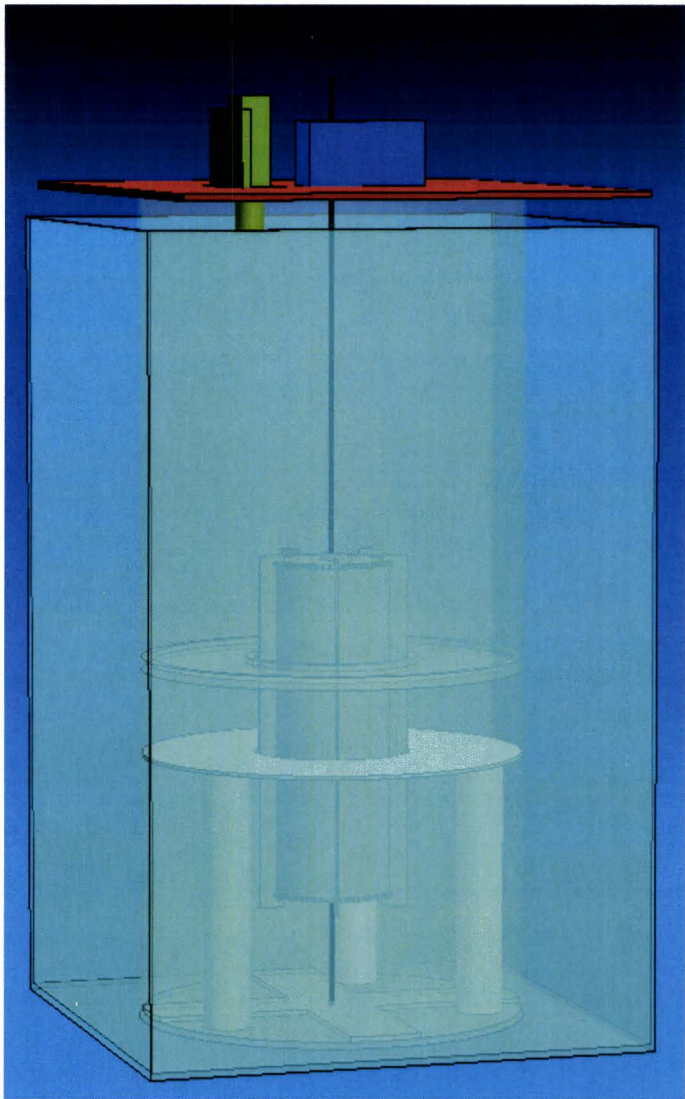


Figure 4.1: The new complete set-up, Unigraphics image.

Expected problems and issues include the measurement initiation timing. The flow has to be at rest, as explained in section 3.3.1, but the particles are prone to sedimentation, which is a bigger issue than before, due to the reduced domain height. Also, particles that end up under the domain's new bottom plate can not easily re-enter the measurement domain. An advantage of the current set-up is that adding seeding (particles) is easier, since there are places where they can be added without removing the surface plate (and thus the top plate). This provided the option to tune the particle concentration without too much effort. The sedimentation issue and the fact that the particles stick to the plates make that a bit harder.

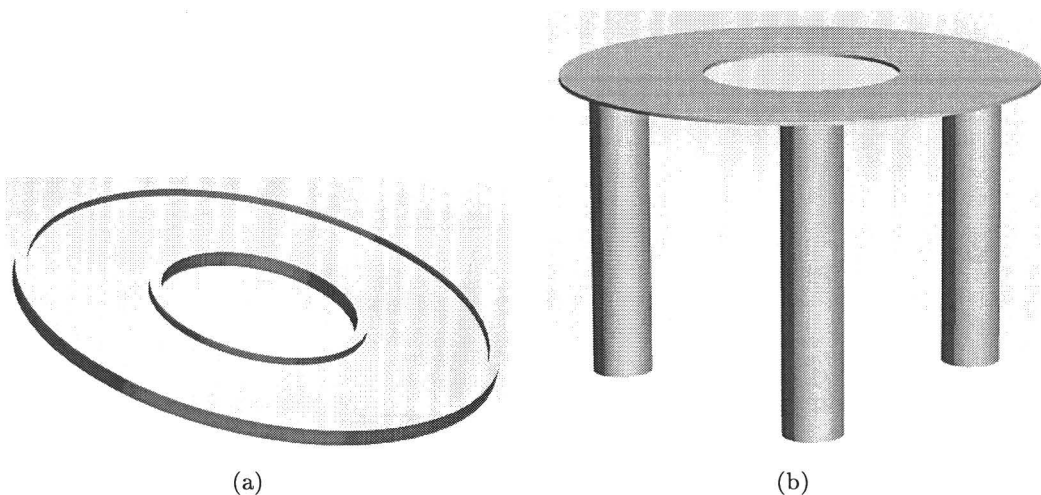


Figure 4.2: New surface plate (a) and secondary bottom (b), Unigraphics images.

4.2 Measurements and results

4.2.1 Vertical plane measurements

The cells as they are present in figure 3.19(b) were estimated to be around 40-50 mm in size. The first reduced vertical domain extent used was 150 mm. This showed no clear indications towards an improvement, which wasn't expected either, since two cells could still easily fit in the domain. An extensive reducing height measurement session was conducted and an interesting observation was made in a measurement where the height was 50 mm. A single cell was present here, see figure 4.3. In this figure, the measurement lay-out is the same as in figure 3.19(b). The horizontal lines in the image are representing the vertical domain boundaries. Above and below these boundaries, the velocity vectors should be ignored, since the particle concentration and lighting are not optimized there. The radially outward flow is again partially directed upwards. Previously, two explanations have been given for this phenomenon, i.e. the bending of the blades and the hydrostatic pressure distribution. The first explanation is again rendered incorrect due to the fact that the measurement was around half the height of the blade. The hydrostatical pressure distribution is believed to trigger the vertical direction of the main radial flow, although the pressure differences are rather small. Note that this is merely a speculation, though corroborated by a series of measurements. Although the cell obtained is again not a Taylor-Couette instability, the need of further domain height reduction was identified.

It is important to assess the boundary layers that will develop on the two plates when further reducing the vertical domain extent. In a boundary layer the inertial forces and the friction forces are in equilibrium, which yields the following relation for a stationary boundary layer, according to *Schlichting* [Sch00]:

$$\mu \frac{U_\infty}{\delta^2} \sim \frac{\rho U_\infty^2}{x}, \quad (4.1)$$

which leads to

$$\delta \sim \sqrt{\frac{\nu x}{U_\infty}}. \quad (4.2)$$

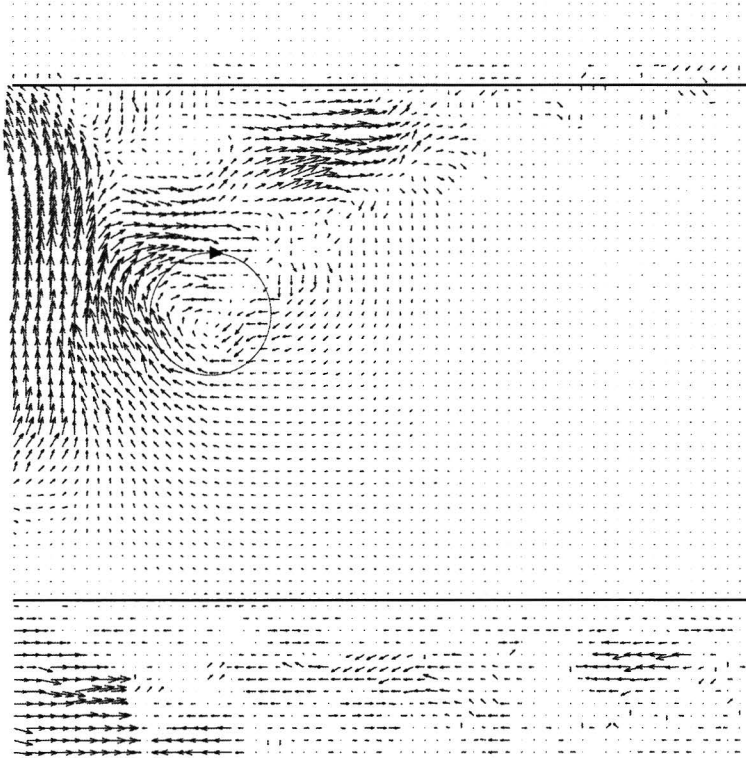


Figure 4.3: Motion in the vertical plane displaying one vortex.

In the above, μ and ν are the dynamic and kinematic viscosity of the medium, U_∞ is the free stream velocity, δ is the boundary layer thickness, ρ is the fluid density and x is the length indication along the plate. When following a similarity variable analysis, for which the interested reader is referred to *Schlichting* [Sch00], one obtains a numerical factor of 5.0 for the laminar boundary layer thickness, when this thickness is defined by the point at which the local velocity is equal to $v = 0.99U_\infty$. In the current analysis however, the definition of displacement thickness is of more use, since this is the thickness that induces motion in the third dimension. The numerical value for this thickness has been found to be around 1.7. Substituting this into equation 4.2 yields

$$\delta_d = 1.7 \sqrt{\frac{\nu x}{U_\infty}}, \quad (4.3)$$

in which the subscript d stands for displacement. The rotating body's circumference is assumed to represent the length in the equation. The velocity is taken to be equal to that of the blade tip of a wide-bladed cylinder at 1 revolution per second. Substituting the above into equation 4.3 yields a displacement thickness of 1.7 mm when the layer is fully developed. Note that in this rough calculation, an assessment at a larger distance from the rotation center would yield the resulting larger length canceling out against the lower velocity. Also, the equation calculates the thickness of a fully developed layer, and whether the layer in the set-up is entirely developed before the measurement ends, is questionable.

Another approach of determining the laminar displacement thickness is taken from *Lighthill* [Lig63] and includes the layer build-up. The relation for the boundary layer thickness, for

small times, is given by

$$\delta = 2\sqrt{\frac{\nu t}{\pi}}. \quad (4.4)$$

Considering the time scale in the experiments, the thickness according to this approach is also in the millimeter range, quite independent of the interpretation of the term ‘small’. A comment on the application of relation 4.4 is that it covers the build-up of a boundary layer in a developed flow. The flow in the set-up is not developed, but developing as well. Hence, one could justifiably argue that the boundary layer is thinner. Having established the relevant layer thickness to be about 2 mm, a vertical domain extent of 10 mm is acceptable. Further reduction can give rise to complications regarding the boundary layers, but would also cause the set-up to not comply with the criterion for wide diffusers anymore.

It is important to realize that the above relations are derived for a straight plate and are being applied to an axisymmetrical flow here. This probably yields a slightly thicker actual boundary layer, but the fact that the flow in the set-up is developing partially counters that. Also, the somewhat pulsating character of the flow is another discrepancy with respect to the cases for which the above equations have been derived. The conclusion of this boundary layer assessment is that the two boundary layers will develop, but will not influence the main flow in the middle of the domain too much when using vertical domain extents greater than 10 mm.

Measurements were carried out with numerous different domain heights, and in the remainder of this section some results are presented for heights of 30, 20 and 10 mm.

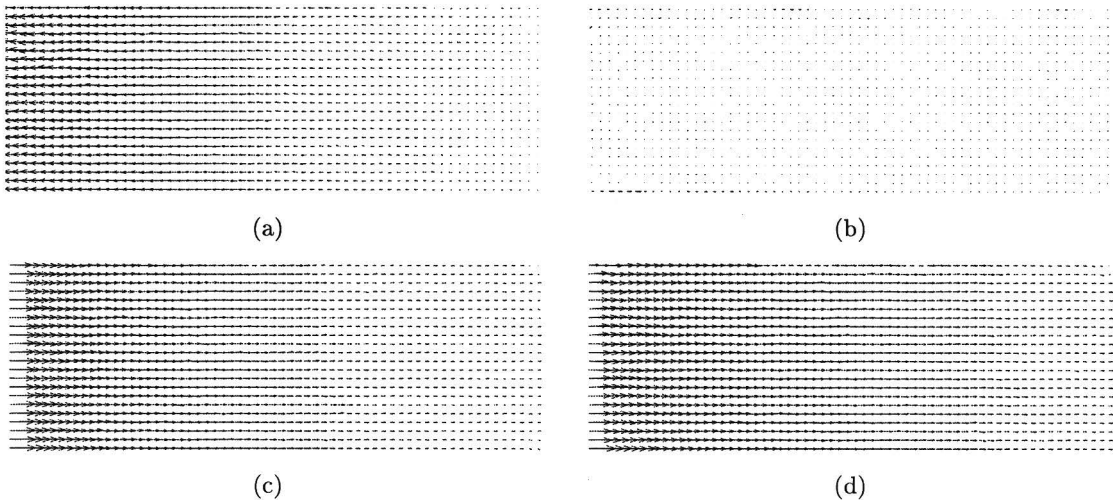


Figure 4.4: Two-dimensional flow pattern over entire domain height at $t < t_{crit}$ (30 mm).

Figure 4.4 shows four consecutive flow field correlations for a measurement in which the domain height was chosen to be 30 mm. These images have been edited, to show only the relevant data. Above and below the region of interest are the two plates that limit the vertical domain extent and the useless data there is not presented. In the first image the radial velocity component is directed inwards, whereas in the third and forth, it is directed outwards. These two flows are ‘separated’ by one frame deprived of radial motion. This image sequence reveals

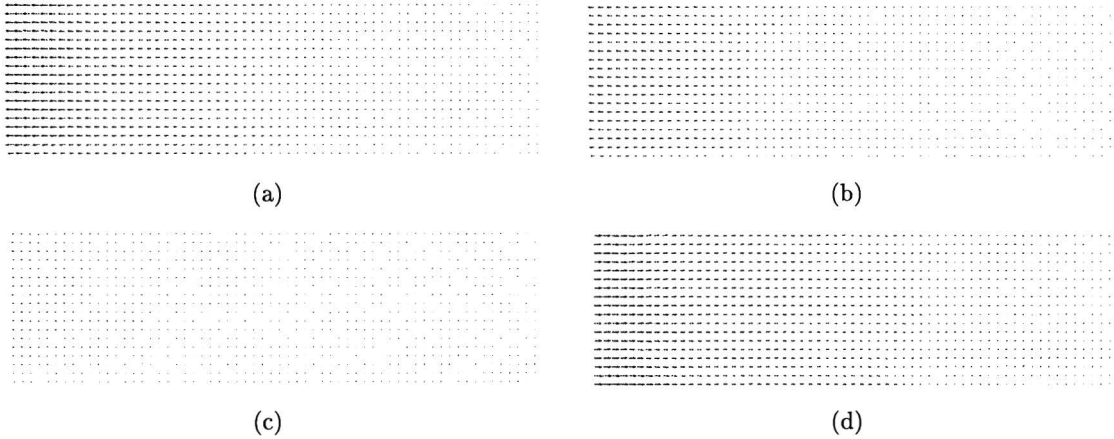


Figure 4.5: Two-dimensional flow pattern over entire domain height $t < t_{crit}$ (20 mm).

the presence of a two-dimensional flow field.

A similar sequence of results is given for a measurement with a vertical domain extent of 20 mm in figure 4.5 and for 10 mm in figure 4.6. All these image sequences contain indications towards a two-dimension flow pattern over the entire domain height before a vortical structure, or any other vertical motion is identified. One clearly identifies a radially outward flow being followed by a radially inward one, or vice versa. This was not the case in measurements with a larger vertical domain extent. In those configurations, no two-dimensional flow pattern ever arose.

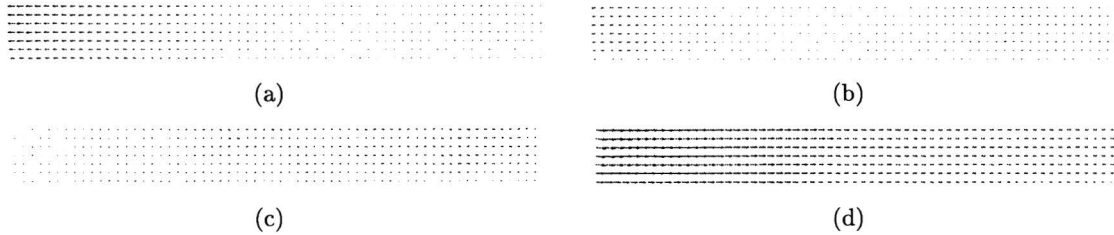


Figure 4.6: Two-dimensional flow pattern over entire domain height $t < t_{crit}$ (10 mm).

When recalling equation 3.4 and substituting 0.01 m for d , one comes to the conclusion that the Taylor number is still an order above the critical value (10^5). This value was taken, since Taylor-Couette cells tend to be round and a vertical domain extent of 0.01 m can contain one cell with a diameter of about 0.01 m. Although this possible single-cell manifestation (as opposed to a stacking of oppositely rotating rolls) is not identified as the Taylor-Couette instability, it does bear some resemblance to it. For this reason the analysis is believed to be justifiably extrapolated to the single roll. Hence, although it is obvious that the domain height reduction is the reason for the suppression of the three-dimensional effects, the absence of the rolls is not to be predicted using equation 3.4.

The domain height reduction procedure has been successful in suppressing the immediate onset of three-dimensional motion. However, later on in the measurements three-dimensional motion was again observed, so the conclusion is drawn that three-dimensional motion can be postponed, though not eliminated altogether. The time at which three-dimensional motion

sets in is called the critical time t_{crit} and is larger for smaller domain heights. Figure 4.7 reveals the initiation of three-dimensional motion in the 20 mm domain and figure 4.8 in the 10 mm domain.

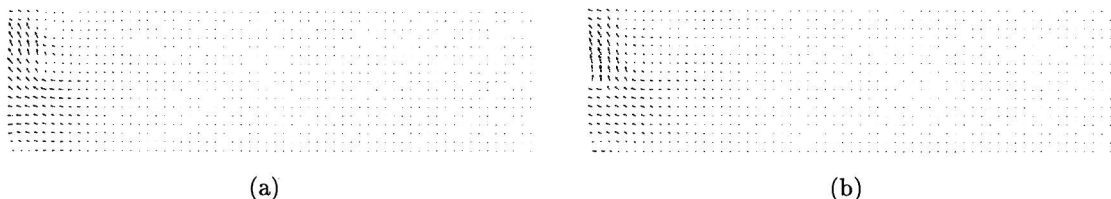


Figure 4.7: Initiation of three-dimensional effects when using a height of 20 mm ($t > t_{crit}$).

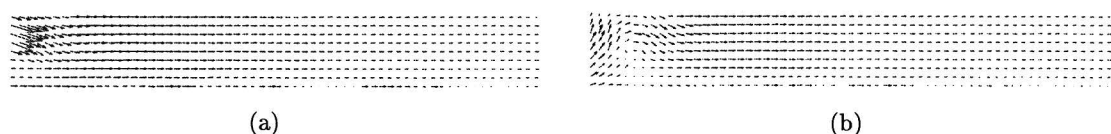


Figure 4.8: Initiation of three-dimensional effects when using a height of 10 mm ($t > t_{crit}$).

The validity and effectiveness of the domain height reduction approach in trying to obtain a two-dimensional flow pattern is corroborated by the fact that with increasing height reduction, the postponement is larger. The occurrence of three-dimensional effects in these measurements is not due to effects alike the Taylor-Couette instability. The motion is most likely induced by the collision of two jet flows.

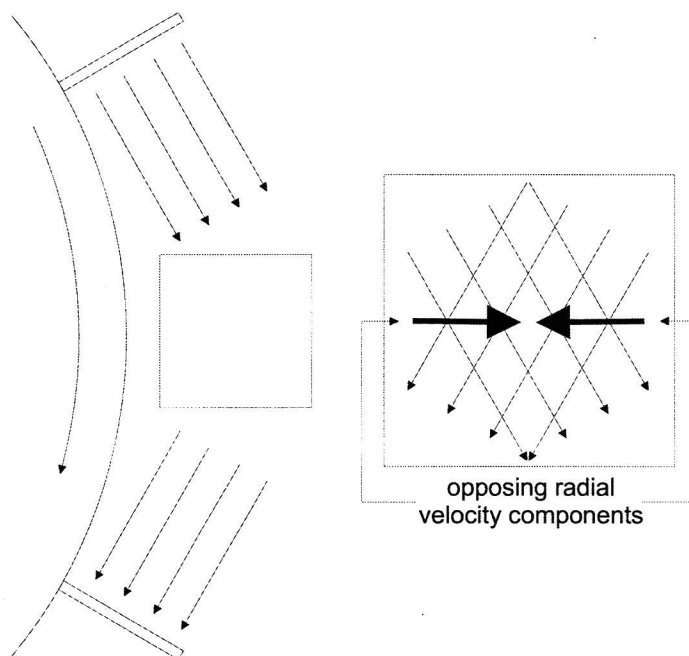


Figure 4.9: Top view of a side of the set-up with jet collision.

In the figures 4.4 to 4.6 there are images in which the radial velocity is approximately zero.

Hence, one does not expect three-dimensional motion, but as the fluid velocity gradually increases, this moment of ‘rest’ in the radial direction vanishes. The collision of the two jet flows is depicted in figure 4.9. One flow is in the wake of the forward blade, while the other is an ejected jet from the rearward blade. The radial components of these two flows are opposite to each other. Part of the fluid has to be redirected as a result of continuity for an incompressible fluid, which causes the motion in the third direction. The fact that the three-dimensional motion was postponed was encouraging enough to return to the original measurement orientation, though with the new set-up incorporating the new surface plate and the secondary bottom plate.

4.2.2 The sticking particle problem

The new measurement configuration inextricably implied that both the new surface plate, as depicted in figure 4.2(a) and the secondary bottom plate, as depicted in figure 4.2(b) are close to the laser sheet. This is schematically represented in figure 4.10. For measurements in a horizontal plane, this leads to complications. The illuminated particles in the sheet scatter light, which is one of the basic principles of particle image velocimetry. However, since they do this, they indirectly illuminate other particles in their proximity. Other refractive issues, such as the cylindrical tank’s poor surface condition also contribute to this indirect illumination.

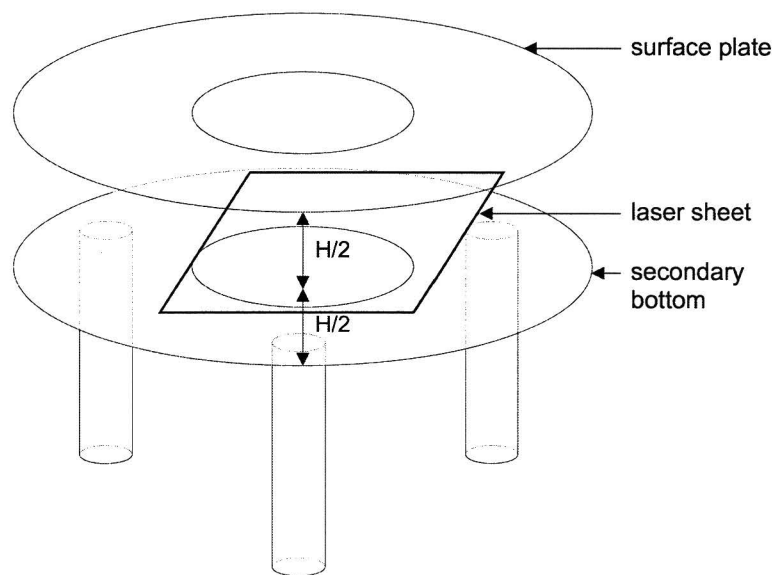


Figure 4.10: Depiction of proximity of laser sheet.

This indirect illumination can become problematic. The 20 micron seeding particles are prone to sedimentation and they will therefore sink to the bottom after some time and remain there. Also, particles that are on the water surface will end up sticking to the surface plate. The process of adding particles to a base concentration to obtain the best particle concentration as described in section 4.1 also proved impossible, for the jet that is created leaves particles behind on both of the plates. Where these sticking particles were not a problem in the first configuration of the experimental set-up, they complicate matters considerably here. A schematic representation of a side-view is presented in figure 4.11.

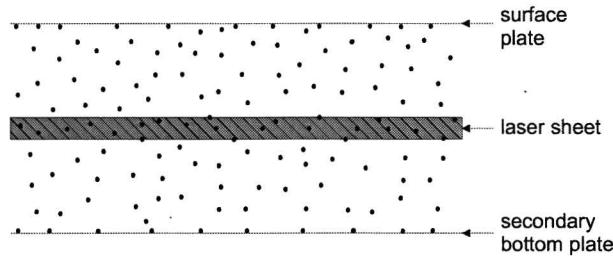


Figure 4.11: Set-up side view, vertical and particle size exaggeration.

The particles in the laser sheet are the ones that are directly illuminated by the laser sheet and the ones whose motion is of primary interest. The particles outside the laser sheet are illuminated indirectly. The focal depth of the high-speed camera is too large to have only particles in the laser sheet in focus and particles over the entire domain height are visible in the images. The indirectly illuminated particles in between the secondary bottom plate and the laser sheet and in between the laser sheet and the surface plate do not constitute a problem. This is due to the two-dimensional flow pattern that has been obtained before the critical time at which motion in the third dimension commences. The motion of these particles does not differ from the motion inside the laser sheet, see figures 4.4, 4.5 and 4.6. The particles stuck on the horizontal surfaces are the ones that hinder the correlation process if illuminated.

The PIV algorithm determines mean particle displacements in image segments. Hence, stuck particles influence its result to a great extent, which leads to inaccurate representations of flow patterns. Averaging unprocessed images and subtracting the average from all the images is a way of solving the problem to some extent. However, for this method to work, a lot of images should be included in the averaging, taking into consideration the fact that odd and even numbered images should be treated separately due to probable illumination intensity differences. The fact that one should include a lot of images in the averaging process indicates that during a relatively large time span the surface plate itself may not move even the slightest bit.

Identification of vortical structures in these flow patterns was found to be impossible. Attempts to solve the problem have included the use of different particles, the optimization of the laser sheet thickness and eventually optimizing the experimental procedure.

Different particles

The biggest contribution to this sticking particle phenomenon was found to be due to the surface plate, which was initially attributed to the material types. The surface plate is made out of perspex and the particle material is polyamid. Both of these are synthetic materials and are prone to static attraction, which can lead to the particles sticking to the surface. A different type of particles, hollow glass spheres with an average diameter 20 microns, was used in order to solve this. A suspension of these particles was easier to make and the particles were less susceptible to floating on the water surface due to surface tension. This was considered encouraging enough to try new measurements with these particles. The resulting improvement was marginal, for the improvement regarding the number of particles stuck on the surface plate was countered by more prominent sedimentation. Also, polyamid particles of a larger diameter, viz. 50 microns were used, which again yielded improvement, but not to the desired extent.

Other measures had to be taken in order to perform the measurements and extract useful data. The polyamid seeding particles with an average diameter of 50 microns were used in all following experiments.

Laser sheet cut-off

The thinner the laser sheet cut-off is, the less light will be scattered by particles in the sheet and this scattering will be kept more confined than when the sheet is thicker. Thus, the thinner a laser sheet is cut, the less of a problem the sticking particles will be. A thin sheet is thus desirable, provided its intensity is high enough, so there's a trade-off here. Also, the bundle intensity maxima of the two correlation pulses of the laser do not exactly coincide. As a direct consequence, the intensity maxima of the sheets, located in the their middle, are at different vertical positions. Intensity differences between the two images of a correlation pair are bound to complicate the correlation procedure. An extreme case is that perfectly illuminated images are accompanied by utterly black ones, leading to no correlation possibilities whatsoever. This latter case would indicate that the sheet cut-off let the most intense part of the one sheet pass, where it stopped all light from the other. Optimization is more difficult for a thinner laser sheet.

In the horizontal direction, a similar criterion holds and one should make sure that the region in which the flow pattern is to be obtained is completely illuminated by both laser sheets. Failing in doing so will lead to part of the one image of a correlation pair being black or insufficiently illuminated. This also leads to general correlation failure and useless flow patterns. Figure 4.12 represents an ideal situation regarding the sheet cut-off position for the given sheet positions.

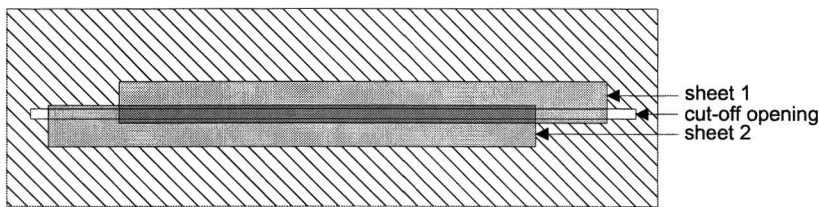


Figure 4.12: The two different laser sheet positions, exaggerated view.

Of course, had the sheets been coinciding to a higher degree, one would obtain a better situation. Over the entire height of the cut-off opening, both laser sheets are represented. This has been achieved in the experimental set-up, which proved to be another step towards obtaining good measurement results.

Experimental procedure

Due to the sedimentation and particles sticking to the plates, the experiment has to be carried out as quickly as possible. Everything that can be done in advance should be finished before adding the particle suspension:

- laser alignment (check image area illumination by both sheets),

- camera focussing,
- identify camera, set its parameters, create a new video file and set recording parameters,
- set delay generator parameters,
- clean the tank and especially the two plates,
- prepare particle suspension and measure off the amount to add,
- fill the tank and remove any air bubbles that may be present under the bottom plate,
- set the water height to the desired level; 30 mm has been used successfully.

The remaining things need to be done as quickly as possible:

- add the particle suspension at about half the domain height and mix it with the water,
- lower the surface plate and avoid including air bubbles,
- put the top plate on top of the set-up, fix the axis in the motor and connect all cables,
- start measurement after ensuring sharp images and start the impeller rotation.

When everything in the above list has been carried out perfectly, incorporating the issues raised in the preceding paragraphs, good measurement data is likely to follow. A more elaborate discussion of the above steps can be found in appendix G, in which the latest measurement protocol is presented.

4.2.3 Horizontal measurements

A measurement method for studying the two-dimensional core flow in the experimental set-up has now been fully developed. The interest is in the occurring fluid mechanics before the three-dimensional motion sets in. The fluid mechanics that occur after this critical time include the switch from 2D to 3D flow and the subsequent three-dimensional patterns that develop. These three-dimensional structures need to be avoided during the measurement time interval. These phenomena are, albeit very interesting, beyond the scope of the present study. In the measurements, vorticity patches were observed before three-dimensional motion sets in, i.e. at $t < t_{crit}$. These patches have a vorticity with a sign opposite to the cylinder rotation and move in the same direction as the blades do, yet at a reduced speed, see figure 4.13. Also, the development of an opposite-signed vorticity patch is visible.

In figure 4.13 the rotating cylinder is at the bottom of the images, whereas in figures 3.12(b) and 3.13 it is at the top of the images. For the rest the measurement position is the same and thus a rotation over 180° would yield the exact same image orientation. The vortical structure obtained in these latest measurements is larger than those observed earlier and presented in figure 3.12(b). This can be even more clearly illustrated by enlarging the part of the image where the vortex is located and leaving out the vorticity on the background. Figure 4.14 shows the vortical structure and reveals that the fluid surrounding the vortex core, indicated by a red color in figure 4.13(b) is also part of the entire vortical structure. The structure is about 50 mm, whereas the vorticity patches in the other experiments were about 20 mm.

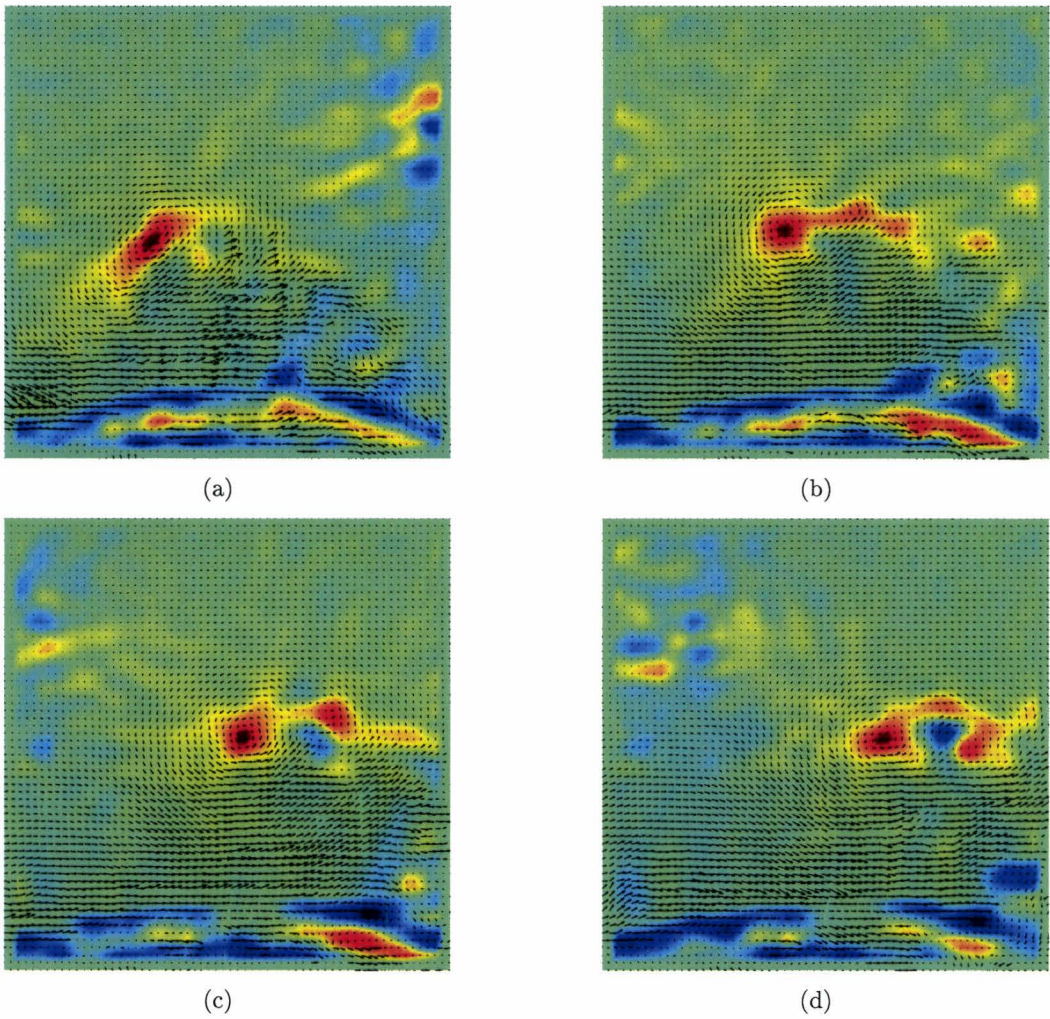


Figure 4.13: Vorticity patch motion in the 2D regime, i.e. $t < t_{crit}$.

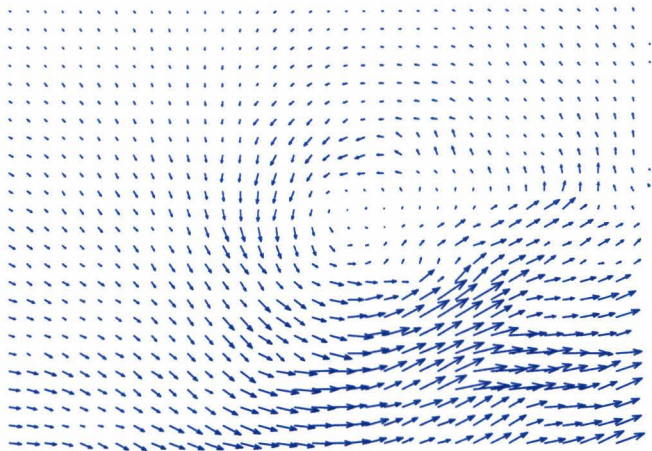


Figure 4.14: The main vortical structure from figure 4.13(b).

In the unprocessed images, one can still see the tip of the blade passing, which allows for a calculation of the cylinder rotational speed. In the correlated images of pairs 83&84, 93&94 and 103&104, a blade tip is visible at about the same position. In figure 4.15 the correlated images of the pairs 83&84 and 103&104 are shown, along with the images themselves.

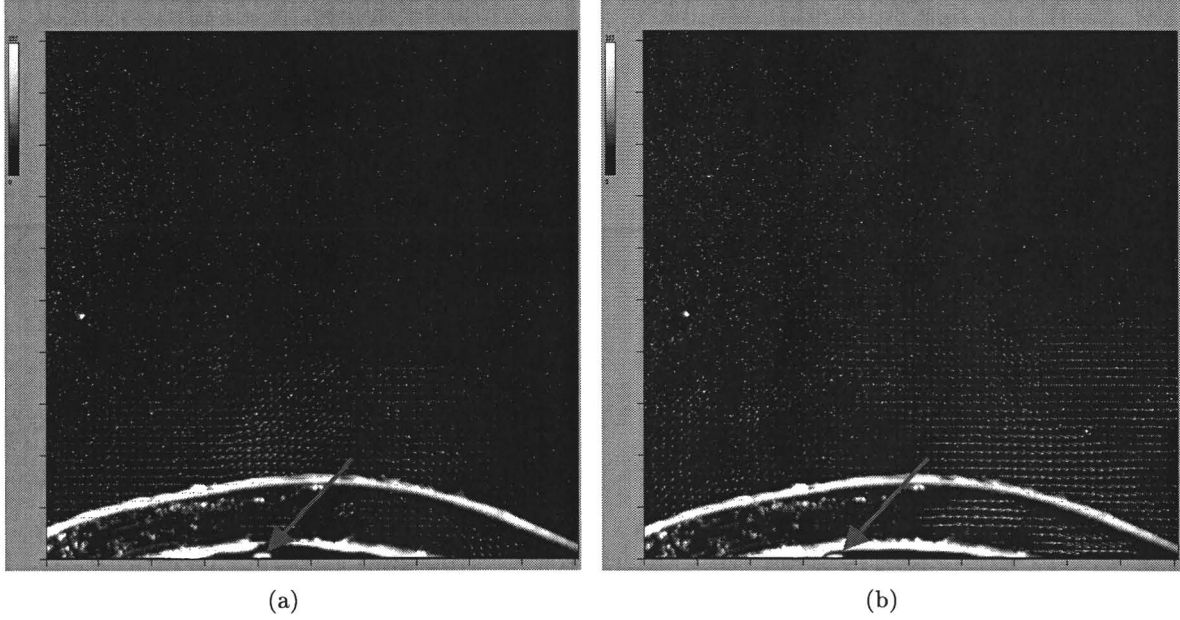


Figure 4.15: Illustration of a passing blade, PIVview images.

An easy deduction yields the insight that 10 images, or 5 image pairs capture 1 blade passage. The frequency of the laser is 15 Hz (15 pairs of two correlation pulses), which leads to 3 passing blades per second and hence $\frac{3}{5}$ revolutions per second. The blade tip speed is then calculated as

$$U = 2\pi r n = 817 \cdot \frac{3}{5} = 490 \text{ mm/s.} \quad (4.5)$$

The time between the first and the last image in figure 4.13 is $\frac{6}{15}$ th of a second. Due to the difficulties in calibration and the predominantly qualitative nature of the endeavor, no exact distances or velocities can be presented. An estimation reveals that the image covers 120 mm. This information can be used to estimate the distance the vortex has traveled in this time, which is 40 mm. The velocity can thus be calculated as

$$v = \frac{\Delta x}{\Delta t} = \frac{40}{\frac{6}{15}} = 100 \text{ mm/s.} \quad (4.6)$$

It can now be deduced that the vortex speed is about 20 % of the impeller speed. Assessing this in terms of rotational speed requires a multiplication by the radius ratio of the impeller tip path and the vortex path. The distance between the vortical structure and the blade tip is about half of the image area, i.e. 60 mm, leading to a path radius of 190 mm. Hence, in

terms of rotational speed a percentage about 14 % is obtained:

$$\frac{\omega_{vort}}{\omega_{imp}} = \frac{v_{vort}/r_{vort}}{v_{imp}/r_{imp}} = \frac{v_{vort}}{v_{imp}} \cdot \frac{r_{imp}}{r_{vort}} = \frac{100}{490} \cdot \frac{130}{190} = 0.14. \quad (4.7)$$

This value is lower, which is expected, since a certain tangential velocity covers less of the circumference at a higher radius, as illustrated in figure 4.16.

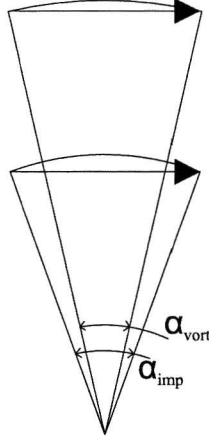


Figure 4.16: Illustration of rotation angles for the same velocities.

Chapter 5

Comparison with Numerical Results and Experiments

5.1 Comparisons with numerical results

5.1.1 Vortex size

An image from a numerical simulations devoid of net impeller outflow and with the exact same geometry as the experiments reveals that per jet-wake two vortical structures develop, see figure 5.1(a). In this image, a boxed area is shown, which would represent the size of the experimental image capturing area. Figure 5.1(b) presents one of the images from figure

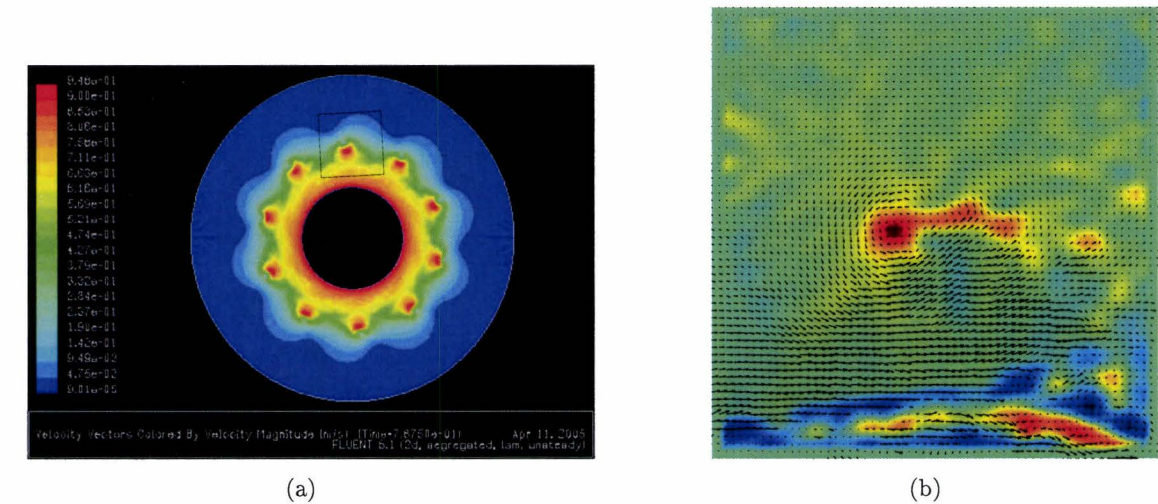


Figure 5.1: Numerical simulation (a) and experimental result (b) displaying vortical structures.

4.13. It is repeated that in the numerical simulation, the coloring is according to velocity magnitude, whereas in the processed images from the measurements, the coloring is according to vorticity magnitude. So where in the processed experimental result the red area indicates the center of the vortex, a red patch in the numerical result indicates the high velocity area below a vortex. The velocity is high here since the contributions of the cylinder rotation and the vortex itself coincide here. Striking resemblance is observed when one looks at the vortical structure size. In both figures, an estimation would yield a size of around 50 mm.

5.1.2 Approximation of the number of vortices

The flow pattern depicted in figure 5.1(b) is now assumed to be present over the entire experimental set-up circumference, as is the case in the numerical simulation, see figure 5.1(a). This is a rather crude, but not entirely unphysical approximation and allows for the following deduction to be made. The image size is 120 mm and the circumference of circle with a radius of 190 mm is calculated as

$$2\pi r = 1194 \text{ mm.} \quad (5.1)$$

Now employing the above described assumption, a division of the circumference by 120 would yield 10 vorticity patches. Recalling that numerically, two vortices per simulated blade are obtained, the conclusion can be drawn that this crude analysis provides another corroboration.

5.1.3 Propagation speed ratio

As calculated in the previous chapter, the experimentally obtained vortex rotates at a frequency of 14 % of that of the rotating cylinder. Now the propagation ratio for the numerical result will be derived. The numerical output reveals a rotation over one fourth of the numerical domain in the time span between 0.86 and 2.10 seconds. The trivial derivation of the rotational speed then runs

$$n_{vort} = \frac{1/4}{2.10 - 0.86} = 0.20 \text{ s}^{-1}. \quad (5.2)$$

In the simulations, a cylinder speed of 1.0 m/s was used. The rotational speed can then be calculated by dividing this velocity by the cylinder circumference:

$$n_{cyl} = \frac{U}{2\pi r_{cyl}} = \frac{1.0}{2\pi 0.10} = 1.59 \text{ s}^{-1}. \quad (5.3)$$

This makes the propagation ratio $\frac{0.20}{1.59} = 0.13 = 13 \%$. Thus, the experiments corroborate the numerical simulations to a very high degree in this respect.

5.1.4 Opposite vorticity presence

When looking at the image in figure 5.1(b) which has already been estimated to be 120 mm in size and recalling from figure 4.15 that the blades are just below this figure, one comes to the conclusion that the presented vortical structure is located at 60 mm from the blade tips. A short while later, at this same radial distance, the development of a distinct area of opposite-signed vorticity is identified, see figure 4.13(d). The formation of the clockwise (blue) vorticity patch in the experiments is thus at about 60 mm from the blade tip. Recalling equation 3.3

$$\frac{D_3}{D_2} = 1.52 \quad (5.4)$$

and identifying that D_2 equals 260 mm yields the insight that the two vortices are near the

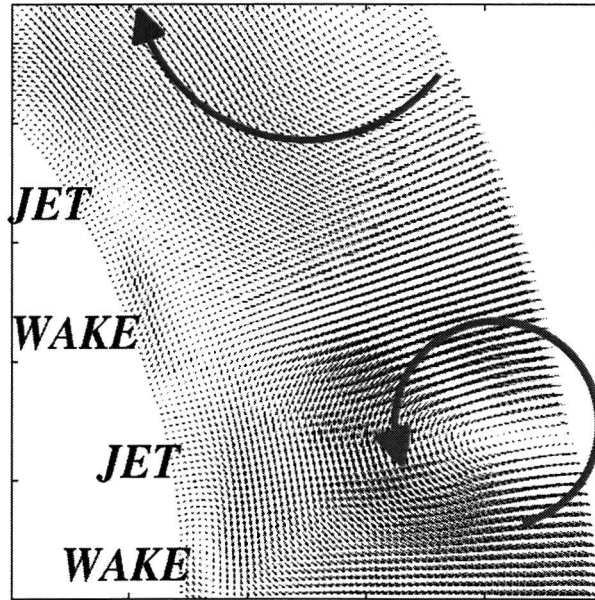


Figure 5.2: Counter-rotating vortex pair near the diffuser outlet.

diffuser exit, i.e. the fictive outflow as described in section 3.1.1.

This has also been observed numerically, as depicted in figure 5.2. The two vortices, a clockwise and a counter-clockwise specimen, are located near the diffuser exit. The lower arrow depicts the rotation of the positive vorticity patch and the upper arrow indicates a negative vorticity region. The terms ‘jet’ and ‘wake’ at the diffuser inlet refer to the employed rotating jet-wake pattern, which rotates clock-wise. Of course, one can not state that these numerically obtained vortices are a representation of the exact same things that have been observed experimentally, but strong similarities are present nonetheless.

5.2 Comparisons with other experiments

5.2.1 Propagation speed ratio

As calculated in the previous chapter and addressed in comparison to numerical results in section 5.1.3, the vortical structure moves at about 20 % of the impeller tip speed, or equivalently, 14 % of the impeller rotational speed. Using the interval given by *Kämmer & Rautenberg* [Käm86] as presented in section 1.1.3 for stall cell rotational speed and applying it to the obtained core flow instability, one concludes that this value lies in the lower part of the interval. This would, should the vortex be likened to a stall cell, indicate that it is a large manifestation of such an instability cell. Figure 4.14 reveals that indeed the vortex is quite large for the given diffuser size, for it would nearly encompass the entire radial extent. However, for centrifugal compressor stall the note was made that the lowest values in the interval were attributed to combined diffuser and impeller stall, indicating that diffuser stall may generally have a lower rotating speed. This deduction is corroborated by observations by *Jansen* [Jan64] who used a rotating screen as impeller and observed that a pattern with few cells rotates at a speed of less than 10 % of that of the screen rotation. Moreover, simulations showed that the incorporation

of a solid wall rather than a radial through-flow significantly reduces the vortex rotational speed.

5.2.2 Opposite vorticity presence

In another experiment a counter-rotating vortex pair was also observed. Figure 5.3 presents two images from PIV measurements in an air flow through an optically accessible wide vaneless diffuser of radial flow pump, as adopted from *Ljevar et al.* [Lje06].

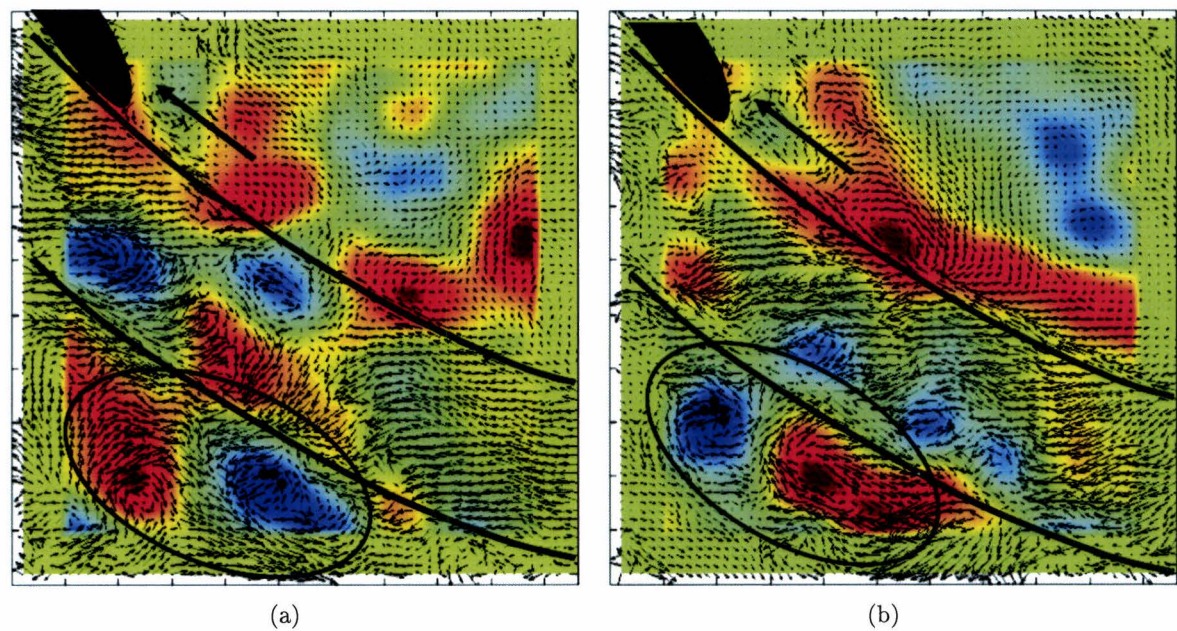


Figure 5.3: Visualization of a vaneless diffuser flow displaying a counter-rotating vortex pair.

In these figures, the vorticity scaling is opposite to all other figures presented in this report. Previously all vortices with counter-clockwise rotation were defined as having positive vorticity, and were represented as red patches. However, the images in figure 5.3 present these vortices as blue patches. The two curved lines running through the images are the diffuser inlet and its outlet and the arrow depicts the impeller rotation. The black dot in the upper left corner of the images represents an impeller blade that has just passed. Both images in the figure reveal a counter-rotating vortex pair near the diffuser outlet, which is another corroboration of the numerical results as well as the experiments carried out in the water model. A more in-depth comparison between the water model and the experiments in the diffuser of the radial flow pump can not be conducted, due to lack of detailed experimental data of the latter. Note that in these images, also direct blade effects are visible, i.e. trailing vortices in the blade's wake. Where the initial realization of the water model was suited to present these phenomena, the latest alterations to the measurement lay-out eliminated this possibility. The edges on the inner part of the new surface plate do not allow for accurate correlation. These edges are visible in the bottom part of the images in figure 4.15.

Chapter 6

Conclusions and Recommendations

6.1 Conclusions

For the purpose of rotating stall research, an air compressor has been scaled to a water model using the universal scaling laws for rotating machinery. The impeller outflow was neglected and the research was aimed at studying the two-dimensional core flow instability of the flow inside a wide parallel-walled vaneless diffuser of a centrifugal compressor. The flow was triggered by a rotating cylinder with blades mounted onto it. The jets ejected by passing blades served as an approximation of an impeller outflow.

Several requirements need to be met in order to obtain good experimental data from the measurements:

- The measurement should start immediately after the cylinder rotation starts in order to capture as much images as possible before significant viscous annihilation due to the domain boundary occurs.
- The flow phenomena that are to be studied should occur prior to the induction of three-dimensional motion, i.e. $t < t_{cr}$.
- The vertical domain extent needs to be reduced to avoid the manifestation of a temporary Taylor-Couette-like instability.
- A lot of care should be taken in preparation of the particle suspension and the mixing of the suspension with the water in the measurement domain. This to eliminate particles sticking to the horizontal surfaces as much as possible.
- A laser sheet cut-off needs to be employed and optimizing the laser sheet is essential for good correlation as well as mitigating the problem of light scattering towards particles outside the laser sheet.
- The experiment preparation and execution should be very well done. This is where a large amount of skill and routine comes into play, as well as a bit of luck.

When all the above requirements are met, good measurements are likely, though not certain, to follow.

The vortical structure that has been obtained in these last measurements was extensively compared with available data. The vortex size matched that of the vortices in the numerical

simulations, as did the approximated number of vortices and the propagation speed ratio. The numerically observed regions of opposite-signed vorticity were also clearly identified at about the same position in the experiment.

Also, a comparison has been conducted with available experimental compressor stall data and the propagation speed ratio proved to be within a given interval. It is in the lower part of this interval, correctly indicating a relatively large structure. In experiments in the vaneless diffuser of a radial flow pump, the opposite signed vortex pair was also observed, as it was in the model experiments and the numerical results. Hence, even when comparing the experimental data from the model set-up with configurations that do include a through-flow, at least some of the characteristics match.

6.2 Recommendations

The current water model is an approximation of a numerical model, which is in itself an approximation of a vaneless diffuser of a centrifugal compressor. Improving the approximation would include implementing an impeller and diffuser through-flow.

Should one want to obtain more quantitative data from the experiments conducted in the water model, calibrations have to be performed for each measurement session. This would allow a more accurate determination of the relevant length and velocity scales.

Due to the early onset of notable viscous annihilation of the emerging vorticity structures and the onset of three-dimensional motion, a larger measurement domain may be desirable. One can then track the movement of the patches for a longer period of time and maybe gain more insight into the number of patches along the model's circumference. This is an interesting parameter in rotating stall and well worth studying in more detail.

Now that measurement procedure has been fully developed, one can obtain a larger measurement database by altering the set-up characteristics. A different cylinder rotational speed would be interesting to use and different configurations of the rotating body may be examined, i.e. more or less blades and maybe even different blade geometries.

Bibliography

- [Abd79] Abdelhamid, A.N., Colwill, W.H., Barrows, J.F. (1979). Experimental investigation of unsteady phenomena in vaneless radial diffusers, in *Journal of Engineering for Power*, Vol. 101, pp. 52-60.
- [Abd80] Abdelhamid, A.N. (1980). *Analysis of rotating stall in vaneless diffusers of centrifugal compressors*. ASME paper 80-GT-184.
- [Abe93] Abed, E.H., Houpt, P.K., Hosny, W.M. (1993). Bifurcation analysis of surge and rotating stall in axial flow compressors, in *Journal of Turbomachinery*, Vol. 115, pp. 817-824.
- [Are83] Aref, H. (1983). Integrable, chaotic and turbulent vortex motion in two-dimensional flows, in *Annual Review of Fluid Mechanics*, Vol. 15, pp. 345-389.
- [Ban99] Banaszuk, A., Krener, A.J. (1999). Design of controllers for MG3 compressor models with general characteristics using graph backstepping, in *Automatica*, Vol. 35(8), pp. 1343-1368.
- [Bat67] Batchelor, G.K. (1967). *An Introduction to Fluid Dynamics*. Cambridge, UK: Cambridge University Press.
- [Bel01] Belta, C., Gu, G., Sparks, A., Banda, S. (2001). Rotating stall control for axial flow compressors, in *Automatica*, Vol. 37(6), pp. 921-931.
- [Bot94] Botros, K., Henderson, J. (1994). Developments in centrifugal compressor surge control - A technology assessment, in *Journal of Turbomachinery*, Vol. 116(2), pp. 240-249.
- [Bra48] Bradshaw, G.R., Laskin, E.B. (1948). *Experimental Study of the Effect of Vaneless-Diffuser Diameter on Diffuser Performance*, National Advisory Committee for Aeronautics, technical note no. 1713. Lewis Flight Propulsion Laboratory, Cleveland, Ohio, USA.
- [Bus96] Buse, M., Jongh, F. de, Vial, F. (1996). Performance improvement of low volume flow centrifugal compressor stages, in *Proceedings of the 6th European Congress on Fluid Machinery for the Oil, Petrochemical and Related Industries*, Vol. C508/033/96. The Hague, The Netherlands, 1996.
- [Cam98] Camp, T.R., Day, I.J. (1998). A study of spike and modal stall phenomena in a low-speed axial compressor, in *Journal of Turbomachinery*, Vol. 120, pp. 393-401.
- [Che98] Chen, X., Gu, G., Martin, P., Zhou, K. (1998). Rotating stall control via bifurcation stabilization, in *Automatica*, Vol. 34(4), pp. 437-443.
- [Cho73] Chorin, A.J., Bernard, P.S. (1973). Discretization of a vortex sheet, with an example of roll-up, in *Journal of Computational Physics*, Vol. 13, pp. 423-429.
- [Chr73a] Christiansen, J.P. (1973). Numerical simulation of hydrodynamics by the method of point vortices, in *Journal of Computational Physics*, Vol. 13, pp. 363-379.

- [Chr73b] Christiansen, J.P., Zabusky, N.J. (1973). Instability coalescence and fission of finite-area vortex structures, in *Journal of Fluid Mechanics*, Vol. 61, pp. 219-243.
- [Col03] Coller, B.D. (2003). Intriguing nonlinear dynamics of a controller with a sluggish actuator, in *Automatica*, Vol. 39(12), pp. 2049-2058.
- [Cum89] Cumpsty, N.A. (1989). *Compressor Aerodynamics*. Harlow, Essex, England: Longman Scientific & Technical.
- [Cur03] Currie, I.G. (2003). *Fundamental Mechanics of Fluids*, third edition. New York, New York, USA: Marcel Dekker, Inc.
- [Day93] Day, I.J. (1993). Stall inception in axial flow compressors, in *Journal of Turbomachinery*, Vol. 115, pp. 1-9.
- [Dou98] Dou, H.-S., Mizuki, S. (1998). Analysis of the flow in vaneless diffusers with large width-to-radius ratios, in *Journal of Turbomachinery*, Vol. 120, pp. 193-201.
- [Eps89] Epstein, A., Ffowcs Williams, J., Greitzer, E. (1989). Active suppression of aerodynamic instabilities in turbomachines, in *Journal of Propulsion*, Vol. 5(2), pp. 204-211.
- [Fre98] Freeman, C., Wilson, A., Day, I., Swinbanks, M. (1998). Experiments in active control of stall on an aeroengine gas turbine, in *Journal of Turbomachinery*, Vol. 120(4), pp. 637-647.
- [Fri84] Frigne, F., van den Braembussche, R. (1984). Distinction between different types of impeller and diffuser rotating stall in a centrifugal compressor with vaneless diffuser, in *Journal of Engineering for Gas Turbines and Power*, Vol. 106, pp. 468-474.
- [Gre81] Greitzer, E.M. (1981). The stability of pumping systems - The 1980 Freeman scholar lecture, in *Journal of Fluids Engineering*, 103(2), pp. 193-242.
- [Had99] Haddad, W.M., Leonessa, A., Chellaboina, W.-S., Fausz, J.L. (1999). Nonlinear robust disturbance rejection controllers for rotating stall and surge in axial flow compressors, in *IEEE Transactions on Control Systems Technology*, Vol. 7(6), pp. 391-398.
- [Heij92] Heijst, G.J.F. van (1992). *Voortgezette Stromingsleer I (3T100)*. Eindhoven University of Technology, Eindhoven, The Netherlands, Lecture Notes.
- [Hoe83] Hoeijmakers, H.W.M., Vaatstra, W. (1983). A higher order panel method applied to vortex sheet roll-up, in *AIAA Journal*, Vol. 21(4), pp. 516-523.
- [Hu97] Hu, C. (1997) <http://www.riam.kyushu-u.ac.jp/ship/STAFF/hu/>.
- [Hun94] Hunziker, R., Gyarmathy, G. (1994). The operational stability of a centrifugal compressor and its dependence on the characteristics of the subcomponents, in *Journal of Turbomachinery*, Vol. 116, pp. 250-259.
- [Jan64] Jansen, W. (1964). Rotating stall in a radial vaneless diffuser, in *Journal of Basic Engineering*, Vol. 86(4), pp. 750-758.
- [Jef56] Jeffreys, H., Jeffreys, B.S. (1956). *Methods of Mathematical Physics*. Cambridge, UK: Cambridge University Press.
- [Jus99] Justen, F., Ziegler, K. U., Gallus, H. E. (1999). Experimental investigation of unsteady flow phenomena in a centrifugal compressor vaned diffuser of variable geometry, in *Journal of Turbomachinery*, Vol. 121, pp. 763-771.

- [Käm82] Kämmer, N., Rautenberg, M. (1982). *An Experimental Investigation of Rotating Stall in a Centrifugal Compressor*. ASME paper 82-GT-82.
- [Käm86] Kämmer, N., Rautenberg, M. (1986). A distinction between different types of stall in a centrifugal compressor stage, in *Journal of Engineering for Gas Turbines and Power*, Vol. 108, pp. 83-92.
- [Kan99] Kang, W., Gu, G., Sparks, A., Banda, S. (1999). Bifurcation test functions and surge control for axial flow compressors, in *Automatica*, Vol. 35(2), pp. 229-239.
- [Kra87] Krasny, R. (1987). Computation of vortex sheet roll-up in the Trefftz plane, in *Journal of Fluid Mechanics*, Vol. 184, pp. 123-155.
- [Krs95] Krstic, M., Protz, J. M., Paduano, J. D., Kokotovic, P. V. (1995). Backstepping designs for jet engine stall and surge control, in *Proceedings of the 34th IEEE Conference on Decision and Control*, pp. 3049-3055.
- [Kun04] Kundu, P.K., Cohen, I.M. (2004). *Fluid Mechanics*, third edition. San Diego, California, USA: Elsevier Academic press.
- [Law95] Lawless, P.B., Fleeter, S. (1995). The active control of rotating stall in a low speed centrifugal compressor, in *Proceedings of the 1995 SPIE International Symposium on Sensing, Actuation and Control*, Vol. 2494, pp. 196-206. Orlando, Florida, USA.
- [Lia96] Liaw, D.-C., Abed, E.H. (1996). Active control of compressor stall inception: a bifurcation-theoretic approach, in *Automatica*, Vol. 32(1), pp. 109-115.
- [Lig63] Lighthill, M.J. (1963). Introduction. Boundary layer theory, in *Laminar Boundary Layers*, edited by L. Rosenhead. Oxford, Great Britain: Oxford University Press.
- [Lje05a] Ljevar, S., de Lange, H.C., van Steenhoven, A.A. (2005). Rotating stall characteristics in a wide vaneless diffuser, in *Proceedings of GT2005 - ASME Turbo Expo 2005: Power for Land, Sea and Air*. Reno-Tahoe, Nevada, USA, June 2005.
- [Lje05b] Ljevar, S., de Lange, H.C., van Steenhoven, A.A. (2005). Rotating Stall in a Two-Dimensional Vaneless Diffuser Flow, in *Proceedings of the 6th European Conference on Turbomachinery*, Vol II, pp. 615-623+770. Lille, France, 2005.
- [Lje05c] Ljevar, S., de Lange, H.C., van Steenhoven, A.A. (2005). Two-dimensional rotating stall analysis in a wide vaneless diffuser, in *International Journal of Rotating Machinery*, to be published.
- [Lje06] Ljevar, S., de Lange, H.C., van Steenhoven, A.A., Dupont, P., Caignaert, G., Bois, G. (2006). Core flow instability in wide vaneless diffusers on behalf of rotating stall investigation, to be published.
- [McC90] McCaughan, F.E. (1990). Bifurcation analysis of axial flow compressor stability, in *SIAM Journal on Applied Mathematics*, Vol. 50(5), p. 1232-1253.
- [McD90] McDougall, N., Cumpsty, N., Hynes, T. (1990). Stall inception in axial compressors, in *Journal of Turbomachinery*, Vol. 112(1), pp. 116-125.
- [Meu02] Meuleman, C.H.J. (2002). *Measurement and Unsteady Flow Modelling of Centrifugal Compressor Surge*. PhD. thesis, Eindhoven University of Technology, Eindhoven, The Netherlands: University Press Facilities, ISBN 90-386-2564-2.
- [Nay02] Nayfeh, M.A., Abed, E.H. (2002). High-gain feedback control of rotating stall in axial flow compressors, in *Automatica*, Vol. 38(6), pp. 995-1001.

- [Nis82] Nisenfeld, A.E. (1982). *Centrifugal Compressors*. Research Triangle Park, North Carolina, USA: The Instrument Society of America.
- [Pam93] Pampreen, R.C. (1993). *Compressor Surge and Stall*. Norwich, Vermont, USA: Concepts ETI, Inc.
- [Pet95] Peters, M.C.A.M., Hoeijmakers, H.W.M. (1995). A vortex sheet method to unsteady flow separation from sharp edges, in *Journal of Computational Physics*, Vol. 120, pp. 88-104.
- [Pla03] Plas, G.A.J. van der, Zoetewij, M.L., Bastiaans, R.J.M., Kieft, R.M., Rindt, C.C.M. (2003). *PIV, PTV and HPV User's Guide 1.1*. Eindhoven: Eindhoven University of Technology.
- [Pre92] Press, W.H., Teukolsky, S.A., Vetterling, W.T., Flannery, B.P. (1992). *Numerical Recipes in C, the art of scientific computing*, second edition. Cambridge, United Kingdom: Cambridge University Press.
- [Rod91] Rodgers, C. (1991). Centrifugal compressor inlet guide vanes form increased surge margin, in *Journal of Turbomachinery*, Vol. 113(4), pp. 696-701.
- [Sar01] Saravanamuttoo, H.I.H., Rogers, G.F.C., Cohen, C. (2001). *Gas Turbine Theory*, fifth edition. Harlow, Essex, England: Prentice Hall.
- [Sch00] Schlichting, H. (2000). *Boundary Layer Theory*, 8th revised and enlarged edition. Berlin, Germany: Springer.
- [Sen77] Senoo, Y., Kinoshita, Y. (1977). Influence of inlet flow conditions and geometries of centrifugal vaneless diffusers of a centrifugal compressor, in *Journal of Fluids Engineering*, Vol. 99, pp. 98-103.
- [Tsu96] Tsujimoto, Y., Yoshida, Y., Mori, Y. (1996). Study of vaneless diffuser rotating stall based on two-dimensional inviscid flow analysis, in *Journal of Fluids Engineering*, Vol. 118, pp. 123-127.
- [Wan02a] Wang, Y., Murray, R.M. (2002). Bifurcation control of rotating stall with actuator magnitude and rate limits: Part I - model reduction and qualitative dynamics, in *Automatica*, Vol. 38(4), pp. 597-610.
- [Wan02b] Wang, Y., Yeung, S., Murray, R.M. (2002). Bifurcation control of rotating stall with actuator magnitude and rate limits: Part II - control synthesis and comparison with experiments, in *Automatica*, Vol 38(4), pp. 611-625.
- [Wil00] Willems, F.P.T. (2000). *Modeling and Bounded Feedback Stabilization of Centrifugal Compressor Surge*. PhD. thesis, Eindhoven University of Technology, Eindhoven, The Netherlands: University Press Facilities, ISBN 90-386-2931-1.
- [Wui02] Wuibaut, G., Bois, G., Dupont, P., Caignaert, G., Stanislas, M. (2002). PIV measurements in the impeller and the vaneless diffuser of a radial flow pump in design and off-design operating conditions, in *Journal of Fluids Engineering*, Vol. 124, pp.791-797.

Appendix A

Image Recording Equipment

A.1 The laser and its appurtenances

The laser that has been used in this project is a Spectra-Physics Quanta-Ray Class IV Nd-YAG laser. The timing of the laser pulses and the triggering of the camera was done with a four-channel digital delay/pulse generator, manufactured by Stanford Research Systems, Inc, Model DG 535. Figure A.1 contains photographs of the laser itself, its control panel, its power source and the delay generator.

The control panel allows the user to adjust the laser operation to his or her specific needs. In the measurements as they were conducted, the following settings were used. The rep button should be down, the Q-Switch and Rep rate buttons should both be on external. The switch for lamp energy should be turned from 0 to 10 slowly.

The cables on the delay generator should be connected exactly as specified below in table A.1. Another important thing to be specified on the delay generator is the times between pulses and signals. There are four times that need specifying, three of which are fixed for the specific laser. The other is dependent on the velocity scales in the visualized flow and is denoted with an asterisk in table A.1.

Table A.1: Coaxial delay generator connections.

plug	connected to	times specification
T ₀	camera trigger	-
A	input lamp trigger on power supply	$A = T + 0.000082$
B	input G-SW trigger on power supply	$B = A + 0.000174$
C	input lamp trigger delayed on power supply	$C = D - 0.000175$
D	laserhead	$D = B + 0.0008^*$

The laser beam from the laser is guided to the experimental set-up using a series of mirrors and a sheet is created using a negative lens. Figure A.2 shows a mirror and a lens as they were used during the measurements.

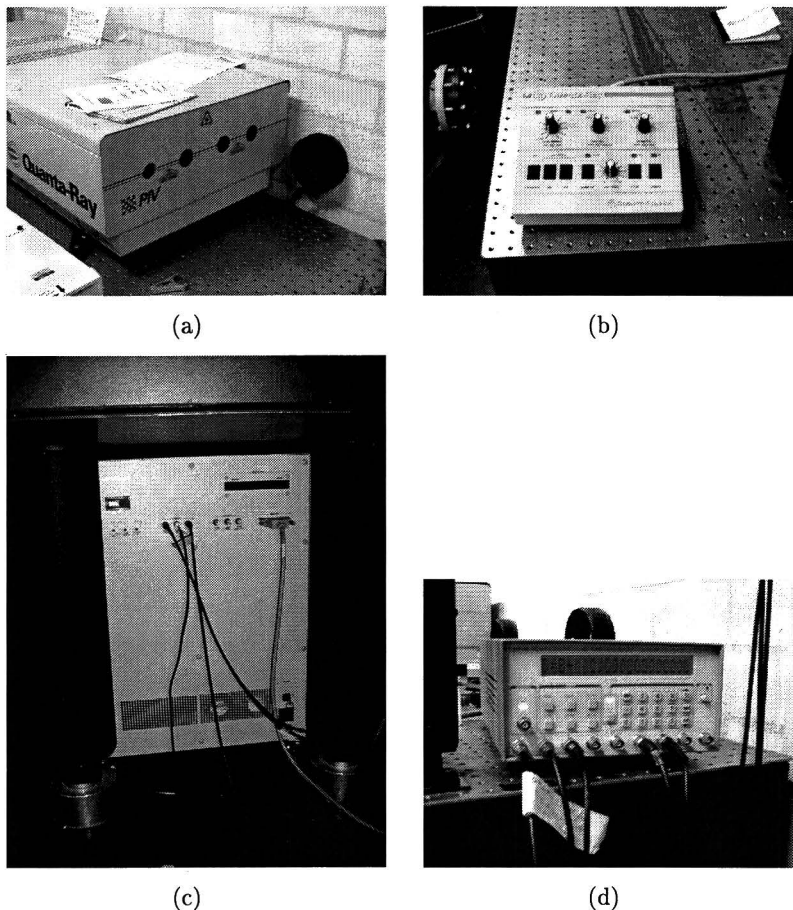


Figure A.1: The laser itself (a), its control panel (b), its power source(c) and the delay generator (d).



Figure A.2: A laser mirror (a) and the negative lens (b).

A.2 The camera and computer system

The camera used in this project is a 10 bit Kodak Megaplug Camera, Model ES1.0 and the lenses used include a Navitar TV lens 75mm F1.3, a Navitar TV lens 50mm F1.3, a Navitar CCTV lens 25mm F1.4 and a Nikon AF Nikkor 50mm 1:1.4D lens. In some measurements extension rings (1mm) or tubes (5mm) were used. The images captured by the camera are stored on a computer system. The camera is shown in figure A.3.

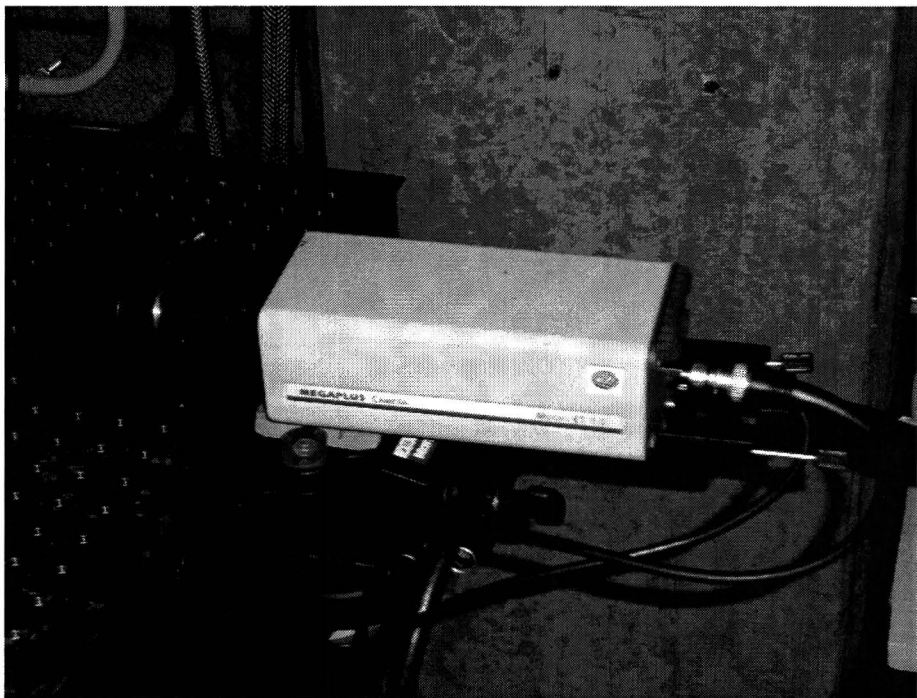


Figure A.3: The 10 bit camera.

The settings in the camera software during measurements are as follows. The camera exposure time is 31.990 ms. The mode is to be set to Trig Dbl Exp, the trigger source to TTL (External) and the trigger polarity to Positive Edge.

Appendix B

Detailed Data Conversion

As described in section 2.1.2, the data files from the experiments are first stored on one of the workstations in the laser laboratory, using a program called VideoSavant. The naming convention for these files has been consistently taken to be `ddmmyy_meas.rtd` with the first six characters obviously defining the measurement date. When more than one measurement files were stored on one day the string 'meas' was followed by a number, without any separating characters. The rest of this appendix will deal with an example: the second measurement on April 19th 2005, stored in the directory `frank` on the D-drive of the `kwek` workstation. The real time display file would then be called `190405_meas2.rtd`.

The image frames in this file are extracted and converted using a UNIX system. The simple program `do` by Gert van der Plas is used to automate batch operations. We will use an example of 501 files which we all wish to extract and convert. The extraction command is then:

```
do 0 500 1 "rtdclient ES1-10 kwek.wtb.tue.nl %d d:\\frank\\190405_meas2.rtd im190405_2_%05d.pgm".
```

The conversion command, which is used to convert the 10 bit files to 8 bit files needed for correlation in PIVview reads: `do 0 500 1 "convert -depth 8 im190405_2_%05d.pgm im190405_2_%05d.pgm"`. Note that the only difference between the 10 and the 8 bit files lies in the way the 5 digit number is preceded by either a dot or an underscore.

The 8 bit bitmap files are subsequently correlated in PIVview while using 32 by 32 pixels interrogation areas with 50% overlap. A double correlation is used, combined with a multi-grid interrogation method with an initial interrogation area of 128 by 128 pixels. Peak detection is done with a 3 point Gauss fit and the outlier detection and replacement are turned on as well. Several parameters and even options have been tuned and turned on or off to yield the best results for each measurement separately. The velocity field data is stored in files, which, in accordance with the naming convention are named `im190405_2_%05d.nc`.

With the aid of the MEXCDF toolbox in MATLAB a flexible script was programmed to enable further data editing and enable more representation options. The code is available from the author. Easily accessible text-files hold the relevant output from this step. Instantaneous, averaged and fluctuation data is stored in files named `im190405_2_%05d_inst.piv`, `im190405_2_aver.piv` and `im190405_2_%05d_fluc.piv`, respectively. All these steps are easily identified in the block diagram of section 2.1.2.

Appendix C

The point vortex analogy

C.1 Proving the analogy

When we assume a vorticity distribution $\omega(\mathbf{x})$, the corresponding velocity field is derived as follows, see *van Heijst* [Heij92]. Any velocity field can be written in terms of a sum of an irrotational field \mathbf{v}_1 and a rotational, but divergence-free field \mathbf{v}_2 . We can pour this into a mathematical formulation:

$$\mathbf{v} = \mathbf{v}_1 + \mathbf{v}_2 \quad \text{with} \quad (\text{C.1})$$

$$\nabla \times \mathbf{v}_1 = 0 \quad \text{and} \quad (\text{C.2})$$

$$\nabla \cdot \mathbf{v}_2 = 0. \quad (\text{C.3})$$

The continuity equation for incompressible flows implies:

$$\nabla \cdot \mathbf{v} = \nabla \cdot (\mathbf{v}_1 + \mathbf{v}_2) = \nabla \cdot \mathbf{v}_1 + \nabla \cdot \mathbf{v}_2 = 0, \quad (\text{C.4})$$

which, after substitution of equation C.3 yields

$$\nabla \cdot \mathbf{v}_1 = 0. \quad (\text{C.5})$$

When we now introduce the velocity potential ϕ , whose gradient equals the irrotational flow field,

$$\left. \begin{array}{l} \mathbf{v}_1 = \nabla \phi \\ \nabla \cdot \mathbf{v}_1 = 0 \end{array} \right\} \nabla \cdot \nabla \phi = 0 \rightarrow \nabla^2 \phi = 0 \quad (\text{C.6})$$

the desire arises to introduce a similar variable for the rotational field as well:

$$\left. \begin{array}{l} \mathbf{v}_2 = \nabla \times \mathbf{B} \\ \omega = \nabla \times \mathbf{v}_2 \end{array} \right\} \nabla \times \nabla \times \mathbf{B} = 0. \quad (\text{C.7})$$

Since the introduced vector potential \mathbf{B} can be chosen divergence-free, and the following vector identity holds:

$$\nabla^2 \mathbf{B} = \nabla(\nabla \cdot \mathbf{B}) - \nabla \times \nabla \times \mathbf{B}, \quad (\text{C.8})$$

the term on the right of the curly bracket in equation C.7 can be rewritten to $-\nabla^2 \mathbf{B}$ and hence, we end up with two Poisson type equations:

$$\nabla^2 \phi = 0 \quad (\text{C.9})$$

$$\nabla^2 \mathbf{B} = -\omega. \quad (\text{C.10})$$

The solution of equation C.10 is formulated by Jeffreys and Jeffreys [Jef56] as

$$\mathbf{B}(x) = \frac{1}{4\pi} \int_V \frac{\boldsymbol{\omega}'}{s} dV(\mathbf{x}'), \quad (\text{C.11})$$

with

$$\left. \begin{aligned} \boldsymbol{\omega}' &= \boldsymbol{\omega}(\mathbf{x}'), \\ \mathbf{s} &= \mathbf{x} - \mathbf{x}', \\ s &= |\mathbf{s}| = \sqrt{(x - x')^2 + (y - y')^2 + (z - z')^2}, \end{aligned} \right\}. \quad (\text{C.12})$$

The integral is taken over the entire fluid domain and the solution gives \mathbf{B} in \mathbf{x} , due to a vorticity distribution in \mathbf{x}' . Recalling $\mathbf{v}_2 = \nabla \times \mathbf{B}$ and identifying $\nabla \times \boldsymbol{\omega}' = 0$, since the curl operates on \mathbf{x} rather than \mathbf{x}' and $\nabla(\frac{1}{s}) = \frac{-\mathbf{s}}{s^3}$, Batchelor [Bat67] derives

$$\mathbf{v}_2 = -\frac{1}{4\pi} \int_V \frac{\mathbf{s} \times \boldsymbol{\omega}'}{s^3} dV(\mathbf{x}'). \quad (\text{C.13})$$

Substituting this into the equation which describes the two-component character of a velocity field yields

$$\mathbf{v}(\mathbf{x}) = \mathbf{v}_1(\mathbf{x}) - \frac{1}{4\pi} \int_V \frac{\mathbf{s} \times \boldsymbol{\omega}'}{s^3} dV(\mathbf{x}'), \quad (\text{C.14})$$

but since the irrotational flow field in a two-dimensional flow without interior boundaries is zero (streamlines do not form loops and can't end on interior surfaces), the right hand side of equation C.14 reduces back to the right hand side of equation C.13. Assigning dA to be an element of the flow field and z the perpendicular coordinate, we can rewrite this term to yield the following expression:

$$\mathbf{v}(\mathbf{x}) = -\frac{1}{4\pi} \int \int_A \frac{\mathbf{s} \times \boldsymbol{\omega}'}{s^3} dA(x', y') dz'. \quad (\text{C.15})$$

Integration with respect to z' yields the expressions

$$\left. \begin{aligned} u(x, y) &= -\frac{1}{2\pi} \int_A \frac{y-y'}{(x-x')^2 + (y-y')^2} \omega(x', y') dA(x', y') \\ v(x, y) &= +\frac{1}{2\pi} \int_A \frac{x-x'}{(x-x')^2 + (y-y')^2} \omega(x', y') dA(x', y') \end{aligned} \right\}. \quad (\text{C.16})$$

which yield the stream function

$$\psi(x, y) = -\frac{1}{4\pi} \int_A \omega(x', y') \log\{(x - x')^2 + (y - y')^2\} dA(x', y'). \quad (\text{C.17})$$

Assuming that ω decreases fast enough for larger distances from the origin, this becomes

$$\psi(x, y) = -\frac{1}{2\pi} \int_A \omega dA \quad \text{as} \quad r \equiv \sqrt{(x^2 + y^2)}, \quad (\text{C.18})$$

indicating that at some distance from the origin the velocity distribution is the same as that due to a point vortex of strength $\int \omega dA$. Hence, the validity of the point vortex analogy has been proven. Equation C.16 needs rewriting to extend its applicability to the discrete vorticity distribution present in the point vortex analogy. Point vortices induce no velocity in itself and their movement is thus the summation of contributions by other vortices or other influences. One can then write the induced velocity in summation form, as given below.

$$\frac{dx_j}{dt} = -\frac{1}{2\pi} \sum_{i=1, i \neq j}^n \gamma_i (y_j - y_i) / r_{ij}^2, \quad (\text{C.19})$$

$$\frac{dy_j}{dt} = +\frac{1}{2\pi} \sum_{i=1, i \neq j}^n \gamma_i (x_j - x_i) / r_{ij}^2 \quad \text{with} \quad (\text{C.20})$$

$$r_{ij}^2 = (x_j - x_i)^2 + (y_j - y_i)^2. \quad (\text{C.21})$$

The above has been programmed into a flexible code, which is available on request from the author. It can be used in the analysis of the motion of small vorticity patches.

C.2 Invariant quantities

Invariant quantities are quantities that are conserved and they are thus ideally suited to be used as a means to check an algorithm's validity. This section shall introduce three invariant quantities, which can be used in most point vortex systems. Exeptions to this rule are systems with the vorticity centroid at infinity. A clear example is a system of two vortices with the circulation being equal in magnitude, but opposite in sign.

Kelvin's circulation theorem states that the total circulation $\int \omega dA$ is an invariant quantity. Also, the first integral moments ($\int \omega x dA$ and $\int \omega y dA$) are invariant, which allows for the definition of the centroid of vorticity coordinates:

$$X_0 = \frac{\int \omega x dA}{\int \omega dA} \quad (\text{C.22})$$

$$Y_0 = \frac{\int \omega y dA}{\int \omega dA}. \quad (\text{C.23})$$

One can also introduce a length scale D , as a measure for the dispersion of the vorticity distribution:

$$D^2 = \frac{\int \{(x - X_0)^2 + (y - Y_0)^2\} \omega dA}{\int \omega dA}. \quad (\text{C.24})$$

The above equations, valid for vorticity patches, need rewriting, to be applicable for the discrete vorticity distribution, as it is used in the analogy. Introducing the summation form leads to the following set of equations:

$$X_0 = \frac{\sum_{i=1}^n \gamma_i x_i}{\sum_{i=1}^n \gamma_i} \quad (\text{C.25})$$

$$Y_0 = \frac{\sum_{i=1}^n \gamma_i y_i}{\sum_{i=1}^n \gamma_i} \quad (\text{C.26})$$

$$D^2 = \frac{\sum_{i=1}^n \{(x_i - X_0)^2 + (y_i - Y_0)^2\} \gamma_i}{\sum_{i=1}^n \gamma_i}. \quad (\text{C.27})$$

C.3 Runge-Kutta method

When one would incorporate equations C.25 to C.27 into a software code, one encounters a problem. This is due to the fact that in the time discretization each vortex displacement would alter the distance between the vortices, leading to a decrease in interaction and a diverging pattern. To eliminate, or at the very least mitigate this effect, Runge Kutta methods can be implemented.

The standard Euler method can be written as

$$y_{n+1} = y_n + hf'(x_n, y_n). \quad (\text{C.28})$$

This method is called unsymmetrical, since it advances solution over h but uses the derivative at the beginning of the interval. The second order Runge Kutta, or midpoint method has a scheme looking like

$$\begin{aligned} k_1 &= hf'(x_n, y_n) \\ k_2 &= hf'\left(x_{n+\frac{h}{2}}, y_{n+\frac{h}{2}}\right) \\ y_{n+1} &= y_n + k_2 \end{aligned} \quad (\text{C.29})$$

The derivative halfway through the initially computed interval (as in the Euler scheme) is now used for calculation of the actual interval. One can, for even better results repeat this process or revert to even more sophisticated methods, for which the interested reader is referred to *Press et al.* [Pre92]. In the program as it has been written, the second order Runge-Kutta and its expanded version have been used.

C.4 Two-vortex system

The stream function for a point vortex of strength γ_1 in (x_1, y_1) is given by

$$\psi = -\frac{\gamma}{2\pi} \log r, \quad \text{with} \quad (\text{C.30})$$

$$r = \sqrt{(x - x_1)^2 + (y - y_1)^2}. \quad (\text{C.31})$$

The tangential velocity component of a point vortex is derived by differentiation of the above equation, which yields

$$v_\theta = -\frac{\partial \psi}{\partial r} = \frac{\gamma_1}{2\pi r}. \quad (\text{C.32})$$

When the vortex system is expanded by placing a second vortex of strength γ_2 in (x_2, y_2) , both point vortices induce a velocity in each other and are advected with the flow, with the velocity components, expressed in the Cartesian coordinate system, being

$$\left. \begin{aligned} v_{x,1} &= -\gamma_2 \frac{y_1 - y_2}{2\pi r_{12}^2} \\ v_{y,1} &= +\gamma_2 \frac{x_1 - x_2}{2\pi r_{12}^2} \end{aligned} \right\} \quad (\text{C.33})$$

$$\left. \begin{aligned} v_{x,2} &= -\gamma_1 \frac{y_2 - y_1}{2\pi r_{12}^2} = +\gamma_1 \frac{y_1 - y_2}{2\pi r_{12}^2} \\ v_{y,2} &= +\gamma_1 \frac{x_2 - x_1}{2\pi r_{12}^2} = -\gamma_1 \frac{x_1 - x_2}{2\pi r_{12}^2} \end{aligned} \right\} \quad (\text{C.34})$$

Multiplying equations C.33 and C.34 by $2\pi\gamma_1$ and $2\pi\gamma_2$, respectively, adding the equation sets and time integration, one obtains

$$\left. \begin{aligned} \gamma_1 x_1 + \gamma_2 x_2 &= c \\ \gamma_1 y_1 + \gamma_2 y_2 &= c \end{aligned} \right\} \quad (\text{C.35})$$

in which c is a constant. Dividing equation C.35 by the combined vortex strengths yields the coordinates of the vorticity centroid, which is fixed:

$$\left. \begin{aligned} X_0 &= \frac{\gamma_1 x_1 + \gamma_2 x_2}{\gamma_1 + \gamma_2} \\ Y_0 &= \frac{\gamma_1 y_1 + \gamma_2 y_2}{\gamma_1 + \gamma_2} \end{aligned} \right\} \quad (\text{C.36})$$

By subtraction of equations C.33 and C.34, multiplication by $(x_1 - x_2)$ and $(y_1 - y_2)$, respectively and substituting $v_x = \frac{dx}{dt}$ and $v_y = \frac{dy}{dt}$, one obtains

$$\left. \begin{aligned} \frac{d}{dt}[(x_1 - x_2)^2] &= -\frac{(\gamma_1 + \gamma_2)(y_1 - y_2)(x_1 - x_2)}{2\pi r_{12}^2} \\ \frac{d}{dt}[(y_1 - y_2)^2] &= +\frac{(\gamma_1 + \gamma_2)(x_1 - x_2)(y_1 - y_2)}{2\pi r_{12}^2} \end{aligned} \right\} \quad (\text{C.37})$$

which, after addition, yields

$$\frac{d}{dt}[(x_1 - x_2)^2 + (y_1 - y_2)^2] = 0. \quad (\text{C.38})$$

Equation C.38 implies that the distance between the two point vortices is constant. Depending on the vortex strengths, the vortices have different movements. Two equally signed vortices rotate about one another. When the two vortex strengths are identical, meaning they have the same sign and the same magnitude, both vortices rotate about the vorticity centroid, see figure C.1(a). When the strengths are equally-signed but different in magnitude, the midpoint of their connection line is not fixed in space but performs a rotation about the vorticity centroid itself, see figure C.1(b). Two oppositely-signed vortices move parallel to one another, with the midpoint of their connection line rotating about the vorticity centroid, see figure C.1(c). A system of two vortices with strengths equal in magnitude, but opposite in sign has its vorticity centroid at infinity, meaning that the vortices move in a straight line, as depicted in figure C.1(d). The point vortex analogy as it was mentioned in section 2.2.1 and as it is available from the author in a MATLAB script can be used to study these described vortex motions, but can also be used to study much more complex point vortex systems.

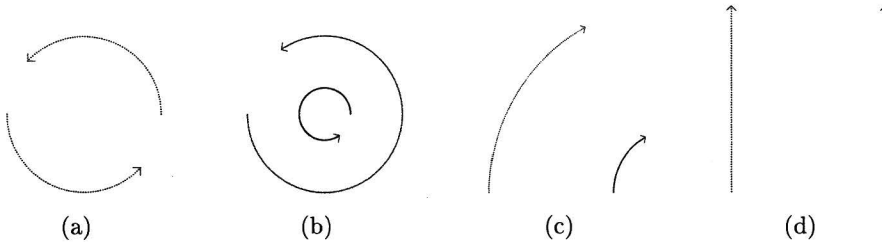


Figure C.1: Vortex paths for different systems of two point vortices.

Appendix D

Centrifugal compressor scaling

D.1 Medium scaling

Geometric compressor scaling is a well-established concept, see for example *Cumpsty et al.* [Cum89]. However, since this project deals with a water model, it is desired to gain insight in the relevant fluid scaling process as well. To do so, first some compressor aerodynamics has to be presented, since the static pressure rise needs to be maintained in the scaling effort.

Pressure rise with air as the medium

Assume air to leave the impeller tip at a speed of C , which can be resolved into a tangential component C_t and a radial component C_r . Ideally C_t equals the impeller tip speed U , see figure D.1.

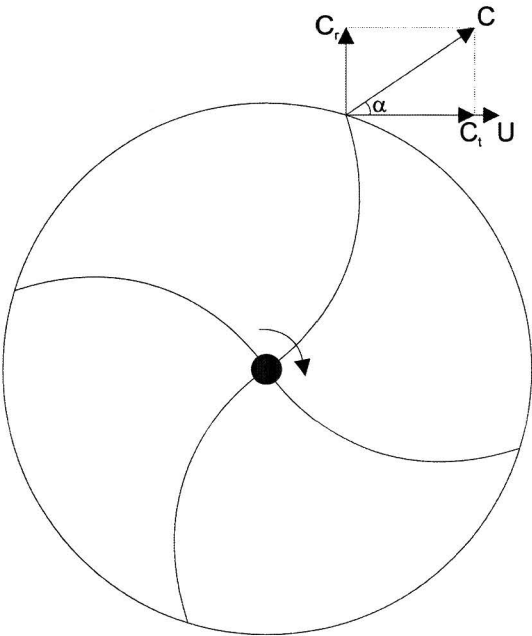


Figure D.1: Impeller and velocity components

The theoretical torque is then given by $C_t r_2$ with r_2 the impeller outlet radius. The theoretical

work done is the torque multiplied by the angular velocity. Accounting for slip, which implies that the tangential velocity never equals the impeller tip speed, leads to the introduction of a slip factor defined as

$$\sigma = \frac{C_t}{U}. \quad (\text{D.1})$$

The theoretical work done per unit mass flow is then rewritten to

$$W_{theoretical} = C_t r_2 \omega = C_t U = \sigma U^2. \quad (\text{D.2})$$

Due to, for example, frictional losses the actual work done is greater than the theoretically required work. This is taken into account by introducing a power input factor ψ :

$$W_{actual} = \psi \sigma U^2. \quad (\text{D.3})$$

Since no energy is added in a diffuser, be it vaned or vaneless, the static temperature rise across the entire compressor equals the static temperature rise across the impeller and is given by

$$T_{03} - T_{01} = \frac{\psi \sigma U^2}{c_p}. \quad (\text{D.4})$$

Herein, c_p is a range average value. The overall stagnation pressure ratio relates to the inlet temperature and the outlet temperature that would be attained in isentropic compression. The latter is not equal to T_{03} and, introducing the overall isentropic efficiency η_c , one obtains

$$\frac{p_{03}}{p_{01}} = \left(\frac{T'_{03}}{T_{01}} \right)^{\frac{\gamma}{\gamma-1}} = \left[1 + \frac{\eta_c (T_{03} - T_{01})}{T_{01}} \right]^{\frac{\gamma}{\gamma-1}} = \left[1 + \frac{\eta_c \psi \sigma U^2}{c_p T_{01}} \right]^{\frac{\gamma}{\gamma-1}}. \quad (\text{D.5})$$

Pressure rise with water as the medium

For a water model, the static pressure rise is determined using the energy equation. Here, the solution is presented, adopted from *Ljevar et al.* [Lje05c]:

$$\frac{p_{03}}{p_{01}} = 1 + \frac{\rho_w \psi \sigma U^2}{p_{01}} - \frac{\rho_w}{2p_{01}} \cdot (C_3^2 - C_1^2). \quad (\text{D.6})$$

With the indices 1,2 and 3 representing impeller inlet, impeller outlet (diffuser inlet) and diffuser outlet, respectively, the continuity equation for incompressible media can be written as

$$C_1 \cdot A_1 = C_{t,2} \cdot A_2 = C_{t,3} \cdot A_3, \quad (\text{D.7})$$

with C referring to velocities as depicted in figure D.1 and A indicating areas. Rewriting equation D.7 and assuming α to be the same for the diffuser in- and outlet, one obtains

$$C_1 = C_3 \cdot \sin \alpha \frac{A_3}{A_1} \quad (\text{D.8})$$

$$C_3 = C_2 \cdot \frac{A_2}{A_3} \quad (\text{D.9})$$

$$C_2 = \frac{C_{t,2}}{\cos \alpha} = \frac{\sigma U}{\cos \alpha} \quad (\text{D.10})$$

Combining equations D.8 to D.10, substituting the result into equation D.6 yields the pressure rise for the water model.

$$\frac{p_{03}}{p_{01}} = 1 + \frac{\rho_w \psi \sigma U^2}{p_{01}} - \frac{\rho_w \sigma^2 U^2 A_2^2 \left(1 - \sin^2 \alpha \left(\frac{A_3}{A_1}\right)^2\right)}{2 p_{01} \cos^2 \alpha A_3^2}. \quad (\text{D.11})$$

Equating the pressure rises

In this medium scaling procedure, the pressure rise across the compressor has to be constant:

$$\left(\frac{p_{03}}{p_{01}}\right)_a = \left(\frac{p_{03}}{p_{01}}\right)_w. \quad (\text{D.12})$$

Hence, one recalls equations D.5 and D.11 to derive the required impeller tip speed in the water model U_w where impeller tip speed in the air compressor is a given value U_a :

$$\left[1 + \frac{\eta_c \psi \sigma U_a^2}{c_p T_{01}}\right]^{\frac{\gamma}{\gamma-1}} = 1 + \frac{\rho_w \psi \sigma U_w^2}{p_{01}} - \frac{\rho_w \sigma^2 U_w^2 A_2^2 \left(1 - (\sin \alpha)^2 \left(\frac{A_3}{A_1}\right)^2\right)}{2 p_{01} (\cos \alpha)^2 A_3^2}. \quad (\text{D.13})$$

After some rewriting, this equation reduces to the following expression for U_w :

$$U_w = \sqrt{\frac{\left[\left(1 + \frac{\eta_c \psi \sigma U_a^2}{c_p T_{01}}\right)^{\frac{\gamma}{\gamma-1}} - 1\right] \cdot 2 p_{01}^2 (\cos \alpha)^2 A_3^2}{2 p_{01} (\cos \alpha)^2 A_3^2 \rho_w \psi \sigma - p_{01} \rho_w \sigma^2 A_2^2 \left(1 - (\sin \alpha)^2 \left(\frac{A_3}{A_1}\right)^2\right)}}. \quad (\text{D.14})$$

D.2 Geometric scaling

After reducing the energy equation for the diffuser alone and neglecting height differences, the quantity $p + \frac{1}{2} \rho C^2$ needs to be conserved:

$$p_3 - p_2 = \frac{\rho (C_2^2 - C_3^2)}{2}. \quad (\text{D.15})$$

In scaling the compressor geometry, one needs to maintain the radial pressure gradient:

$$\frac{\partial p}{\partial r} = \frac{p_3 - p_2}{r_3} = c, \quad (\text{D.16})$$

which, after substitution into equation D.15 and addition of subscripts A and B for the two geometries yields

$$\frac{C_{2,A}^2 - C_{3,A}^2}{r_{3,A}} = \frac{C_{2,B}^2 - C_{3,B}^2}{r_{3,B}}. \quad (\text{D.17})$$

Recalling equation D.9, the above is rewritten to

$$\frac{C_{2,A}^2 - C_{2,A}^2 \left(\frac{A_{2,A}}{A_{3,A}} \right)^2}{r_{3,A}} = \frac{C_{2,B}^2 - C_{2,B}^2 \left(\frac{A_{2,B}}{A_{3,B}} \right)^2}{r_{3,B}}, \quad (\text{D.18})$$

which, after identifying

$$\frac{A_2}{A_3} = \frac{2\pi r_2 B}{2\pi r_3 B} = \frac{r_2}{r_3} \quad (\text{D.19})$$

can be written as

$$\frac{C_{2,A}^2}{r_{3,A}} \left(1 - \frac{r_{2,A}^2}{r_{3,A}^2} \right) = \frac{C_{2,B}^2}{r_{3,B}} \left(1 - \frac{r_{2,B}^2}{r_{3,B}^2} \right). \quad (\text{D.20})$$

The quantity $C_{2,A}$ can be calculated by substituting equation D.14 into equation D.10, which yields an explicit relation between the water speed as it leaves the impeller $C_{2,B}$ and the diffuser outlet radius $r_{3,B}$.

This latter quantity is, due to similarity laws bound to the diffuser inlet diameter

$$\frac{r_{3,A}}{r_{2,A}} = \frac{r_{3,B}}{r_{2,B}}. \quad (\text{D.21})$$

The quantity that has been left out of discussion here, due to assumptions made prior to the start of the project, is the diffuser width B . When one would incorporate the diffuser width in the scaling effort as well, the following equation has to hold:

$$\frac{B_A}{r_{3,A}} = \frac{B_B}{r_{3,B}}. \quad (\text{D.22})$$

D.3 Dimensions of air compressor and working conditions at stall point

In this section, the geometrical of the air compressor and the operating conditions at the stall point are given in tables D.1 and D.2, respectively.

Table D.1: Air compressor dimensions.

Symbol	Description	Value	Unit
$D_{1,in}$	Inner diameter at impeller inlet	0.1450	m
$D_{1,out}$	Outer diameter at outlet	0.1592	m
$D_{2,imp}$	Diameter at impeller exit	0.2840	m
$D_{2,dif}$	Diameter at diffuser inlet	0.2900	m
D_3	Diameter at diffuser outlet	0.4410	m
B	Diffuser width	0.0036	m
A_1	Area at impeller inlet	0.00339	m ²
A_2	Area at impeller exit	0.00321	m ²
A_3	Area at diffuser exit	0.00499	m ²

Table D.2: Air compressor operating conditions at stall point.

Symbol	Description	Value	Unit
Q_V	Volume flow rate	0.0757	m ³ s ⁻¹
Q_m	Mass flow rate	1.2447	kgs ⁻¹
n	Impeller rotational speed	14716	rpm
ω	Impeller rotational speed	1541	rads ⁻¹
C	Absolute velocity at impeller outlet	198.35	ms ⁻¹
$C_{r,2}$	Radial velocity component at impeller outlet	23.57	ms ⁻¹
$C_{t,2}$	Tangential velocity component at impeller outlet	196.95	ms ⁻¹
U	Impeller tip speed	218.83	ms ⁻¹
α	Angle of absolute velocity with the tangent	6.8	°

Appendix E

Minor design issues and rejected ideas

The first realization of the experimental set-up, as it is represented in figure 3.2(a) is not the first design. An elaborate designing process preceded this design. This appendix presents some of these prior designs concepts and mentions the smaller design issues that are not elaborated on the design chapters of the report.

The first designs included a shorter cylinder and hence, a shorter experimental domain. To realize this, the domain either had to be in the bottom half of the cylindrical tank, or in the top half. A few ideas from a brain storm are presented in figure see figure E.1.

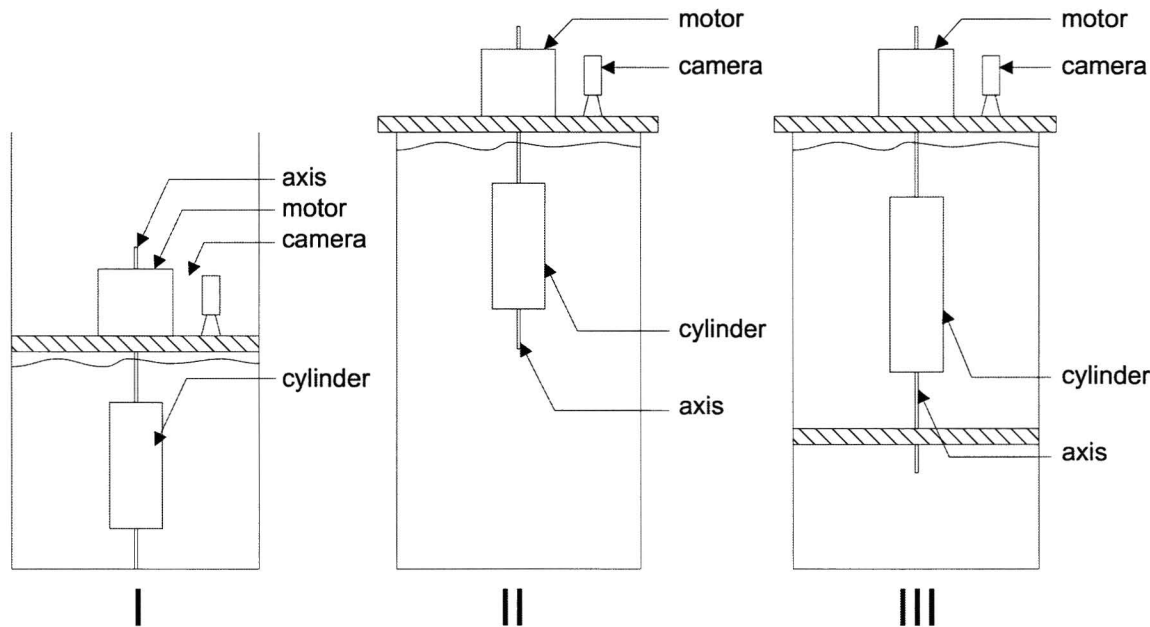


Figure E.1: Three initial brainstorm ideas on the set-up.

Option I was discarded on grounds of practical feasibility. Having the motor and the camera on a plate inside the tank would have made set-up alterations and adjustments very time-consuming. The axis and the cylinder were considered too prone to radial excitations in option II, for which reason in option III, an additional fixation arises. Extrapolating on this step-wise improving design process, the final set-up lay-out was determined as represented in

figure E.2(a).

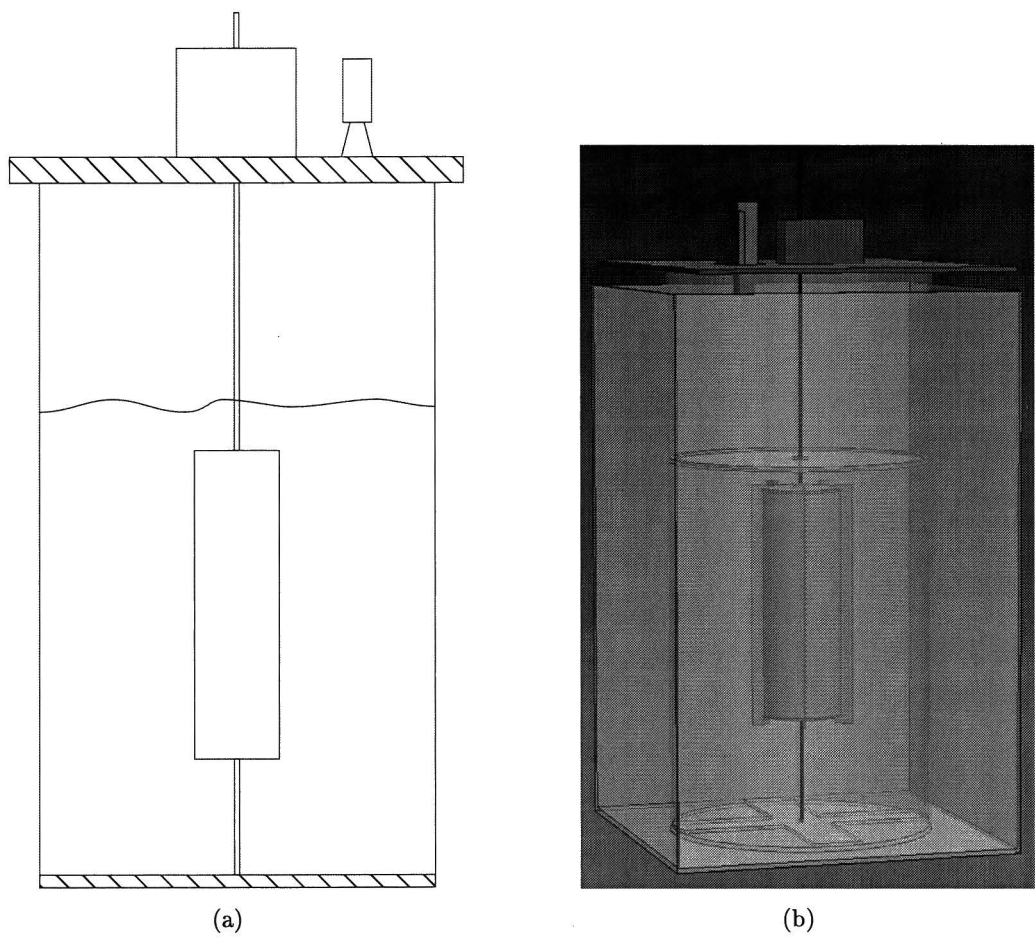


Figure E.2: Final design for first set-up realization, sketch (a) and Unigraphics image (b).

Figure E.2(b) presents a Unigraphics image of the set-up as it was designed including the blades mounted on the cylinder using the connection plates. Also, the surface plate is implemented.

Before the final connection plates had been designed, some time had been spent on devising a way to connect the rotating cylinder to the axis. A first idea was to use a threaded axis and fix it with nuts (figure E.3(a)), but the idea as implemented in the set-up was much more flexible (figure E.3(b)).

Originally, the flexibility regarding blade number and distribution was assessed by the option of having a slightly larger and changeable cylinder with blades slide over the rotating cylinder. However, the idea as put forth in the final design was much more flexible and feasible. Figure E.4 presents a schematic view of both ideas. Note that the blade thickness in figure E.4(a) is left out, for clarity reasons.

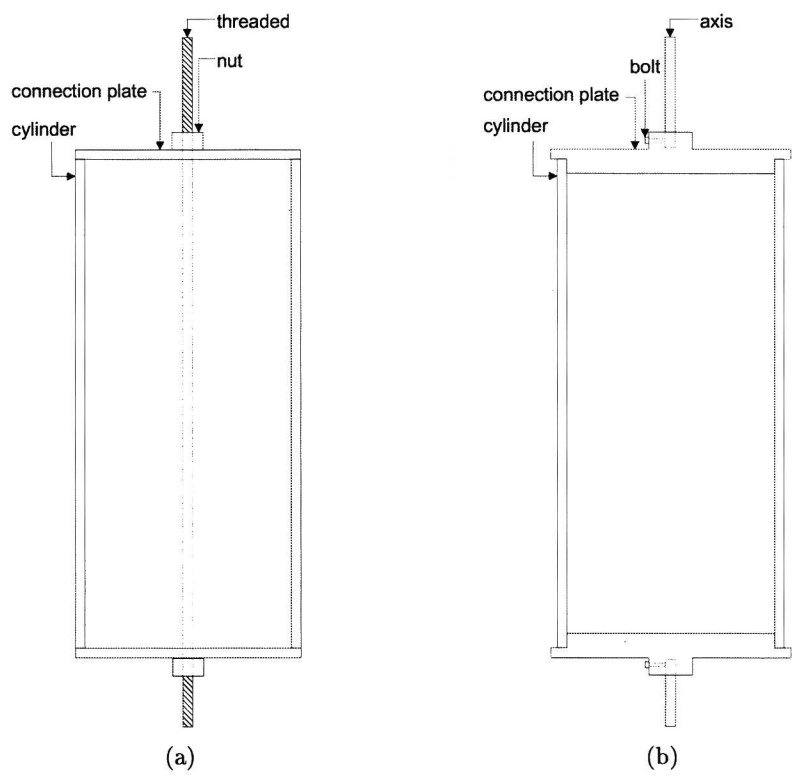


Figure E.3: Two ideas for fixing the cylinder to the axis.

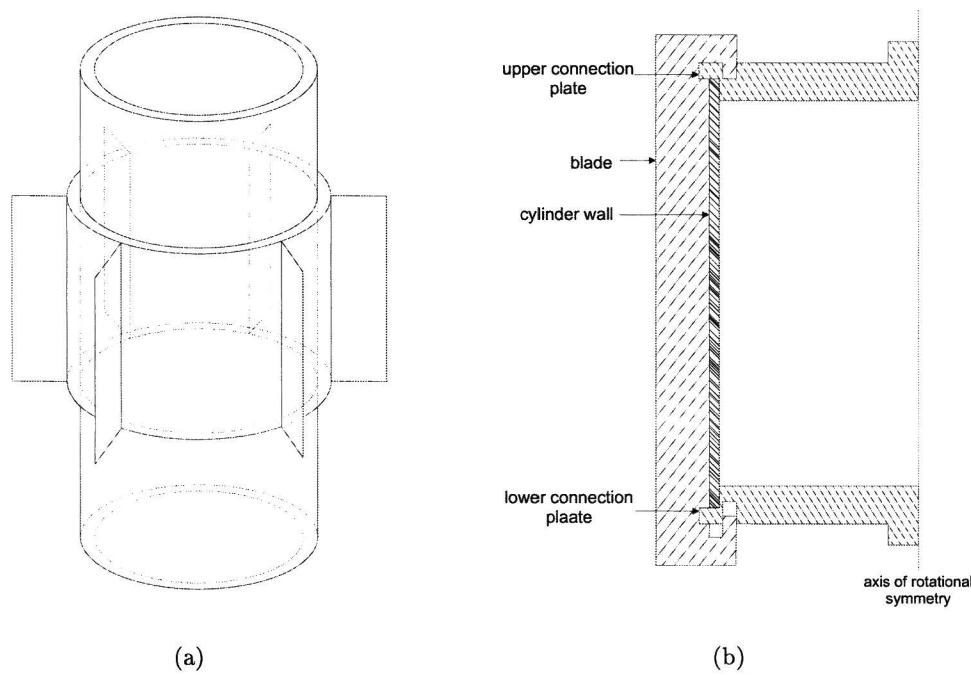


Figure E.4: Two ideas for fixing the cylinder to the axis.

Appendix F

Individual components

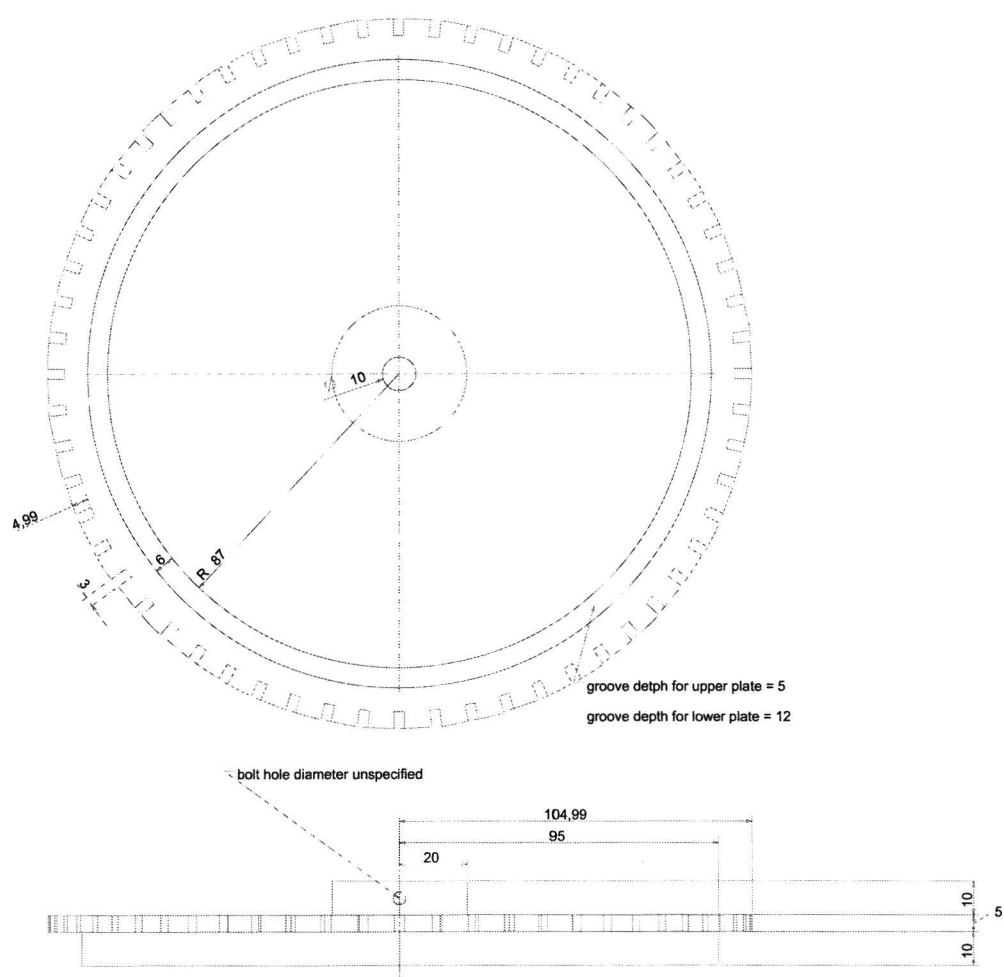


Figure F.1: The connection plates, Unigraphics drafted image.

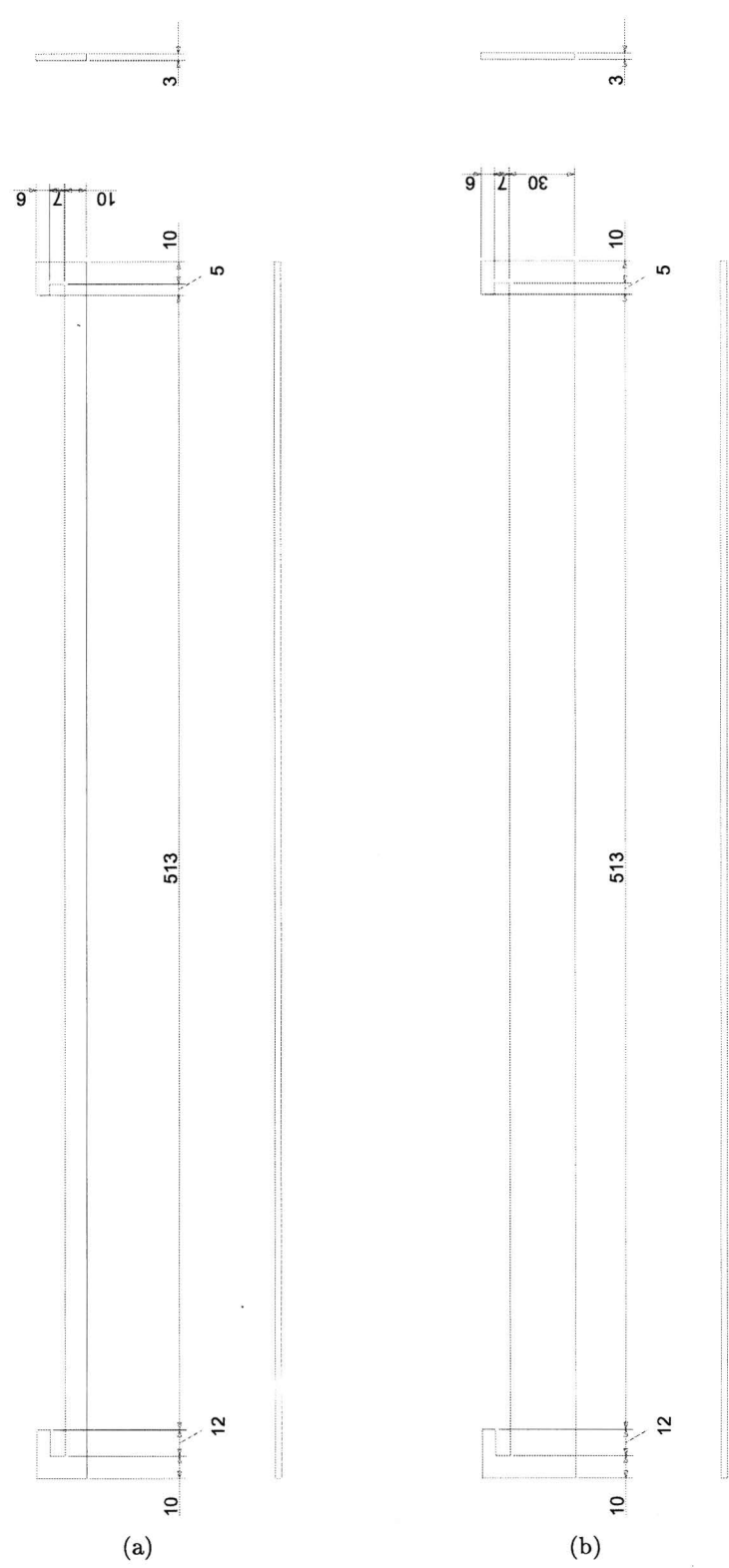


Figure F.2: The 10 mm (a) and 30 mm (b) wide blades, Unigraphics drafted image.

Appendix G

Measurement protocol

Laser alignment

- Check the level of the internal water reservoir on the back of the power supply.
- Open the tap for the cooling water and make sure there is a Nitrogen flow.
- The laser is always on, meaning that the switch on the lower right corner is always up. Turn the key clock-wise to turn the power on.
- Ensure the settings in the second column of table G.1 on the laser control panel:

Table G.1: Laser control panel settings.

parameter	alignment setting	measurement setting
Rep rate	fixed	ext
Q-Switch	long pulse	ext
Computer	up	up
Fire	up	up
Lamp on	down	down
Rep	down	down
lamp energy	0	0

- Experienced laser workers may choose to do the following steps without laser goggles, but for inexperienced people, putting on the goggles is required. Turn the laser on by pressing the **on** button on the control panel and slowly turn the lower switch of **lamp energy** to 10.
- Make sure all mirrors in a 45° orientation and start alignment by using the adjusting screws to aim the laser beam at the middle of the next mirror, but never adjust the position of the first mirror. Adjust the lens so that the beam passes through it and make sure the laser sheet is horizontal at the place you want it to be by using the vertical scalings on the side of the rectangular tank. If required, apply a sheet cut-off. Check the illumination of the image area by the laser sheets of both the correlation pulses.

Delay generator and laser settings during measurement

- Turn on the delay generator.
- Check, and if necessary adjust the settings and cables to (the asterisk denotes the parameter which needs to be adjusted according to the occurring velocities):
- Ensure the settings in the third column of table G.1 on the laser control panel.

Table G.2: Coaxial delay generator connections.

plug	connected to	times specification
T ₀	camera trigger	-
A	input lamp trigger on power supply	$A = T + 0.000082$
B	input G-SW trigger on power supply	$B = A + 0.000174$
C	input lamp trigger delayed on power supply	$C = D - 0.000175$
D	laserhead	$D = B + 0.0008^*$

Camera preparation

- Put the top plate on top of the set-up and connect the power, coaxial and computer cable to the camera. Turn on the power to the camera.
- Before having drained the tank, use the old water to focus the camera on the position of the laser sheet.
- Identify the camera and make sure the following settings are saved:

Table G.3: Laser control panel settings.

parameter	setting
exposure time	31.990 ms
mode	Trig Dbl Exp
trigger source	TTL (External)
trigger polarity	positive edge

- Create a video file in the VideoSavant software.

Set-up preparation

- Remove the top plate and drain the cylindrical tank and clean it. Clean the secondary bottom plate as well as the surface plate.
- Prepare the rotating body if you wish to adjust it.
- Prepare the particle suspension, 50 micron particles are advised for the latest measurements.
- Fill up the tank to the desired height, which you can check using a piece of temperature foil. Rotate the cylinder to remove any air bubbles under the secondary bottom plate.
- Add the particle suspension, stir it through and immediately lower the surface plate, avoiding trapping air underneath.
- Cover the set-up with the top plate again, fix the axis in the motor, connect all camera cables and connect the motor to a switchable socket.

The actual measurement and finishing up

- After ensuring sharp images, click the switch for the motor and start the image capturing process.
- Dismantle the set-up to the degree that you can remove the surface plate and dry it.
- Leave the laser on for a short while and then turn off the camera power supply, the delay generator, the laser and the water flow. Lower the Nitrogen flow.

Samenvatting

Instationaire stroming beperken het werkgebied van compressoren en voor een verhoging van het rendement dienen deze onderdrukt te worden. Voor een succesvolle toepassing van technieken om deze onderdrukking tot stand te brengen is een grondig begrip van de relevante stromingsleer nodig. Het onderzoek waarover gerapporteerd wordt in dit verslag gaat over de instabiliteit 'rotating stall' in schoeploze brede diffusors. Een van de aanpakken die wordt gevolgd is die waarin de aanname wordt gedaan dat in een brede schoeploze diffusor de wand effecten verwaarloosbaar zijn. Dit leidt tot een twee-dimensionale stroming welke onderhevig kan zijn aan instabiliteiten. In numerieke simulaties is een twee-dimensionaal roterend patroon van instabiliteitscellen verkregen, wat erg veel lijkt op rotating stall. Dit heeft geleid tot de behoefte aan experimentele verificatie.

Er diende een experimentele opstelling te worden ontworpen en gebouwd, waarin de metingen kunnen worden uitgevoerd die nodig zijn om de numerieke resultaten te staven. Een schalingsproces heeft geleid tot een water model van een compressor, waarin een roterende cylinder met schoepen erop de stroming op gang brengt.

De eerste uitvoering van de opstelling was ontworpen met het oog op een zo groot mogelijk hoogte van het domein. Dit leidde tot het optreden van een Taylor-Couette-achtige verstoring in het verticale vlak, welke niet kon worden geëlimineerd zonder een herontwerp van een deel van de opstelling. De domeinhoogte werd verkleind om de beweging in de derde dimensie te onderdrukken en een twee-dimensionaal stromingspatroon te verkrijgen.

Een uitvoerige analyse is uitgevoerd met betrekking tot deze hoogte en de beweging in de derde dimensie bleek niet geheel te elimineren. Bij hoogtes onder de 30 mm bleek het echter wel mogelijk om deze uit te stellen tot een bepaalde kritische tijd, welke toeneemt met afnemende hoogte. Nieuwe metingen in het horizontale vlak laten binnen de tijdsspanne waarin twee-dimensionale stroming verwacht wordt een groot vortcitsgebied zien, wat beweegt met een fractie van de rotatiesnelheid van de cylinder. De voortplantingssnelheid, de vortexgrootte en het geschatte aantal vortices zijn bijna exact hetzelfde als de resultaten van het numerieke model. Een duidelijk gebied met tegengestelde vortcits ontwikkelt zich in de nabijheid van de vortex in de experimentele resultaten, iets wat ook numeriek en in andere experimenten vastgesteld is.

De experimentele opstelling die nodig is voor de metingen is gerealiseerd, evenals een efficiënt protocol voor de metingen. Er zijn experimenten uitgevoerd met een enkele configuratie en de resultaten hieruit komen goed overeen met de numerieke resultaten met het oog op voortplantingssnelheid van de vortex, grootte, aantal en de aanwezigheid van tegengestelde vortcitsgebieden.

Acknowledgements

Though this report presents my graduation project, not all credit is due to me and this section is reserved to thank those involved in the project. First and foremost I would like to thank my two direct supervisors, ir. S. Ljevar and dr. ir. H.C. de Lange. Their support during the project is greatly appreciated and helped get through some tough issues. Where at the end of the project its main goal started to look unattainable, their enthusiasm might well have provided the extra incentive that made me give all I had and, at times, more. For this I can only be thankful.

I would also like to thank my graduation professor prof. dr. ir. A.A. van Steenhoven, whose ideas and suggestions during our meetings never failed to point me in the right direction and always opened up new perspectives. Some very interesting concepts were also provided by the expertise of prof. dr. ir. G.J.F. van Heijst of the Physics department, for which I am very grateful.

For helping me with the experimental set-up realization I would like to thank Geert-Jan van Hoek and Gerard van Hout, the first of whom was also very helpful in trouble-shooting the set-up in the design and realization phase. I am indebted to Milenko Jovanović and Jeroen Mans for sharing 'their' lab with me, but more importantly, their expertise regarding PIV measurements. For introducing me to that measurement technique, I wish to thank ing. G.A.J. van der Plas.

I would like to end this section by extending my gratitude towards all those involved in the Thermo Fluids Engineering division of the department of Mechanical Engineering at the Eindhoven University of Technology. In my opinion, the informal culture created by professors, research and supporting staff, secretaries and students alike, results in a very pleasant and stimulating working atmosphere.

Frank van Bortel
January 2006